UNIVERSITY OF CALIFORNIA, MERCED

Functional X-ray Imaging for Preclinical Applications

A dissertation submitted in partial satisfaction of the requirements for the degree Doctor of Philosophy

in

Bioengineering

by

Ignacio Omar Romero

Committee in charge:
Professor Wei-Chun Chin, Chair
Professor Joel Spencer
Professor Chih-Wen Ni
Professor Changqing Li

2022

The dissertation of Ignacio Omar Romero is approved, and it is acceptable in quality and form for publication on microfilm or electronically:

Professor Wei-Chun Chin, Chair

Professor Joel Spencer

Professor Chih-Wen Ni

Professor Changqing Li

University of California, Merced 2022

This dissertation is dedicated to my family, friends, and girlfriend whose unconditional support has helped me get to where I am today.

TABLE OF CONTENTS

LIST OF SYMBOLS

∇	Gradient operator
$\Phi(\mathbf{r}, p)$	Time-dependent photon density
p	Laplace transform factor
$\mu_a(\mathbf{r})$	Position dependent absorption coefficient
$\mu'_s(\mathbf{r})$	Position dependent reduced scattering coefficient
$\mathbf{r}$	Position vector
$D(\mathbf{r})$	Position dependent diffusion coefficient
c	Velocity of light in the media
$\mathbf{e}_n$	Normal vector at boundary under consideration
$\partial\Omega$	Boundary under consideration
K	Robin boundary coefficient
R_f	Internal reflection coefficient at the boundary
Ω	Domain under consideration
$S_k(\mathbf{r}, p)$	Source term representing the k^{th} X-ray beam illumination pattern
$\eta\mu_{af}(\mathbf{r})$	Light yield of optical contrast agent
$\tau(\mathbf{r})$	Lifetime of the optical contrast agent
$T_k(\mathbf{r})$	X-ray beam intensity distribution
T_0	Initial x-ray beam intensity
$\mathbf{x}_{m,1}(p)$	XLCT contrast agent concentration for a transform factor p
$\mu_x(\mathbf{r})$	X-ray attenuation coefficient at position $\mathbf{r}$
$L(\mathbf{r})$	Distance from x-ray's origin position to current position $\mathbf{r}$

$\mathbf{A}_{n_d \times I \times J,m}(p)$	XLCT System matrix for a transform factor p
$\mathbf{b}_{n_d \times I \times J,1}(p)$	Measurements from XLCT scan for a transform factor p
$\Gamma_j(s)$	Mask prior constraint vector
n_d	Number of detector nodes in finite element mesh
m	Number of XLCT/XFCT finite element nodes/image pixels
I	Number of angular projections in the XLCT scan
J	Number of linear scan steps per angular projection in XLCT scan
$\Phi_{n_d}(p)$	XLCT Sensitivity Matrix for detector node n_d
α, λ	Regularization parameter
L^q	The L^q-norm where ($q \geq 0$)
$\mu_a^{(B)}$	Background optical absorption coefficient
$\tau^{(B)}$	Background lifetime coefficient
$\mu_e(\mathbf{r})$	Linear attenuation coefficient at the X-ray excitation energy for position **r**
$\mu_f(\mathbf{r})$	Linear attenuation coefficients at the X-ray fluorescent energy for position **r**
$P_{i,m}$	XFCT Sensitivity Matrix
$F_{j,m}$	XFCT Excitation Matrix
d_n	XFCT discretization number of the detector surface
$\mathbf{A}_{n_d \times I \times J,m}$	XFCT System Matrix
$\mathbf{B}_{n_d \times I \times J,1}$	Measurements from XFCT scan
$\mathbf{X}_{m,1}$	XFCT contrast agent concentration

LIST OF FIGURES

LIST OF TABLES

ACKNOWLEDGEMENTS

I would like to thank my PhD advisor Dr. Chanqging Li for giving me the opportunity to work in the Biomedical Imaging Lab group at the University of California, Merced. His enthusiasm for the field kept me motivated despite the unusual circumstances during the pandemic. I appreciate his words of encouragement especially when I was preparing for my medical physis board certification exam and residency applications.

In addition, I would like to thank my committee members, Dr. Wei-Chun Chin, Dr. Joel Spencer, and Dr. Chih-Wen Ni who volunteered their time throughout my graduate research. I highly appreciate the great advice and suggestions during our committee meetings to become a better researcher and science communicator.

During the early years of my graduate studies, I had the pleasure of working next to Dr. Michael Lun and Dr. Yiping Guo who were senior lab members when I first joined the lab. I appreciate the welcoming support when I first started in the lab, and for providing a support system when days were rough. I was fortunate enough to witness their success and degree program completion which served as a motivator to persist. I would like to thank my current and former lab members: Dr. Michael Lun, Dr. Yiping Guo, Yile Fang, Jarrod Cortez, Yibing Zhang, Jason Ngo, Casey Hashimoto, Steven Soe, and Kurtis Brent. I hope I was of use to all of you during my time in the Biomedical Imaging Lab group.

My research has been funded by several sources. I am thankful to UC Merced for the Teaching Assistantships during my early graduate studies, and the Bioengineering Graduate Group for summer fellowship support. The Biomedical imaging lab group has received several NIH grants which helped support my work [R01 EB026646, STTR].

Next, I would like to thank my previous and current advisors. I would like to thank my undergraduate research advisor Dr. Wesley Campbell from University of California, Los Angeles (UCLA). Dr. Campbell gave me the opportunity to join my first lab group and inspired confidence to solve complex problems. This journey would not have started without him. I would like to thank my masters research advisor Dr. Usha Sinha from San Diego State University (SDSU). Dr. Sinha introduced me to the world of medical physics and helped me take the first steps as a researcher to publish my first research article. Finally, I would like to thank Dr. Richard Dunia from the Fresno Cancer Center. Dr. Dunia gave me the opportunity to get involved in my first clinical work and provided guidance during my residency applications and board exams. I hope to become a clinical physicist as knowledgeable and versatile as him.

Most importantly, I would like to thank my family. To my parents, Ignacio and Susana Romero, thank you for instilling a hard work ethic. Please know that your sacrifices do not go unnoticed although we at times don't show appreciation. I hope you know that what we strive to become is only possible because you willfully chose to provide a better life for us. Thank you to the Bamacho Bousins: Analy Romero, Mauricio Romero, Adrian Mejia, Rene Martinez, Dinora Mejia, Daniel Mejia, and Isaac Martinez for always reminding me of the importance of camaraderie and reminding me to enjoy the present instead of worrying too much about the future. I cannot think of a better group of people to share the holidays, summers, or a random weekend with. I love you all.

Finally, I would like to thank my girlfriend, Austany Macias, for being the anchor in my life. She has been with me since our subway eating and sudoku solving undergraduate years at UCLA. She has seen me grow into the person I am today. She saw good days as well as bad days, but she never missed a chance to share good food, talks, and laughs. Thank you for sticking with me throughout my career journey. I love you. I can’t wait to see where life takes us.

CURRICULUM VITAE

Education

2018-2022 *University of California, Merced*
Bioengineering, PhD Candidate
GPA: 3.89
Dissertation: "Functional X-ray Imaging for Preclinical Applications"
Advisor: Dr. Changqing Li
Contact: cli32@ucmerced.edu

2016-2018 *San Diego State University*
Medical Physics, M.S
Thesis: "Magnetization Transfer Saturation Imaging to Monitor Gender Related Differences in Leg Skeletal Muscle"
Advisor: Dr. Usha Sinha
Contact: usinha@mail.sdsu.edu

2011-2016 *University of California, Los Angeles*
Physics, B.S
Minor: Statistics

Medical Physics Certifications

April 2021 American Board of Radiology (ABR) Part 1

Publications - Peer Reviewed

1. **I.O Romero**, Y. Fang, and C. Li, "Correlation between X-ray tube current exposure time and X-ray photon number", Journal of X-ray Science and Technology (2022)

2. **I.O. Romero**, Y. Fang, M. Lun, and C. Li, "X-ray fluorescence computed tomography (XFCT) imaging with a superfine pencil beam X-ray source", Photonics (2021)

3. **I.O. Romero**, and C. Li, "A feasibility study of time of flight cone beam computed tomography imaging" Journal of X-ray Science and Technology (2021)

4. **I.O. Romero**, and C. Li, "Radiation dose estimation in pencil beam x-ray luminescence computed tomography imaging", Journal of X-ray Science and Technology (2021)

5. **I.O. Romero**, U. Sinha, "Magnetization Transfer Saturation Imaging of Human Calf Muscle: Reproducibility and Sensitivity to Regional and Sex Differences," J Magn Reson Imaging (2019), doi:10.1002/jmri.26694.

6. W. Zhang, **I.O. Romero**, and C. Li, "Time domain X-ray luminescence computed tomography: numerical simulations," Biomed. Opt. Express 10(1), 372-383 (2019), doi:10.1364/BOE.10.000372

Conference Presentations

1. **I.O Romero**, C. Li, "Functional X-ray Imaging" Presented at UC Merced Bioengineering Young Investigator Symposium (2022, May)

2. **I.O Romero**, C. Li, "Radiation dose estimation in pencil beam X-ray luminescence computed tomography imaging" Poster presented at AAPM Virtual Annual Meeting (2021, July).

3. **I.O. Romero**, Y. Fang, M. Lun, and C. Li, "X-ray fluorescence computed tomography (XFCT) imaging with a superfine pencil beam x-ray source" Presented at Northern California AAPM Chapter Young Investigator Symposium (2021, May).

4. **I.O. Romero**, Y. Fang, M. Lun, and C. Li, "Benchtop x-ray fluorescence computed tomography imaging" Presented at SPIE Medical Imaging (2021, February).

5. **I.O. Romero**, C. Li, "A feasibility study of Time of Flight Computed Tomography," Presented at Northern California AAPM Chapter Young Investigator Symposium (2020, May).

6. **I.O. Romero**, W. Zhang, C. Li, "Time domain X-ray luminescence computed tomography," Presented at 20th Annual UC Systemwide Bioengineering Symposium, University of California, Merced (2019, June).

7. J.C. White, **I.O. Romero**, and U. Sinha, "Magnetization Transfer Magnetic Resonance Imaging of Human Calf Muscle by Quantitative and Semi-Quantitative methods: Gender and Regional Differences", Poster presented at Annual CSU Biotechnology Symposium, Orange County, California (2019, January)

ABSTRACT

Functional X-ray Imaging for Preclinical Applications
Ph.D. Dissertation by **Ignacio Omar Romero**
University of California, Merced, 2022
Bioengineering
Ph.D. Advisor: **Professor Changqing Li**

In a typical X-ray imaging, an image is formed based on X-ray beam attenuation. The most common form of X-ray imaging is computed tomography (CT) which allows us to view the internal structure of tissues with fine detail. However, CT imaging provides little information about the functional capabilities of the tissues. In this dissertation, functional X-ray imaging modalities including time domain X-ray luminescence computed tomography (XLCT) and X-ray fluorescence computed tomography (XFCT) are explored for preclinical applications. The dose concerns related with these two imaging modalities are also investigated.

Optical contrast agents may be injected into the subject to give more information of the tissue function for a more accurate diagnosis. These contrast agents can release optical photons when excited with X-rays while in proximity to chemical concentrations of interest in tissues. Cancerous tumors exhibit an acidic environment and are highly vascularized which increase oxygenation levels. Optical contrast agents can be made sensitive to the cancer pH change or oxygen levels and release light when excited by X-rays. This form of X-ray imaging is XLCT imaging. Usually, researchers tend to use the optical light intensity (light yield) from the contrast agent to create the image. However, the time information of the optical photon intensity (lifetime) is useful since the time measurements can detect microenvironmental changes that are unobservable by light yield measurements. The feasibility of using the lifetime of the contrast agent instead of the light yield to create the image was numerically explored. The findings of this work reported that the lifetime images were more accurate than light yield images. The lifetime images were also found to be independent of some typical imaging acquisition parameters.

The use of X-rays to excite contrast agents that release secondary X-rays which are specific to the contrast agent material composition was also studied. This form of X-ray imaging is XFCT imaging. Chemotherapeutic drugs can be monitored in the body using this type of imaging without additional contrast agents being injected into the subject. By using a fine X-ray pencil beam and a ring detector, contrast agents embedded in an object were resolved with high contrast and submillimeter resolution with fewer imaging acquisitions.

CT imaging traditionally uses cone or fan X-ray beam geometries to reduce the radiation dose and imaging time while providing quality images. The radiation safety concerns of using a fine X-ray pencil beam imaging for high resolution imaging was investigated. Typically, the radiation dose of pencil beam X-ray imaging is difficult to measure due to instrumentation limitations. Therefore, it is best to calculate the dose with Monte Carlo methods. X-ray imaging like XLCT benefit most from high resolution

imaging to resolve sub millimeter targets in tissues. Results shows that if bright X-ray sources are used for the imaging scan, the radiation safety concerns with X-ray pencil beam imaging can be reduced and investigated further.

The image quality of X-ray imaging relies heavily on the X-ray output number which is dependent on the X-ray tube current and the exposure time. A limiting factor of good image quality is the radiation dose that will be delivered to the imaging object. Conventional methods to estimate the dose are limited and/or standardized to a specific imaging object size and imaging protocol. To accurately estimate the dose in any imaging protocol, it is better to simulate the X-ray imaging with a Monte Carlo platform. Among Monte Carlo platforms, GATE (Geant4 Application for Tomographic Emission) has gained traction in medical imaging applications. So far, there is no good way to setup the photon number for a desired X-ray tube current in GATE. The findings of this work provide an approach to correlate the X-ray tube current exposure time (mAs) to the X-ray photon number in the GATE simulation of the X-ray tube. The work provides a method to accurately estimate the dose in an imaging protocol.

The work presented in this dissertation is meant to showcase the feasibility of novel imaging techniques to promote advancements in functional X-ray imaging.

CHAPTER 1

INTRODUCTION TO BIOMEDICAL IMAGING, X-RAY LUMINESCENCE COMPUTED TOMOGRAPHY, AND X-RAY FLUORESCENCE COMPUTED TOMOGRAPHY

1.1 Introduction

X-ray imaging has remained as the workhorse for medical imaging since its discovery in 1895 by German physicist Wilhelm Roentgen [1]. X-ray imaging provides high spatial resolution medical images with fast acquisition speeds. However, X-ray imaging alone cannot provide physiological information of biological tissues. Medical imaging soon expanded to other modalities due to innovations in medical instrumentation and imaging techniques. In this chapter, several popular biomedical imaging modalities will be discussed. The following sections provide introductions and reviews of prominent functional X-ray imaging techniques: X-ray luminescence computed tomography (XLCT) and X-ray Fluorescence computed tomography (XLCT).

1.2 Review of Biomedical Imaging Modalities

In this section, several popular biomedical imaging modalities will be reviewed. The discovery and applications of X-ray imaging will first be discussed. Then nuclear medicine imaging modalities will be reviewed, followed by magnetic resonance imaging (MRI). Next optical imaging methods will be reviewed. Finally, the section will conclude with a discussion of hybrid imaging modalities.

With the discovery of X-rays, X-ray imaging was quickly implemented in clinics and hospitals. Projection radiography was first implemented in which a single exposure generates a 2D image of the internal anatomy of the imaging object. Upon emission from the X-ray tube, the X-rays must first pass through the imaging object. Some of the X-rays are lost or attenuated due to absorption or scattering effects from the different densities in the object. The remaining X-rays that pass unattenuated reach the detector forming a projection. Typically, the image is reconstructed using a filtered back projection method or iterative algorithm [2]. Currently, the most popular form of X-ray imaging is computed tomography (CT) which was developed in 1971 by Sir Godfrey N. Hounsfield and Dr. Allan M. Cormack [3]. In CT imaging, the imaging object is exposed at multiple projection angles creating an axial image with high imaging depth and spatial resolution. Multiple axial slices (images) can be stacked to form a 3D anatomical image. However, since CT

image contrast is based on attenuation, CT imaging suffers from poor sensitivity between different soft tissues and therefore cannot provide molecular (functional) imaging.

Nuclear medicine imaging like positron emission tomography (PET) and single photon emission computed tomography (SPECT) scans use radiotracers which are injected into the subject to provide tissue function information which is used to diagnose malignancies [4]. A wide variety of radiotracers are available to map molecular processes. A popular radiotracer for PET imaging is fluorodeoxyglucose 18 (FDG-18) which maps the metabolization of glucose in the object. The radiotracer undergoes positron decay where a proton from the radiotracer nucleus is converted into a neutron and a positron is ejected. Shortly after, the positron becomes annihilated by a nearby electron generating two opposing 511 keV X-rays. The transmitted pairs are detected coincidentally to map the radiotracer distribution in the object. SPECT imaging readily uses Technetium 99m for perfusion imaging studies. Tech99m is a metastable radiotracer which undergoes gamma decay in which the radiotracer ejects a gamma photon from its atomic nucleus. The transmitted gamma rays from the object are collected by the pinhole detector to map the distribution of Tech99m. The images from PET and SPECT can be reconstructed using the filtered back projection algorithm or statistical reconstruction methods [5]. PET and SPECT modalities have high sensitivity and high imaging depth which make them great molecular imaging tools. However, the best spatial resolution for PET imaging is about 0.7 mm, which is close to its intrinsic physical limits [6]. Compared to PET, SPECT imaging sensitivity and resolution is degraded due to the detector pinholes [7].

MRI uses static magnetic fields, radiofrequency (RF) pulses, and magnetic field gradients to produce high quality images that enable soft-tissues delineation by mapping proton densities [8]. A strong magnetic field polarizes the protons in the imaging object. The RF pulses excite the protons, inducing an MR signal in the receiving coils. The MR signal is localized in k-space by superimposing gradient fields. A common method of reconstructing the image is by applying the inverse Fourier transform on the k-space raw data. MRI has greater image contrast than CT and has a spatial resolution less than 1 mm [9]. However, MRI suffers from negative contrast that limits its sensitivity. In addition, the MRI scanners are costly.

Optical imaging methods are important and popular approaches for studying cellular level activities with high measurement sensitivity and high spatial resolution at shallow depths. Fluorescence imaging and bioluminescence imaging are major preclinical molecular imaging modalities [10, 11]. They are employed in most research and preclinical centers due to their unique features such as mature technology, low cost, non-ionizing radiation, and high sensitivity. Optical photons in the near-infrared region are optimal for deep tissue imaging which can image targets as deep as 10 cm [12]. Current optical methods like two photon microscopy are able to resolve probes with 0.64 μm lateral resolution [13]. However, the spatial resolution of most optical imaging methods is larger than 1 mm for targets deeper than 2 mm due to strong optical scattering in tissues and its quantification is deteriorated by the uncertainty of tissue optical properties [14]. Efforts have been made to improve its spatial resolution and quantification from both experimental system and reconstruction algorithm aspects [15, 16].

Hybrid imaging modalities have risen to circumvent the obstacles of the individual imaging modality. A molecular imaging modality which provides high sensitivity but suffers from poor spatial resolution is integrated with an anatomical imaging modality which provides high spatial resolution, but poor image contrast. Popular examples of hybrid imaging modalities are PET/CT, SPECT/CT, and PET-MRI [6, 17, 18]. Other prominent hybrid imaging modalities are X-ray luminescence computed tomography (XLCT) imaging and X-ray fluorescence computed tomography (XFCT) which will be described in the following section.

1.3 Review of X-ray Luminescence Computed Tomography (XLCT)

In this section, the first hybrid functional X-ray imaging modality will be introduced and reviewed. To begin, the X-ray luminescence process is reviewed. Next, the application for this process will be discussed: X-ray luminescence computed tomography (XLCT).

1.3.1 The X-ray Luminescence process

X-ray luminescence (XL) is a scintillation process in which the emission of optical photons is stimulated by the absorption of an X-ray photon. Scintillator materials consist of high Z nanoparticles with phosphor groups that enable the emission of optical photons [19]. In scintillating material, the X-rays from an excitation X-ray beam deposit their energy and ionize the atoms in the material releasing electrons with high kinetic energy. The high energy electrons ionize other atoms in the material resulting in a cascade of lower energy electrons. The lower energy electrons move to luminescent centers in the scintillating material which leads to transient electronic excitations. Upon electronic relaxation, optical photons are emitted. In non-scintillating materials the lower energy electrons release energy in the form of heat instead of migrating to luminescent centers. The XL process is a sensitive technique because thousands of optical photons are emitted per absorbed X-ray [20]. The XL process is the basic principle for radiation detectors which use scintillating material to detect ionizing radiation.

1.3.2 X-ray Luminescence Computed Tomography

XL imaging was first demonstrated as a 2D chemical imaging modality by Chen et al in which lanthanide doped phosphor concentrations in thin pork tissues were imaged [21, 22]. XLCT imaging combined the principles of XL and tomographic imaging to enable the reconstruction of 3D distributions of the luminescent phosphors in a biological medium. XLCT imaging is a hybrid imaging modality that combines the high contrast of optical imaging and high image spatial resolution of CT imaging. The principle of XLCT imaging is shown in Figure 1. For every rotational position, the imaging object is scanned sequentially with a collimated X-ray beam. This imaging protocol is like the ‘scan and shoot’ method from the first-generation CT imaging. Upon X-ray excitation, the luminescent contrast agents in the imaging object emit optical photons. Sensitive detectors like an electron multiplying charge coupled device (EMCCD) or photomultiplier tube

(PMT) are used to measure the optical photon signal from the object surface. Simultaneously, a CT image can be acquired with an X-ray detector to provide an anatomical reference image. Unlike optical imaging, XLCT uses X-rays to excite the luminescent targets. Therefore, major limitations imposed by optical imaging are surpassed by the X-ray excitation beam. X-rays can excite contrast agents in much thicker samples than optical beams and do not scatter easily like optical photons. Therefore, the location of the optical emissions in XLCT imaging is known to be along the X-ray beam line which provides spatial information to overcome the strong optical scattering limitations in deep tissues [23]. Image resolution in XLCT imaging is mainly limited by the X-ray beam collimation [24].

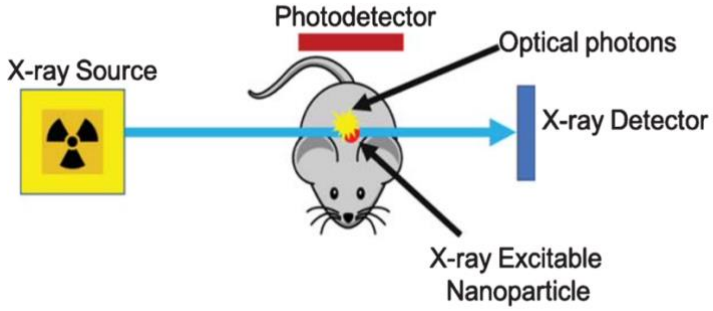

Figure 1.1: Schematic of the X-ray luminescence computed tomography (XLCT) imaging principle.

The feasibility of XLCT imaging was first demonstrated by Pratx et al in 2010 by using a selective excitation-based (pencil beam) imaging approach to scan a 4.5 cm diameter cylindrical phantom composed of tissue equivalent material embedded with nanophosphor targets. Sub-picomolar sensitivity was achieved with 1 cGy of radiation dose and with a spatial resolution of 1 mm [20, 25]. To experimentally prove the feasibility of pencil beam XLCT imaging, an XLCT prototype was built to image various phantoms with different nanophosphor target concentrations. However, the X-ray scatter in tissue was significant enough to excite nanophosphors outside the beam volume which increases noise and limited the sensitivity of the experimental study [20]. Cong et al explored the feasibility of a scatter-estimating forward model in which they were able to improve the image quality when considering the X-ray scattering effects in the reconstruction algorithm [26]. In the same study, Cong et al also simulated multiplexing to image multiple luminescent contrast agents simultaneously. Carpenter et al demonstrated in vivo multiplex XLCT imaging on a mouse with nanoparticles doped with different lanthanides [27]. To reduce the scan time of pencil beam imaging protocols, Li et al proposed a limited angle tomographic approach to show that two orthogonal projections were sufficient to reconstruct the phosphor contrast agents in the imaging object [28].

The pencil beam based XLCT imaging can obtain high spatial resolution images but has the disadvantages of a long scan time due to the subsequent line excitation imaging protocol. Other imaging geometries have been explored to overcome the long scan times of the pencil beam imaging approach like the cone beam and fan beam imaging geometries.

Chen et al proposed the cone X-ray beam XLCT imaging in which the entire imaging object is irradiated thus significantly reducing the scan time [29]. The reduced scan time comes at the cost of degraded image resolution for deep targets since the structural guidance in the image reconstruction from selective excitation is lost. Efforts have been made to improve the image spatial resolution by exploring methods that mitigate the ill-posedness of the XLCT imaging reconstruction with cone beam XLCT imaging. Zheng et al proposed a Gaussian Markov field model with a Bayesian method approach and showed improved results in image quality compared to conventional methods [30]. Liu et al proposed a compressed sensing method which showed a target location error of 1.5 mm with single-view data from an in-vivo mouse imaging study [31]. Tzoumas et al applied a coded aperture compressed sensing method and reported better spatial resolution than the conventional cone beam methods with Tikhonov regularization [32]. Liu et al used a wavelet-based single view approach to accelerate the image reconstruction and reported a target location error of 0.8 mm [33].

The feasibility of fan beam based XLCT imaging was first proposed by Cong et al. This study reported a faster acquisition compared to pencil beam due to the irradiation of a plane instead of a line and showed an improvement in spatial resolution compared to cone beam XLCT imaging [34]. Chen et al experimentally demonstrated the fan beam XLCT imaging and proposed a reconstruction algorithm that included the fan X-ray beam distribution model and adaptive split Bregman method [35]. The results showed a target location error less than 1.1 mm. Quigley et al proposed a slit collimator to scan a plane of an optical gel phantom with two targets separated 1 cm from each other and were able to resolve the targets at a depth of 1.75 cm [36].

1.4 Review of X-ray Fluorescence Computed Tomography

In this section, the second hybrid functional X-ray imaging modality will be introduced and reviewed. To begin, the X-ray fluorescence process is reviewed. Next, the application for this process will be discussed: X-ray fluorescence computed tomography (XFCT).

1.4.1 The X-ray Fluorescence process

X-ray fluorescence (XF) is described by the photoelectric effect in which an inner shell electron in the K or L shells of a high Z material is ejected due to the absorption of an X-ray photon. An outer shell electron falls to fill the vacancy left by the ejected inner shell electron. The difference in energy states between the outer shell and inner shell is emitted as a characteristic (fluorescent) X-ray which has discrete energies. The discrete energies of the characteristic X-rays are intrinsic to each element, and their energies are always lower than the energy of the incident X-ray beam which induced the fluorescent event. The XF process has been extensively used to characterize a material's elemental composition by using energy dispersive detectors. The intensity of the fluorescent X-rays is greatest when the energy of the excitation beam is just above the L-edge or K-edge of the target element. The L-edge and K-edge are discrete energy levels where X-ray absorption is increased immediately. Generally, the X-ray absorption for any material decreases with increasing

X-ray energy. Fluorescent energies resulting from absorption of X-rays above the L-edge are lower than the fluorescent energies from X-ray absorption above the K-edge. However, the intensity of the L shell X-rays is greater than the intensity of the K-shell X-rays since the L-edge absorption has a greater cross section than K-edge absorption. Compared to the XL process, the XF process is less sensitive since only one fluorescent X-ray is emitted per absorbed X-ray.

1.4.2 X-ray Fluorescence Computed Tomography

XF imaging has been exploited to nondestructively identify the chemical species in a sample. XFCT imaging combined the principles of XF and tomography imaging to enable the reconstruction of the 3D elemental distribution within the imaging object. XFCT imaging is a hybrid imaging modality that combines the high spatial resolution of CT imaging and the material analysis of X-ray fluorescence imaging. The principle of XFCT imaging is shown in Figure 2. A pencil beam imaging protocol is employed like in pencil beam XLCT imaging. For every rotational position, the imaging object is scanned sequentially with a collimated X-ray beam. An energy resolving detector is used to measure the fluorescent X-rays. An anatomical reference image can be simultaneously acquired using an X-ray detector.

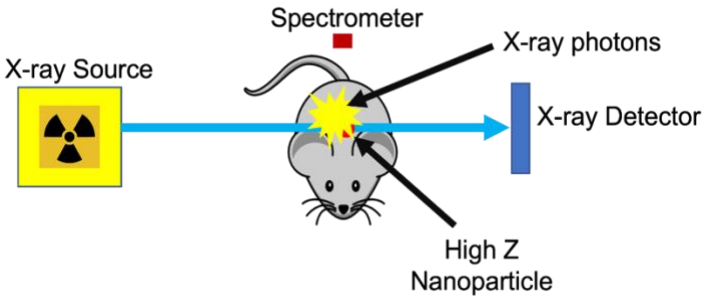

Figure 1.2: Schematic of the X-ray fluorescence computed tomography (XFCT) imaging principle.

XFCT imaging was first shown in 1987 by Boisseau et al with synchrotron X-ray sources at Brookhaven National Laboratories and were able to image trace elements of titanium and iron in glass fibers and a bee with micrometer spatial resolutions [37]. Takeda et al demonstrated in vivo and ex vivo XFCT imaging to image the distribution of an iodine contrast agent in the brains of mice [38]. Synchrotron sources have the advantage of providing bright monochromatic X-ray energies suitable to tune just above the K-edge or L-edge absorption energies of the target element. However, synchrotron X-ray source facilities are high cost and not readily accessible.

Benchtop XFCT imaging using conventional laboratory X-ray sources was first shown in 2010 by Cheong et al in which they imaged a 5 cm diameter cylindrical object with gold (Au) nanoparticles (NPs) targets using a pencil beam imaging approach with a collimator. This was the first study to implement K-edge XFCT imaging and successfully reconstructed the AuNPs distribution at relatively low concentrations (10 mg/ml) with a

polychromatic X-ray source and a single detector [39]. In 2012, Bazalova et al used numerical simulations to compare conventional CT, K-edge CT, and XFCT and reached a greater sensitivity with XFCT at the same dose [40]. In 2013, Kuang et al demonstrated multiplex XFCT imaging of Au, Gadolinium (Gd), and Barium (Ba) targets in a 3.5 cm diameter water phantom using a 5 mm pencil beam X-rays source [41].

Like pencil beam XLCT imaging, pencil beam XFCT imaging has the advantages of providing the highest spatial resolution and greatest sensitivity, but the long scan time poses a challenge. Experimental cone beam XFCT imaging was shown by Jones et al in which a 5 cm diameter phantom with 5-10 mm diameter AuNPs targets were imaged with a pinhole collimator to remove Compton scatter and improve resolution [42]. However, the resolution is limited by the size of the pinhole. Fu et al experimentally demonstrated selective-plane (fan beam) XFCT imaging using a collimator slit and position sensitive detector to image trace metals in biological samples with a synchrotron source [43]. However, the authors note that long scan times would still be required when imaging with a polychromatic source. In both geometries the potential decrease in scan times comes at the expense of sensitivity.

Despite the dose and acquisition speed advantages of the fan beam and cone beam scanning geometries, the pencil beam scanning approach results in the best spatial resolution to resolve superfine targets and sensitivity to detect smaller probe concentrations. The X-ray pencil beam size and location can be used as structural guidance in the forward model to provide high spatial resolution. The pencil beam imaging protocol will be focused on in this dissertation work.

To overcome the limitations with sensitivity in XFCT imaging, benchtop XFCT systems have adopted X-ray sources which have greater X-ray intensity and a narrower energy spectrum. The popular use of narrow collimators to shape the beam is inefficient since most of the X-rays are blocked. Hertz et al experimentally demonstrated the use of a liquid anode X-ray source which allows for greater anode heat limits to greater brightness [44]. In this work, 100-um resolution was achieved with mouse-sized imaging objects with reasonable dose and imaging time. Other approaches have employed the use of internally reflective lens to focus the X-ray beam [45-47]. However, internally reflecting capillaries only work for X-ray energies below 30 keV. X-ray sources arising from inverse Compton scattering sources and free electron lasers processes are expected to produce synchrotron radiation with much smaller facilities in the future [48, 49].

Another factor affecting sensitivity in benchtop XFCT imaging is Compton scatter. The X-rays from the incident beam can scatter from anywhere within the imaging object and reach the detector which can interfere with the fluorescent signals. The imaging system design can be optimized to reduce Compton scatter. In 2014, Ahmad et al showed through simulation that positioning detectors in a back-scatter configuration greatly increased the sensitivity to 10 ug/ml with 2 mGy of dose using monochromatic sources, however, similar improvements were seen with conventional X-ray sources [50]. To further minimize the effects of scatter, a background signal can be acquired without the contrast agent to provide an estimate of the scatter at the cost of additional radiation dose [50]. Other approaches have used interpolation techniques to remove the scatter contribution from the fluorescent signal [41].

In theory, XFCT imaging with K-shell fluorescence energies may be applicable for whole-body imaging due to its greater penetrability compared to L-shell emission energies. However, the cross section of the L-edge is greater than K-edge and the sensitivity of XFCT imaging can be improved by a factor of 7 [51]. Manohar et al demonstrated L-shell XFCT imaging and achieved a sensitivity of 20 ug/ml for AuNPs using a single detector and a collimated pencil beam X-ray source [52]. In 2019, Vernekohl et al demonstrated the use of a polycapillary X-ray optic lens to provide a high fluence rate for L-shell XFCT imaging and reduced the imaging time from 17 hrs to 1 hr [53]. For mouse size objects, a concentration of 300 ug/ml for AuNPs was imaged in 66 min. XFCT imaging in the L-shell fluorescence energies is restricted to preclinical applications and organ specific imaging since the lower X-ray energies are readily attenuated by biological tissues [54]. However, the L-shell energies can be stimulated with lower energy X-ray beams which are more accessible for laboratory use.

1.5 X-ray Excitable Contrast Agents

Only exogenous agents are available for XLCT imaging. Rare-earth nanoprobes have been extensively studied as XLCT contrast agents [55]. The nanoprobes consist of lanthanide doped material surrounded by a non-doped shell. Gadolinium oxysulfide (GOS) doped with either Eu or Tb is often used in X-ray detectors due to its high cross-section for diagnostic energy X-rays and high light yield [56]. Nanoscale X-ray excitable particles like GOS:Eu^{3+}, $NaGdF_4$:Eu, and other lanthanide-doped compounds have been successfully synthesized [57-61]. The lanthanide cation in these compounds allow the nanoparticles to emit light at wavelengths around 710 nm [61]; these wavelengths provide optimal tissue penetration for in vivo applications. The nanoparticle can be coated with a plasmonic gold shell to increase its biocompatibility [62, 63]. Karanthanasis et al and Hainfeld et al among others have reported various synthesized emission efficient Eu^{3+} doped X-ray excitable nanophosphors [62, 64].

Different classes of contrast agents exist for XFCT imaging: exogeneous agents, metal-based therapeutic agents, and endogenous contrast agents. Exogenous contrast agents can be created by adding a high Z nanoparticle to the molecular target without hindering the affinity of the target to its biological processes [54]. Metal-based therapeutic agents as an XFCT imaging contrast agents allow for the visualization of the distribution of therapeutic drugs in tissues which can give insight in the metabolism and therapy response of the drug in malignant tissues [65, 66]. The perturbation of concentrations of trace elements (endogenous contrast agents) in biological environments have been observed to be linked to diseases. However, this sensitivity has only been achieved with synchrotron radiation. In breast cancer, greater concentrations of copper (Cu) were observed in malignant tissue compared to healthy breast tissues by Gerati et al using synchrotron XRF [67]. In prostate cancer, lower level of zinc (Zn) was found compared to healthy prostate tissues by Costello et al [68]. In this dissertation, exogenous contrast agents for XFCT imaging will be focused on since the excitation energies can be much lower compared to other contrast agents for XFCT imaging.

High Z nanoparticles like Molybdenum (Mo) and Gold (Au) nanoparticles (NPs) have attracted significant attention in XFCT imaging. The K-shell and L-shell emission energies of these NPs have greater penetrability which enables deeper functional tissue imaging compared to scintillation nanoprobe optical emissions. The K-shell characteristic energy peaks for Mo are 17.48 keV and 19.61 keV. The L-shell characteristic energy peaks for Au are 9.71 keV and 11.44 keV. The energy range of the K shell excitation energies of Mo and L-shell of excitation energies of Au are suitable for X-ray focusing optics like polycapillary lens. The max voltage of typical laboratory X-ray sources is 50 kVp which is enough to produce K-shell and L-shell emission of Mo and Au, respectively. The high biocompatibility of these NPs allows for greater injection doses with less concerns of cell toxicity which makes it feasible for these NPs to act as both CT contrast agents and functional imaging contrast agents [69, 70]. For many cancer imaging applications, the NPs are used as passive targeting agents due to the enhanced permeability and retention (EPR) effects of the tumor [54]. AuNPs have been extensively investigated due to their high affinity ligands which have led to dose enhancements in radiation cancer treatment [70-73].

1.6 Joint XLCT and XFCT imaging

XLCT imaging employs nanophosphors which emit optical photons upon X-ray excitation. Typically, these nanophosphors are composed of high Z elements. As discussed in the previous section, high Z particles undergo X-ray fluorescence if the incident X-ray energy is above the K-edge or L-edge of the particle material. In a dual modality configuration with XLCT and XFCT imaging, the characteristic emissions from XRF allow for high resolution imaging while the optical emissions from XRL allow for high sensitivity imaging. In a 2018 dissertation by Quigley et al, a dual modality imaging of XLCT and XFCT imaging with a monochromatic 17.4 keV pencil beam X-ray source was numerically and experimentally presented to reconstruct the distribution of $Y_2O_3:Eu^{3+}$ in a 5 x 5 x 1.6 cm gel phantom [74]. The joint image reconstruction employed a 1D Richardson-Lucy deconvolution method in which XRL is only registered to regions of the excitation line which detected XRF. The results showed an increase in contrast with the dual modality compared with XFCT alone.

1.7 Dissertation Outline

In the following chapters, I discuss advancements made towards preclinical functional X-ray imaging methods.

Chapter 2 discusses the feasibility of a time domain X-ray luminescence computed tomography (tdXLCT) imaging system [75]. The problem framework is presented, and results are compared to conventional CW XLCT imaging. A preliminary experimental study in which X-ray pulses and $GOS:Eu^{3+}$ optical pulses were measured is also presented at the end of the chapter.

Chapter 3 discusses the improvements in XFCT imaging with the use of a superfine quasi-monochromatic source [76]. Various detector setups on a radial distance from the

imaging object are compared. A proposed image reconstruction algorithm using the structural guidance of the pencil beam is compared with popular algorithms: Maximum likelihood expectation maximization (MLEM) and filtered back projection (FBP). A preliminary experimental study of an XFCT system with a superfine pencil beam is also presented at the end of the chapter.

Chapter 4 discusses the dose concerns associated with pencil beam XLCT imaging and provides a radiation dose estimation method for pencil beam XLCT imaging [77]. The dose deposited on the internal structures of a mouse from a conventional XLCT imaging protocol is reported.

Chapter 5 discusses a method to correlate the X-ray tube current exposure time and X-ray photon number in GATE [78]. To our knowledge, no other methods have been reported which accurately estimate the dose from a given tube current exposure.

Finally, Chapter 6 concludes the dissertation work and provides a discussion for future works in functional X-ray imaging. TOF-CT imaging and Speckle-based phase contrast imaging are explored with Monte Carlo software.

CHAPTER 2

TIME DOMAIN XLCT IMAGING

2.1 Introduction

X-ray luminescence computed tomography (XLCT) is an emerging hybrid imaging modality, in which high energy X-ray photons are used to excite X-ray excitable nanophosphors which emit optical photons measured for optical tomographic imaging [25]. The XLCT imaging is an intrinsic optical imaging with high measurement sensitivity and uses the known X-ray excitation region as anatomical guidance for high spatial resolution when imaging deep targets inside tissues [79, 80]. So far, several XLCT systems have been proposed and validated with numerical simulations and experimental studies [20, 28, 29, 81]. Currently, all XLCT systems work in a mode of continuous sampling, in which continuous-wave (CW) X-ray photons are used to excite fluorophores and the emitted optical intensity data is acquired for image reconstruction. Therefore, these CW XLCT systems do not have the ability for lifetime imaging which is related to many micro-environmental parameters such as oxygen concentration, temperature, and pH value, etc.

Up to now, many different techniques including time domain (TD) and frequency domain (FD) solutions have been well developed to measure fluorescent lifetimes [82-84]. Although fast FD optical imaging systems have been commercially available, TD imaging methods, especially the time-correlated single photon counting (TCSPC) technique, which has better timing resolution, is the gold standard for high precision fluorescence lifetime imaging, due to its measurement accuracy [85, 86]. Although the lifetime is independent of the depth, the spatial resolution of TD fluorescence imaging is also degraded by the strong optical scattering when imaging deep targets.

While like fluorescence lifetime imaging, phosphorescence lifetime imaging exhibits long luminescent lifetimes greater than fluorescent lifetimes due to their long-lived excited triplet states. Combined with time gating techniques, acquisition of these long emission lifetimes eliminates background fluorescence noise and overall improves the signal-to-noise ratio (SNR) of the phosphorescent lifetime signal [87]. Lifetime information serves as probe for detection and visualization of biomolecules in tissue [88]; analysis of the lifetime signal with fractional calculus establishes correlations between the lifetime of the excited nanophosphor and the biomolecule. For example, phosphorescent lifetimes are sensitive to oxygen levels [87]; the long-lived excited state of the nanophosphor provides enough time for collisional interactions to occur between the nanophosphor and oxygen thus decreasing the lifetime. Oxygen concentrations are vital for radiation therapy since tumors in a hypoxic state become unresponsive to radiation treatment. Monitoring oxygen levels of tumors before and during therapy could improve radiation treatment results. Other applications of lifetime imaging allow for quantitative measurements of zinc, calcium, and pH in cells [89, 90]. Zinc is responsible for proper functioning and folding of proteins and

are cofactors of viral proteins [91]. Calcium plays a significant role in signal transduction pathways and measurements of calcium in tissue could further advance studies in diseases such as Alzheimer's disease [92]. Homeostasis of pH is critical for regular cell metabolic functionalities, and lifetime imaging could record pH level fluctuations due to environmental changes within the cell [93]. The proposed time domain XLCT (tdXLCT) system has the potential to provide luminescent lifetime information of these biomolecules with high spatial resolution and sensitivity.

In this study, a fiber-based tdXLCT system design is presented in which a pulsed, superfine X-ray beams is used to excite phosphors, and time resolved optical signals are detected by a photomultiplier tube (PMT) coupled to a TCSPC unit. The superfine X-ray beams, used as anatomical guidance in the time domain XLCT reconstruction, make it possible to have high spatial resolution lifetime imaging. The feasibility of this design is demonstrated through numerical simulations.

This chapter is organized as follows. In section 2.2, the methods are presented, including the time domain XLCT imaging system design, the forward model, the reconstruction algorithms, numerical simulation setup, and the imaging evaluation criteria. Then, the numerical simulation results are presented in section 2.3. Section 2.4 presents a preliminary experimental study in which X-ray pulses and GOS:Eu^{3+} optical pulses were measured. The chapter ends with discussion and conclusion in section 2.5.

2.2 Methods

2.2.1 Time domain XLCT system

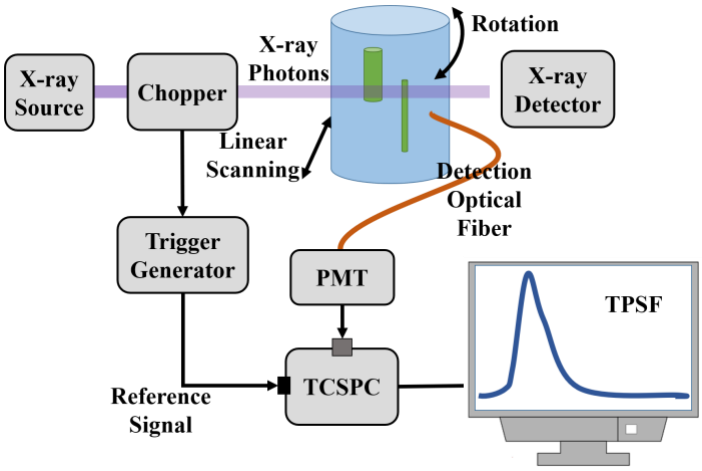

Figure 2.1: Schematic of the proposed time domain XLCT system.

The schematic of the proposed time domain XLCT imaging system is plotted in Figure 2.1. A focused X-ray tube (Polycapillary X-Beam Powerflux, XOS, New York; target metal: molybdenum (Mo)) is utilized to generate X-ray photons. A chopper system, which is like an optical chopper (MC2000B, Thorlabs, USA), chops the focused X-ray beam with a chopping frequency about 1 kHz. With the focusing X-ray beam diameter less than 100

micrometers, the X-ray pulse width is expected to be less than 1 microsecond. Meanwhile, the synchronous signal of the chopper system is acquired by a trigger generator and serves as the reference signal for the TCSPC device (SPC-130, Becker & Hickl, Germany). Phantoms or other objects for imaging are placed on a motorized rotation stage (B4872TS-ZR, Velmex, Inc., New York), which is mounted on a motorized linear stage (MB2509Q1J-S3, Velmex, Inc., New York). The scanning X-ray beam pass through objects and is then detected by an X-ray detector (Shad-o-Box 1024, GOS scintillator screen, Rad-icon Imaging Corp., California) with a detection area of $49.2 \times 49.2\ \mathrm{mm}^2$ consisting of a 1024×1024 pixel photodiode array sensor with a 48 μm pixel size. The X-ray detector measures the intensity of the X-ray beam, from which the phantom boundary is detected. The emitted optical photons from the phantom side surface are collected by a 2 meters long fiber bundle with an aperture diameter of 3 mm. The fiber bundle is fixed by a mount frame that moved and rotated with the phantom or the object being scanned. A fan-cooled photomultiplier tube (PMT) photon counting head (PMC-100, Becker & Hickl, Germany) is coupled to the TCSPC module for acquiring the time-resolved flux, *i.e.*, the temporal point spread function (TPSF). The measurement data is stored and displayed in a personal computer (PC).

2.2.2 Laplace transform based time domain XLCT algorithm

In this study, the generalized pulse spectrum technique (GPST) method is applied to convert the real domain optical diffusion forward model into its Laplace transform, following the similar approach described in Ref. [94] for time domain fluorescence molecular tomography (FMT). In time domain XLCT, let $\Phi(\mathbf{r}, \mathrm{p}) = \int_0^{+\infty} \Phi(\mathbf{r}, \mathrm{t}) \mathrm{e}^{-\mathrm{pt}} \mathrm{dt}$ be the Laplace transform of the time-dependent photon density $\Phi(\mathbf{r}, \mathrm{p})$ at position $\mathbf{r}$ in domain Ω at time t for a complex transform factor p. The Laplace-transformed photon diffusion equation is accordingly written by the following equation:

$$\begin{cases} [\nabla \cdot \mathrm{D}(\mathbf{r})\nabla - \mu_{\mathrm{a}}(\mathbf{r})\mathrm{c} - \mathrm{p}]\Phi(\mathbf{r}, \mathrm{p}) = -\mathrm{S}_{\mathrm{k}}(\mathbf{r}, \mathrm{p}), \mathbf{r} \in \Omega \\ \mathrm{c}\Phi(\mathbf{r}, \mathrm{p}) + 2\mathrm{KD}(\mathbf{r})\mathbf{e}_{\mathrm{n}} \cdot \nabla\Phi(\mathbf{r}, \mathrm{p}) = 0, \mathbf{r} \in \partial\Omega \end{cases} \tag{2.1}$$

where $\mu_{\mathrm{f}}(\mathbf{r})$ is the absorption coefficient of the media, c is the velocity of light in the media, $\mathrm{D}(\mathbf{r}) = \left[3\left(\mu_{\mathrm{a}}(\mathbf{r}) + \mu'_{\mathrm{s}}(\mathbf{r})\right)\right]^{-1}$ is the diffusion coefficient, $\mu'_{\mathrm{s}}(\mathbf{r})$ is the reduced scattering coefficient, $\mathbf{e}_{\mathrm{n}}$ is the outward unity vector normal to the surface $\partial\Omega$, $\mathrm{K} = (1 + \mathrm{R_f})/(1 - \mathrm{R_f})$ is the Robin boundary condition coefficient, $\mathrm{R_f}$ is the internal reflection coefficient at the boundary, and ∇ is the gradient coefficient. $\mathrm{S_k}(\mathbf{r}, \mathrm{p})$ is the source term which stands for the k^{th} X-ray beam illumination pattern and can be written as:

$$\mathrm{S_k}(\mathbf{r}, \mathrm{p}) = \mathrm{T_k}(\mathbf{r}) \frac{\eta\mu_{\mathrm{af}}(\mathbf{r})}{1 + \mathrm{p}\tau(\mathbf{r})} \tag{2.2}$$

where $T_k(\mathbf{r})$ is the X-ray intensity distribution, η is the quantum efficiency, and $\mu_{af}(\mathbf{r})$ is the absorption coefficient. In Equation 2.2, the light yield $\eta\mu_{af}(\mathbf{r})$ and the lifetime $\tau(\mathbf{r})$ are the phosphorescent nanoparticle properties to be reconstructed.

In XLCT, while an X-ray beam scans the object along a straight line, the X-ray beam intensity distribution along the scanning line follows the Beer-Lambert law. If a uniform X-ray attenuation medium is assumed, $T_k(\mathbf{r})$ can be expressed as:

$$T_k(\mathbf{r}) = T_0 \exp\left(-\mu_x(\mathbf{r}) \times L(\mathbf{r})\right) \tag{2.3}$$

where T_0 is the initial X-ray beam intensity, $\mu_x(\mathbf{r})$ is the X-ray attenuation coefficient at the position $\mathbf{r}$, and $L(\mathbf{r})$ is the distance from X-ray beam start position to current position $\mathbf{r}$.

Based on the finite element method (FEM), the forward model of the time domain XLCT can be expressed as [95]:

$$\mathbf{A}_{n_d \times I \times J, m}(p)\mathbf{x}_{m,1}(p) = \mathbf{b}_{n_d \times I \times J, 1}(p) \tag{2.4}$$

where n_d is the number of detector nodes, I is the total number of angular projections, J is the number of linear scan for each projection, and m is the finite element mesh node number. The intermediate quantity is defined: $x(\mathbf{r}, p) = \eta\mu_{af}(\mathbf{r})/[1 + p\tau(\mathbf{r})]$. Let $x(\mathbf{r}, p) \approx \sum_{n=1}^{m} x_n(p)u_n(\mathbf{r}) = \mathbf{x}^T(p)\mathbf{u}(\mathbf{r})$ with $\mathbf{u}(\mathbf{r}) = [u_1(\mathbf{r}), u_2(\mathbf{r}), \dots, u_m(\mathbf{r})]^T$ and $\mathbf{x}(p) = [x_1(p), x_2(p), \dots, x_m(p)]^T$ being the shape functions and the unknowns, respectively. $\mathbf{b}$ is the measurement, and $\mathbf{A}$ is the system matrix that can be calculated as:

$$A_{n_d \times I \times J, m}(p) = \begin{bmatrix} \begin{bmatrix} \Phi_1(p) \\ \vdots \\ \Phi_{nd}(p) \end{bmatrix} \otimes \Gamma_1 \otimes T_1 \\ \vdots \\ \begin{bmatrix} \Phi_1(p) \\ \vdots \\ \Phi_{nd}(p) \end{bmatrix} \otimes \Gamma_{I \times J} \otimes T_{I \times J} \end{bmatrix} \tag{2.5}$$

in which $\otimes$ is the element product of row vectors Φ_i, Γ_j and T_j where $i \in [1, n_d]$ and $j \in [1, I \times J]$. $[\Phi_1(p), \Phi_2(p), \dots, \Phi_{n_d}(p)]^T$ is the sensitivity matrix where each row vector Φ_i is solved by Equation 2.1 when setting the detector node i to be 1. T_j is the excitation vectors from X-ray beam illumination patterns. In XLCT, the excitation regions have the known locations along the X-ray beam and can be described as:

$$\Gamma_j(s) = \begin{cases} 1, \text{node } s \text{ is within the X} - \text{ray beam} \\ 0, otherwise \end{cases} \tag{2.6}$$

The XLCT reconstruction can be solved like in FMT [96-98]. The solution of Equation 2.4 can be obtained by minimizing the following regularized squared measurement misfit under the non-negativity constraint:

$$\mathbf{x}(\mathrm{p}) = \underset{\mathbf{x}\geq\mathbf{0}}{\mathbf{argmin}}\, \mathrm{F}\big(\mathbf{x}(\mathrm{p})\big) := \frac{1}{2}\big|\big|\mathbf{b}(\mathrm{p}) - \mathbf{A}(\mathrm{p})\mathbf{x}(\mathrm{p})\big|\big|_2^2 + \alpha\big|\big|\mathbf{x}(\mathrm{p})\big|\big|_{\mathrm{q}}^{\mathrm{q}} \qquad (2.7)$$

where α is the regularization parameter and $||\mathbf{x}(\mathrm{p})||_{\mathrm{q}}^{\mathrm{q}}(\mathrm{q} \geq 0)$ is the L^{q} norm term. In this work, the majorization-minimization (MM) algorithm is applied to minimize the L^1 regularized mismatch between the measurements and the modeled values by updating the images iteratively. The details of the MM algorithm have been described elsewhere [97, 98].

The two unknown distributions, the phosphorescent yield and the lifetime of the phosphor particles can be explicitly recovered from the images of $\mathbf{x}(\mathbf{r}, \mathrm{p}_1)$ and $\mathbf{x}(\mathbf{r}, \mathrm{p}_2)$ by employing a pair of transform factors $(\mathrm{p}_1, \mathrm{p}_2)$ in the Laplace transforms:

$$\begin{cases} \eta\mu_{\mathrm{af}}(\mathbf{r}) = \dfrac{(\mathrm{p}_1 - \mathrm{p}_2)\mathrm{x}(\mathbf{r}, \mathrm{p}_1)\mathrm{x}(\mathbf{r}, \mathrm{p}_2)}{\mathrm{p}_1\mathrm{x}(\mathbf{r}, \mathrm{p}_1) - \mathrm{p}_2\mathrm{x}(\mathbf{r}, \mathrm{p}_2)} \\ \tau(\mathbf{r}) = -\dfrac{\mathrm{x}(\mathbf{r}, \mathrm{p}_1) - \mathrm{x}(\mathbf{r}, \mathrm{p}_1)}{\mathrm{p}_1\mathrm{x}(\mathbf{r}, \mathrm{p}_1) - \mathrm{p}_2\mathrm{x}(\mathbf{r}, \mathrm{p}_2)} \end{cases} \qquad (2.8)$$

where the transform factors are:

$$\mathrm{p}_{1,2} = \pm\frac{\mathrm{k}}{\left(\dfrac{2}{\mu_{\mathrm{a}}^{(\mathrm{B})}\mathrm{c}}\right) + \tau^{(\mathrm{B})}}, (0 \leq \mathrm{k} \leq 1) \qquad (2.9)$$

in which, $\mu_{\mathrm{a}}^{(\mathrm{B})}$ and $\tau^{(\mathrm{B})}$ are the background optical absorption and lifetime coefficients. The transform factors p_1 and p_2 are two specific transform factors of p as defined in Equation 2.8. In this study, only a pair of transform factors are used.

2.2.3 Numerical Simulation Studies

To validate the proposed time domain XLCT imaging system and algorithms, numerical simulations with a three-target phantom were performed. To simulate the proposed imaging system, measurements were recorded with one optical fiber bundle. A 10 mm long cylindrical phantom with a diameter of 13 mm was used. The optical properties of the phantom were set to be $\mu_{\mathrm{a}}^{(\mathrm{B})} = 0.0072\ \mathrm{mm}^{-1}$ and $\mu'^{(\mathrm{B})}_{\mathrm{s}} = 0.72\ \mathrm{mm}^{-1}$, while the phosphorescent properties were $\eta\mu_{\mathrm{af}}^{(\mathrm{B})} = 0.001\ \mathrm{mm}^{-1}$ and $\tau^{(\mathrm{B})} = 1$ ps.

In numerical simulations, a normalized X-ray beam intensity was adopted. Therefore, the X-ray intensity at the entry to the phantom (T_0) was assumed to be equal to 1. The X-ray attenuation coefficient was $\mu_x = 0.0214\ \mathrm{mm}^{-1}$ in the phantom. Then, the X-ray intensity along the X-ray beam in the phantom is given by the following equation:

$$T_k(\mathbf{r}) = \exp(-0.0214 \times L(\mathbf{r})) \tag{2.10}$$

where $L \in [0, 13]$ was the distance from one side to another side of the phantom.

All the three-targets had a diameter of 0.4 mm and a height of 6 mm and were embedded in the phantom. The positions of the targets are shown in Figure 2.2. The target center-to-center distance (CtCD) was 0.8 mm. For numerical study, the phosphor particle concentration was 1 mg/mL in the targets and 0 mg/mL (no phosphors) in the background. The targets were divided in two groups: Group #1 including T1 and T2; Group #2 including T3. The optical properties and phosphorescent parameters of the imaging object and targets are shown in Table 2.1.

Table 2.1: Optical and phosphorescent parameters of the phantom and targets

Items	μ_a [mm^{-1}]	μ'_s [mm^{-1}]	$\eta\mu_{af}$ [mm^{-1}]	τ [ps]
Background	0.0072	0.72	0.001	1
Group 1	0.0072	0.72	0.005	400
Group 2	0.0072	0.72	0.003	600

The fiber bundle was placed at 3 mm under the phantom top surface. The relative position of fiber bundle to the phantom was fixed. During the experiments, the fiber bundle and the phantom translated and rotated together. A focused X-ray beam was used to scan the phantom at a depth of 5 mm. The focused X-ray beam diameter and the linear scan step size were set to be 100 μm. Six angular projections with an angular step size of 30 degrees were used. For each projection, 130 measurements were collected. The numerical measurements were generated from the forward model, in which the phantom was discretized by a finite element mesh with 26,638 nodes, 153,053 tetrahedral elements, and 11,456 face elements. Finally, 1% Gaussian noise was added to the numerical measurements.

2.2.4 Evaluation Criteria

Two criteria were used to evaluate the quality of the reconstructed images, as described in Ref. [99].

Center-to-center distance error (CDE): For multiple target imaging, CDE was defined as the distance error ratio between the reconstructed targets and the true targets and is given by

$$\mathrm{CDE} = \frac{2 \times |\mathrm{Dist_r} - Dist_t|}{\mathrm{Dist_r}} \times 100\% \tag{2.11}$$

where $Dist_r$ and $Dist_t$ are the CtCD between the reconstructed targets and the true targets, respectively. $Dist_r$ is also calculated from the cross target profile plot using the full width at half maximum (FWHM) approach.

Dice similarity coefficient (DICE): DICE is used for comparing the similarity between the reconstructed and true targets and is given by

$$\mathrm{DICE} = \frac{2 \times |\mathrm{ROI_r} \cap \mathrm{ROI_t}|}{|\mathrm{ROI_r}| + |\mathrm{ROI_t}|} \times 100\% \tag{2.12}$$

where ROI_r is the reconstructed region of interest that is defined to be the pixels whose intensities are higher than 20% of the maximum pixel intensity. Generally, the closer DICE is to 100%, the better.

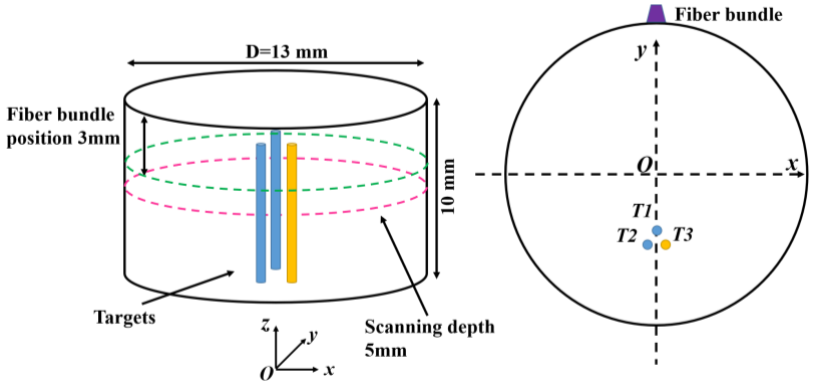

Figure 2.2: The phantom geometry and fiber bundle position for numerical simulation with three targets.

2.3 Result of numerical simulations

The scanned transverse section was discretized with a two-dimensional (2-D) grid having a pixel size of $\mathbf{25 \times 25\ \mu m^2}$. The system matrix generated with the finite element mesh was interpolated to the fine 2-D grid. During the reconstruction, the L^1 regularization method was applied using the MM algorithm reconstruction framework to solve the optimization problem. Figure 2.3 shows the results for numerical simulations of three targets. In Figure 2.3A, the reconstructed time domain XLCT phosphorescence images are plotted. Figure 2.3B shows the zoomed in target region, where the green circles represent the true targets' size and locations. From the reconstructed images, the three targets were reconstructed successfully and were clearly resolved for phosphorescence yield and lifetime properties, respectively. To further analyze the reconstructed XLCT image quantitatively, the image quality metrics are shown in Table 2.2. From the dotted blue line

in Figure 2.3B, line profiles are plotted in Figure 2.3C. From the FWHM, the reconstructed target size was calculated to be 0.4249 mm with a target size error (TSE) of 6.23% and 0.4222 mm with a TSE of 5.54% for phosphorescence yield and lifetime, respectively. In addition, the CtCD of yield and lifetime are 0.7769 and 0.7742 mm with errors of 2.89% and 3.23%, and DICE were evaluated to be 89% and 87.62% for yield and lifetime, respectively. Based on our results, the lifetime and yield of multiple targets deeply embedded inside tissues can be successfully reconstructed simultaneously using time resolved data.

To see how robust the proposed time domain XLCT imaging algorithm is to different measurement noises from 1% to 10%, different Gaussian white noises were added onto the numerical measurements and ran the reconstruction with a fixed projection number of 6. The image quality metrics for the reconstructed lifetime images and yield images are listed in Table 2.3. Reconstruction using lifetime data with noise levels of 1% and 2% resulted in equivalent CtCD of 0.7769 mm with 2.89% error. At 5% noise level, the CtCD was 0.7755 mm with 3.06% error. At the largest noise level of 10%, the CtCD was evaluated at 0.9515 mm with 18.94% error. DICE coefficients remained larger than 86% in noise levels 1%, 2%, and 5%. For noise level of 10%, the DICE coefficient decreased to 27.53%. The reconstructed yield images resulted in similar DICE coefficients to those utilizing lifetime images, but the lowest DICE coefficient was 85.14% at the greatest noise level. The DICE coefficients at noise levels 1%, 2% and 5% did not fluctuate significantly from 86%. In addition, the lowest CDE of 1.17% occurred at 1% noise level while the greatest CDE of 27.64% occurred at 5% noise level. At noise levels 2% and 10%, CtCD were generated at 0.5844 mm with 26.95% error and 0.6187 mm with 22.66% error respectively.

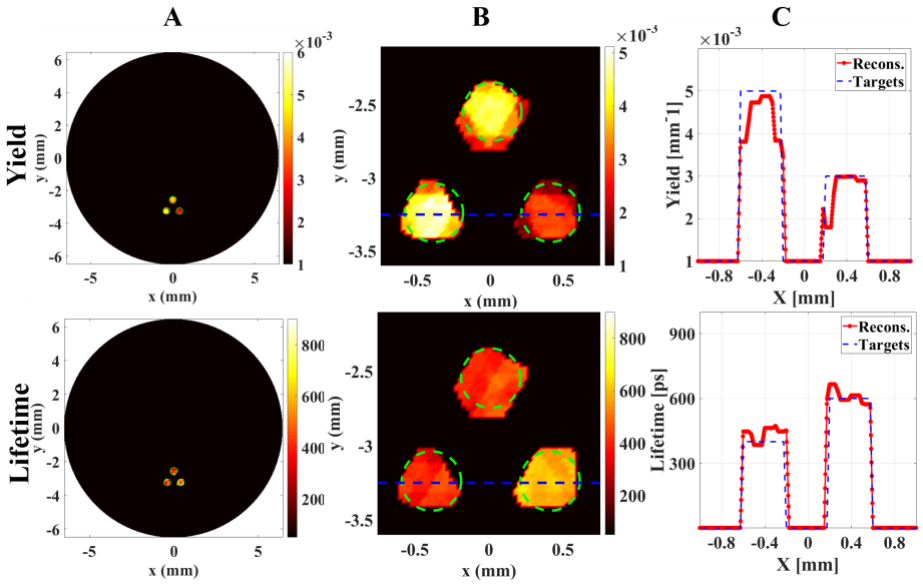

Figure 2.3: The reconstruction results of phosphorescence yield (top) and lifetime (bottom) for three targets numerical simulation. A: The reconstructed phosphorescence yield and lifetime images, respectively; B: Zoomed in regions of reconstructed targets, the green dotted line indicates the exact target size and position, the blue dotted line indicates the profile location; C: profile plots across target T2 and target T3.

Table 2.2: Quantitative imaging quality metrics for the numerical simulation with three targets.

	Diameter (mm)/TSE	CtCD (mm)/CDE	DICE
Yield	0.4249/6.23%	0.7906/1.17%	86.49%
Lifetime	0.4222/5.54%	0.7769/2.89%	86.50%

Additionally, lifetime and yield images were reconstructed with measurement data at different number of projections with a fixed noise level of 2% as shown in Figure 2.4. The image quality metrics for these results are listed in Table 2.4. The reconstructed lifetime images performed best with measurement data of projections 6 and 12 considering their high DICE coefficients of 87.62% and 86.15% and low CDE of 3.07% and 1.63%, respectively. From the reconstructed yield images, the DICE coefficients did not vary significantly with different projection numbers. The greatest DICE coefficient was calculated with 6 projections at 86.32%. The closest CtCD to the actual value was evaluated with 24 projections at 0.8016 mm with 0.20% error, while the greatest CtCD error arose from 3 projections at 1.0560 mm with 32.00% error.

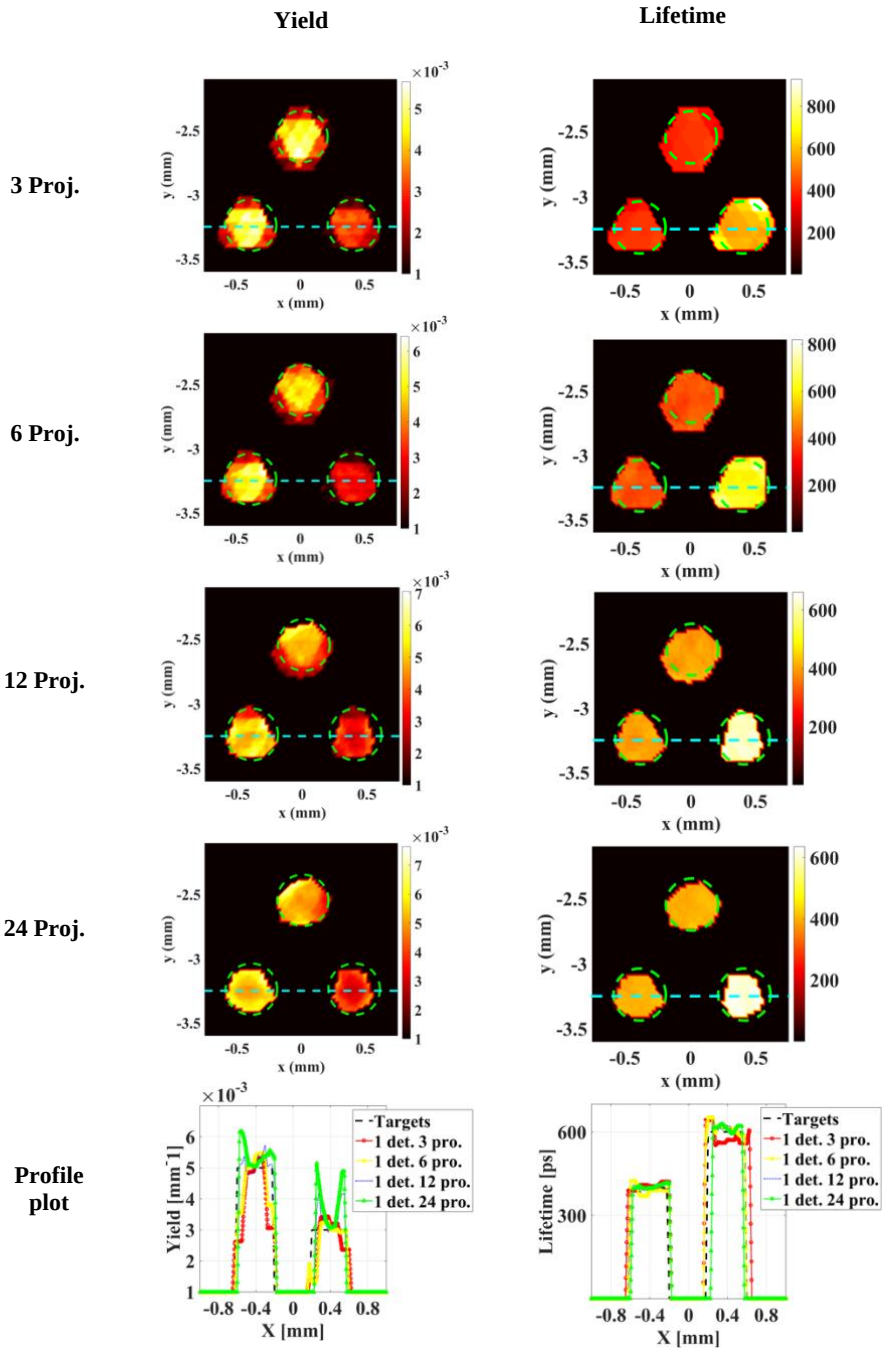

Figure 2.4: The zoomed regions of the reconstructed phosphorescence yield images and lifetime images for three targets numerical simulation with measurements at different projections. The dotted circles indicate the true target position and size. The bottom row shows the profile plots cross the bottom two targets where "1 det" indicates one detector used in the simulations.

Lastly, the robustness of the reconstructed lifetime and yield images to the unknown optical properties was investigated. In the forward model, the absorption coefficient was set to 0.0072 mm^{-1} and the reduced scattering coefficient was set to 0.72 mm^{-1}. In the reconstruction model, the optical properties were changed to be 2 times the absorption coefficient ($2*\mu_a$), 4 times absorption coefficient ($4*\mu_a$), and 2 times absorption coefficient plus 2 times reduced scattering coefficient ($2*\mu_a$ and $2*\mu_s'$). In these studies, a fixed noise level of 2% and a fixed projection number of 6 was used and their image quality metrics for the reconstructed lifetime and yield images are listed in Table 2.5. The reconstructed lifetime images seem independent of the optical properties of the imaged object with the same CtCD of 0.7769 mm with 2.89% error and same DICE coefficient of 86.50%. These results are very close to the numbers from the true optical properties. From Table 2.5, the reconstructed yield images resulted in slightly different metrics with respect to different optical properties. The lowest CDE of 1.52% occurred at $2*\mu_a$ and $2*\mu_s'$ with a CtCD of 0.7879 mm, and the greatest CDE of 27.81% occurred at $2*\mu_a$ with a CtCD of 0.5775 mm. DICE coefficients remained relatively constant at 86% for $2*\mu_a$, and $4*\mu_a$ while the greatest DICE coefficient was generated from $2*\mu_a$ and $2*\mu_s'$ at 87.05%.

Table 2.3: Quantitative imaging quality metrics for the numerical simulations with different noise levels

	Number of Projections	Noise	CtCD (mm)/CDE	DICE
Lifetime	6	1%	0.7769/2.89%	86.50%
	6	2%	0.7754/3.07%	87.62%
	6	5%	0.7755/3.06%	86.50%
	6	10%	0.9515/18.94%	27.53%
Yield	6	1%	0.7906/1.17%	86.49%
	6	2%	0.5844/26.95%	86.32%
	6	5%	0.5789/27.64%	86.58%
	6	10%	0.6187/22.66%	85.14%

Table 2.4: Quantitative imaging quality metrics for the numerical simulations with measurements of different projection numbers

	Number of Projections	Noise	CtCD (mm)/CDE	DICE
Lifetime	3	2%	0.8113/1.41%	84.32%
	6	2%	0.7754/3.07%	87.62%
	12	2%	0.7870/1.63%	86.15%
	24	2%	0.7878/1.52%	82.41%

Yield	3	2%	1.0560/32.00%	84.36%
	6	2%	0.5844/26.95%	86.32%
	12	2%	0.7906/1.17%	86.16%
	24	2%	0.8016/0.20%	83.35%

Table 2.5: Quantitative imaging quality metrics for the numerical simulations with mismatched optical properties. The first row indicates the true optical properties with μ_a=0.0072 mm^{-1} and μ_s'=0.72 mm^{-1}

	μ_a	μ_s'	CtCD (mm)/CDE	DICE
Lifetime	0.0072 mm^{-1}	0.72 mm^{-1}	0.7754/3.07%	87.62%
	2*0.0072 mm^{-1}	0.72 mm^{-1}	0.7769/2.89%	86.50%
	2*0.0072 mm^{-1}	2*0.72 mm^{-1}	0.7769/2.89%	86.50%
	4*0.0072 mm^{-1}	0.72 mm^{-1}	0.7769/2.89%	86.50%
Yield	0.0072 mm^{-1}	0.72 mm^{-1}	0.5844/26.95%	86.32%
	2*0.0072 mm^{-1}	0.72 mm^{-1}	0.5775/27.81%	86.72%
	2*0.0072 mm^{-1}	2*0.72 mm^{-1}	0.7879/1.52%	87.05%
	4*0.0072 mm^{-1}	0.72 mm^{-1}	0.5789/27.64%	86.39%

2.4 Preliminary Time Domain XLCT Experiment

2.4.1 Experimental Setup

The schematic and experimental setup of the tdXLCT system is shown in Figure 2.5. An XOS X-ray source (X-Beam Powerflux [Mo anode], XOS) is used to generate X-ray photons with 100 um beam size at the focal distance from the XOS polycapillary lens opening. The XOS source was operated at 50 kVp and 1 mA. An optical chopper system (300D30, Scitec Instruments) was positioned at the focal distance (44.9 mm) of the XOS source. The optical chopper contains a chopping disc with 102 mm diameter and 0.5 mm thickness. The chopper disc is composed of half hard brass to attenuate 99.9% of the X-rays when the X-ray beam is incident on the disc. While the chopper disc contains slits, the disc slit sizes would generate X-ray pulse lengths too great for the study objective. To generate X-ray pulse lengths suitable for this work, two 2 mm slits were drilled into opposing edges of the disc. The slits were drilled 180° from each other. The chopper disc is contained inside a steel case to prevent damage to the disc and to prevent damage to other nearby instrumentation as the disc can achieve very high speeds. The tdXLCT imaging system except the computer, oscilloscope, and chopper system control unit was contained in a light tight and X-ray shielding lead cabinet. X-ray pulses are generated as

the X-ray beam is chopped by the rotating disc slits. The X-ray pulse length was recorded at various chopper frequency settings without an imaging sample. The X-ray pulses were incident on a scintillator X-ray crystal in which the optical photons released through the scintillation process were fed into a PMT for recording. Next a cuvette with GOS:Eu^{3+} solution was positioned along the X-ray pulse trajectory. Upon X-ray pulse excitation, the GOS:Eu^{3+} nanophosphor emits isotropic optical photons. The emission of the optical photons is observed as an optical pulse since the X-ray pulse excitation is short lived. The optical pulse signal was collected with an optical fiber positioned 90° from the incident X-ray beam and fed into a second PMT.

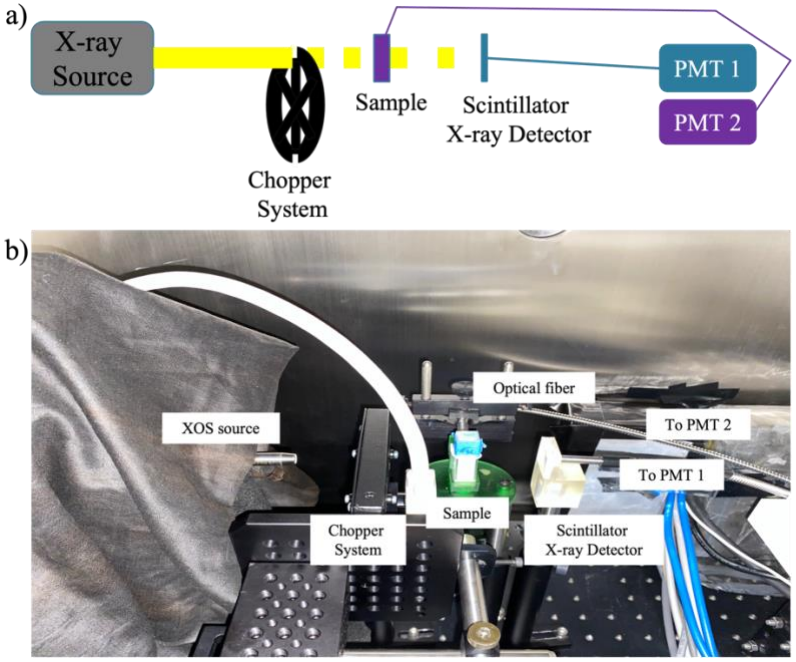

Figure 2.5: a) Schematic of the experimental tdXLCT imaging system with the imaged sample. b) Experimental setup of the tdXLCT imaging system with the GOS:Eu imaged sample. For the X-ray pulse measurements, the imaging sample would simply be removed from the imaging stage.

2.4.2 Results

Figure 2.6 shows the measurement results displayed in an oscilloscope screen for a sample with the X-ray pulse at chopper setting 2000. The top image shows a full view of the measurement window in which several pulses can be observed. The bottom image shows a zoom in view of a single X-ray pulse. Table 2.6 shows the X-ray pulse repetition, pulse frequency, and pulse width (length) at various chopper frequency settings: 500, 1000, 2000. As the chopper frequency setting is increased, the pulse frequency also increases while the pulse repetition and the pulse width decrease. At the max chopper setting (7,500), the pulse frequency is expected to be 234.38 Hz while the pulse width is expected to be 7.47 μs. Figure 2.7 shows a sample result of measuring the GOS:Eu^{3+} optical pulse. The top image shows a full view of the measurement window in which several optical pulses and excitation X-ray pulses can be observed. The yellow signal corresponds to the X-ray

pulses (PMT 1) while the blue signal corresponds to the GOS:Eu^{3+} optical pulses (PMT 2). The optical pulses are in line with the X-ray pulses. The bottom image shows a zoom in view of a single optical pulse and X-ray pulse. Table 2.7 shows the optical pulse length at various chopper frequency settings: 500, 1000, 2000. Compared to the X-ray pulse length, the optical pulse length is much longer lived (3x-18x). As the X-ray pulse repetition is increased, the optical pulse length increases significantly.

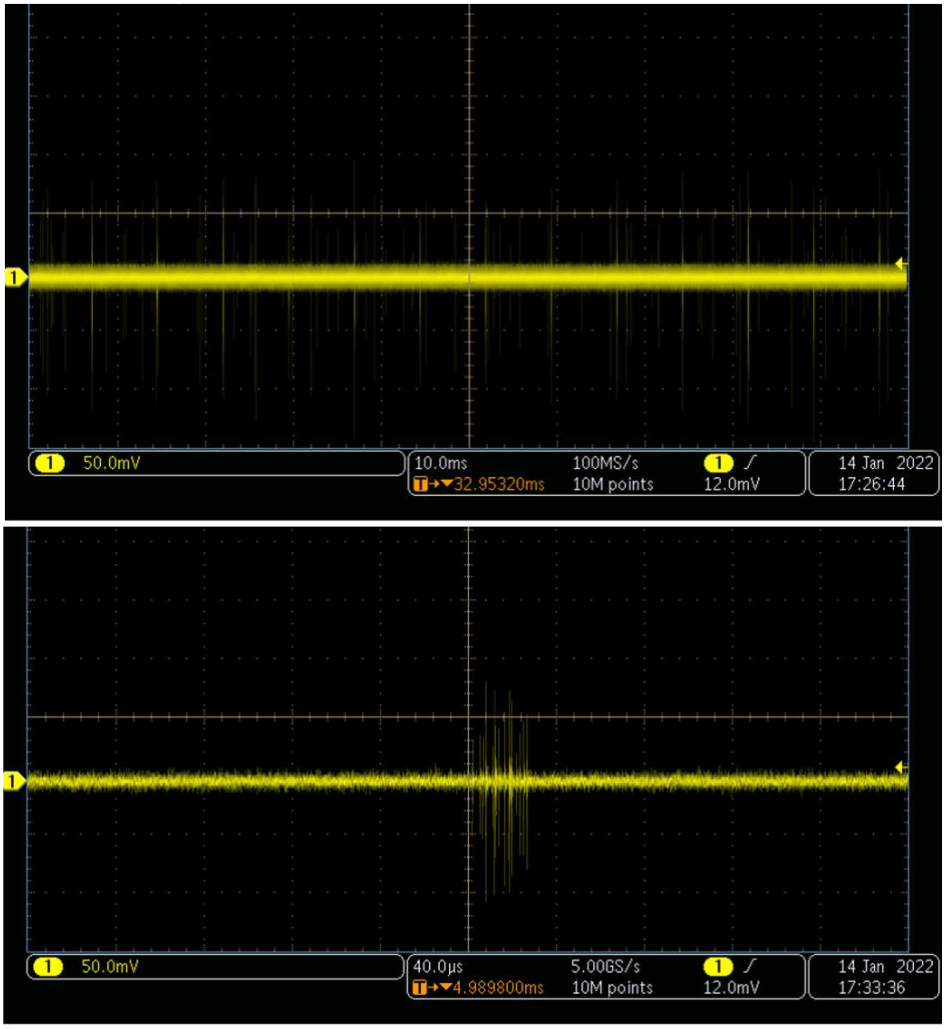

Figure 2.6: Sample measurement of the X-ray pulse at chopper setting 2000. (Top) Full view of the measurement window. (Bottom) Zoom in view of a single X-ray pulse.

Table 2.6: X-ray pulse measurements at various chopper frequency settings

Chopper Frequency Setting	Pulse Repetition (ms)	Pulse Frequency (Hz)	Pulse Width (µs)
500	32	15.63	120

1000	15	33.33	50
2000	8	62.50	28

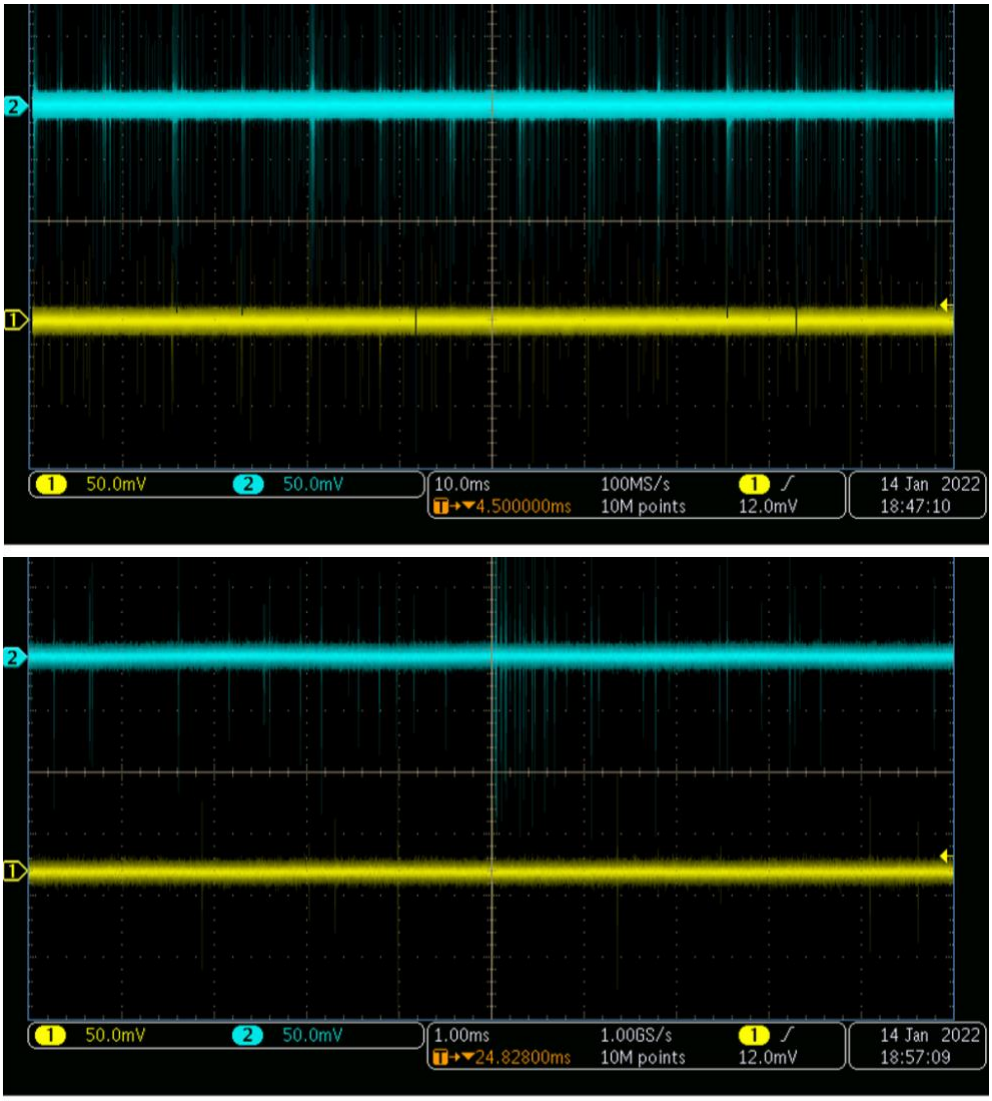

Figure 2.7: Sample measurement of the GOS:Eu^{3+} optical pulse at chopper setting 2000. (Top) Full view of the measurement window. (Bottom) Zoom in view of a single optical pulse. The yellow signal corresponds to the X-ray pulses while the blue signal corresponds to the optical pulses.

Table 2.7: Optical pulse measurements at various chopper frequency settings.

Chopper Frequency Setting	Pulse Repetition (ms)	Pulse Frequency (Hz)	Pulse Width (μs)
500	30	15.63	320

1000	15	33.33	400
2000	8	62.50	500

2.5 Discussion

In this study, a time domain XLCT system design, forward model, and reconstruction algorithm was proposed for the first time. High frequency pulsed X-ray photons are to be generated by using an optical chopper in the experimental design. The linear GPST method was applied to solve the optical diffusion forward model problem. In three-component target numerical simulation, three targets were successfully reconstructed. Furthermore, phosphorescence yield and lifetime distributions have been recovered simultaneously with good accuracy and resolution. Time domain methods usually take a relatively long scanning time, in the real system, several TCSPC modules can be employed to achieve multiple channel detection to reduce measurement time.

From the numerical simulation studies, the proposed time domain XLCT imaging system was found to be robust to measurement nose level up to 5% and to unknown optical properties. In particular, the reconstructed lifetime images are independent of the optical properties, which is a major advantage of the lifetime imaging due to the difficulty in estimating the optical properties of tissues.

A 20% of maximum threshold was applied when the DICE coefficient was calculated. It is also possible to apply a threshold of 10% maximum. Similar DICE coefficients for all cases were obtained except for the cases with noise level of 5%. It is feasible to use either 10% or 20% threshold in the future because the measurement noise should be less than 10%.

In this study, a pair of transform factors was used as shown in Equation 2.8. In the future, more transform factor pairs will be applied from the measured pulses, which should result in better image quality due to more measurement data as input for the reconstruction algorithm.

It is worth noting that the proposed time domain XLCT algorithm is a generic reconstruction algorithm that works for nanophosphors with a lifetime ranging from picoseconds to microseconds. In the numerical simulation studies, the lifetimes were arbitrarily chosen to be 0.400 and 0.600 nanoseconds, which are enough to validate our algorithm. However, the experimental system as described in Figure 2.1 might only work for measuring the lifetime less than hundreds of nanoseconds. For measuring nanophosphors with lifetimes around a few nanoseconds, an X-ray source like a free electron laser is needed which can generate X-ray pulses as short as a fraction of nanosecond [100].

The DICE dropped slightly when the measurement projection number increased as shown in Table 2.4. To figure out the reason, another set of numerical simulations with only one large target (5 mm in diameter) were performed at different projection numbers with a constant noise level. With the large target, this issue was not observed. A possible explanation is that our tdXLCT reconstruction is based on a finite element mesh and there

are partial volume issues due to the small target size. The reconstructed image quality can be improved substantially with more detectors instead of one detector as described in our simulations.

The proposed algorithm is a generic reconstruction algorithm that works well for both two-dimensional (2D) imaging and three-dimensional (3D) imaging. Due to the computational cost, the proposed system was demonstrated with 2D imaging. For 3D imaging, the imaging sample region of interest can be imaged slice by slice.

In the preliminary experimental tdXLCT study, a chopper system was used to chop the incident X-ray beam into X-ray pulses which excited the nanophosphor sample. The X-ray pulse length of a XOS source was measured and the optical pulse length of a GOS:Eu^{3+} solution was measured. At max chopper settings, the X-ray pulse width is expected to be 7.47 μs which offer the opportunity to explore time domain measurements with different nanophosphors. The GOS:Eu^{3+} optical pule lengths are longer lived than the X-ray pulses as seen in Figure 2.7 and Table 2.7. Since the GOS:Eu^{3+} optical pulse is longer lived, it becomes more difficult to distinguish between pulses as the chopper setting is increased. The increased frequency of X-ray pulse excitation may cause optical pulse signals to become mixed and create difficulties in measuring a single optical pulse. Due to the greater effective atomic number of the GOS:Eu^{3+} water mixture, the X-ray pulse is attenuated as seen between Figures 2.6 and 2.7. Since the GOS:Eu^{3+} is insoluble in water, the nanophosphors will settle in the mixture, therefore, the optical signal will decrease over time. It is best to create a nanophosphor agar mixture to prevent the GOS:Eu^{3+} particles from settling.

In future works, a trigger system will need to be incorporated into the proposed system to automate the capture of the optical pulse. This will help facilitate the measurement of the optical pulse especially when the optical pulse much longer lived compared to the X-ray pulse. The proposed trigger system would employ a laser which would be incident on the opposing disc slit. The chopped laser pulse would serve as the reference signal seen in Figure 2.1 which would be fed to the TCSPC system to acquire the TPSF. The imaging object and target will need to be composed of an agar/intralipid solution to prevent the GOS:Eu^{3+} particles from settling to the bottom of the container over time. Other nanophosphors like $(Gd,Y)_3(Ga,Al)_5O_{12}$:Ce and $(Gd,Lu)_3(Ga,Al)_5O_{12}$:Ce will be experimented with to explore the difference in the optical pulse widths and pulse decays. The pulse decay differences of different nanophosphors will be analyzed with microenvironmental parameters of interest like oxygen concentration.

2.6 Conclusion

In summary, a time domain XLCT imaging framework was proposed, and a set of numerical simulations were performed to validate the time domain XLCT imaging feasibility, which will guide the future design of an experimental time domain XLCT imaging system. A preliminary study was performed to prove the experimental feasibility of creating the X-ray pulses and optical pulses with a chopper system.

Acknowledgements: I would like to Dr. Wei Zhang who programmed the time domain XLCT imaging framework in MATLAB. I performed the numerical simulation using Dr. Zhang's MATLAB code and performed the data analysis and image reconstruction in this work. I was also responsible for performing the preliminary time domain XLCT measurement study.

CHAPTER 3

XFCT IMAGING WITH A SUPERFINE BEAM

3.1 Introduction

X-ray fluorescence computed tomography (XFCT) is a molecular imaging technique of X-ray photons, which can be used to sense different elements or nanoparticle agents inside deep samples or tissues. XFCT has been an active research topic for many years. XFCT imaging quantifies and maps the distribution of a high atomic number (Z) element of interest in objects. Many XFCT benchtop systems employ a cone beam source geometry, with pinhole detector collimation to reduce the imaging time and dose [73, 101-102]. However, the pencil beam geometry provides greater spatial resolution due to the radiation of a line rather than a volume at the cost of a longer scan time. Upon X-ray excitation, element specific characteristic X-rays are emitted from a target and then recorded. Ideally, multiple spectral detectors are configured to optimize the detected X-ray fluorescent signal and reduce the scan time and dose delivered to the imaging object [103].

As stated in Section 1.5, nanoparticles like Molybdenum (Mo) and Gold (Au) nanoparticles (NPs) have attracted significant attention in biomedical imaging. The K-shell emission energies of these NPs have greater penetrability which enables deeper functional tissue imaging. The high biocompatibility of MoNPs and AuNPs allows for greater injection doses with less concerns of cell toxicity which makes it feasible for the NPs to act as both CT contrast agents and functional imaging contrast agents [69, 70]. For many cancer imaging applications, the NPs are used as passive targeting agents due to the enhanced permeability and retention (EPR) effects of the tumor [70]. AuNPs have been extensively investigated due to their high affinity ligands which have led to dose enhancements in radiation cancer treatment [70-73].

A simple filtered back projection (FBP) reconstruction can be performed to obtain the X-ray fluorescent computed tomography (XFCT) image [39, 40, 104]. A popular iterative method to reconstruct the emission tomographic image is the maximum likelihood expectation maximization (ML-EM) algorithm [73, 101-103, 106]. Recently, a Nesterov accelerated MM algorithm with an L^1 regularization known as fNUMOS (fast NonUniform Multiplicative MM algorithm with Ordered Subsets acceleration) has shown success in X-ray luminescence computed tomography (XLCT) image reconstruction [76, 95] [14,15]. The MM algorithm with the Nesterov acceleration technique guarantees monotonicity and improves the convergence rate by limiting computational exhaustive matrix operations on the system matrix while promoting sparsity with the L1 regularization [98, 106] [16,17].

In this work, a benchtop XFCT imaging system is presented in which a quasi-monochromatic pencil beam X-ray source from Sigray Inc and a ring of spectrometers were simulated using GATE (Geant4 Application for Tomographic Emission) [107-109]. A quasi-monochromatic X-ray source spectrum was simulated due to the emergence of compact quasi-monochromatic sources in laboratory settings which enhance CT image

quality [110]. The X-ray propagation inside the media was modeled to construct the system matrix. The XFCT image of two MoNP targets with 2 mm diameter inside a cylindrical water phantom was reconstructed. The number of detectors used for the reconstruction was varied to show the detector number and position dependence on the reconstruction image quality. The images from the simulations were reconstructed using the fNUMOS algorithm and compared with the ML-EM and FBP algorithms. The target size was then reduced to show the capabilities of high spatial resolution imaging with the current setup. The angular projection number was also varied among 3, 6, and 10 projections, which are practically relevant projection numbers for pencil-beam XFCT imaging. To show the experimental feasibility of XFCT with a superfine pencil beam, a preliminary XFCT study was conducted with an X-ray source with 100 μm beam size. Two phantoms were used: a 12 mm diameter agar phantom with a 1%wt Au target, and a 20 mm diameter air phantom with three Au targets of varying concentrations, 0.1%wt, 0.5%wt, and 1%wt. The images were reconstructed with the fNUMOS algorithm.

This chapter is organized as follows. In Section 3.2, the methods of the GATE simulation using the unique Sigray source and ring detector configuration are presented. In Section 3.3, the results showing the effects of detector number and placement and the results comparing the fNUMOS reconstruction algorithm to ML-EM and FBP reconstructions are presented. Section 3.3 also shows the results of the high spatial resolution imaging in which the target size was reduced, and the angular projection number was varied. Section 3.4 provides a preliminary experimental study of an XFCT system with a superfine pencil beam. The chapter concludes with a discussion of the results and future works in Section 3.5.

3.2 Materials and Methods

3.2.1. GATE Simulation

The GATE Monte Carlo software was developed by the international OpenGATE collaboration as a GEANT4 wrapper that encapsulates the GEANT4 libraries specific to medical imaging and radiotherapy researchers [107-109]. GATE utilizes the macro language to ease the learning curve of GEANT4. The GEANT4 toolkits are more accessible to medical imaging and radiotherapy researchers which has allowed for the design and optimization of new medical imaging devices and radiotherapy protocols [107-109].

The GATE simulations in this work were parallelized and executed with a custom bash script on a 20 CPU workstation. The simulation wait time was approximately two days. The physics lists enabled in GATE consisted of the photoelectric effect, Compton scattering, and Rayleigh scattering, which are the primary physics processes accounted for in XFCT imaging. To observe characteristic X-rays, atom de-excitation was enabled under the photoelectric effect process. The GATE software stores all output as ROOT files [111]. The necessary data from the ROOT output file was extracted using custom C++ code and processed in MATLAB. The extracted data consisted of the detector element number, the deposited energy, and the angular projection number. The number of data sets needed were equal to the number of linear translations.

A schematic of the GATE simulation setup along with a GATE simulation snapshot is seen in Figure 3.1. For demonstration purposes, only 10 X-ray photons are shown in the GATE simulation snapshot. A 30 mm diameter cylindrical water phantom was positioned at the center of the reference frame. Two targets (T1, T2) with uniform 5 mg/mL and 10 mg/mL concentrations of MoNPs were embedded offset from the phantom center with the 5 mg/mL target (T1) closest to the phantom surface. The targets had a diameter and an edge-to-edge distance of 2 mm.

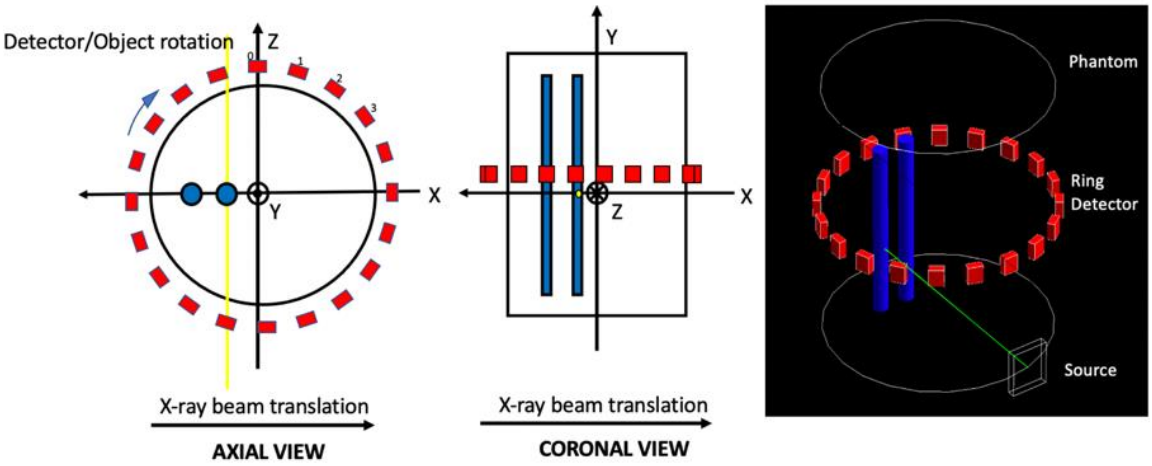

Figure 3.1: Axial view, coronal view, and snapshot (right) of the XFCT simulation setup in GATE. The axial view shows the X-ray beam as a yellow line and the coronal view shows the X-ray beam as a yellow dot near the center of the reference frame. The snapshot shows the trajectory of the X-ray photons as green lines.

The detector ring had a diameter of 31 mm and consisted of 20 cadmium zinc telluride (CZT) elements. A detailed schematic of the ring detector is seen in Figure 3.2. Each detector element had dimensions of $2 \times 2 \times 1$ mm^3. The X-ray beam size along the x-axis was 100 µm. The pencil beam had a divergence angle of 0.05°. A total of 10^7 X-ray photons per step were initialized. The X-ray beam scanned 2 mm below the detector ring. The linear step size was 125 µm; therefore, 248 linear steps were acquired to cover the phantom diameter and phantom edge. Six angular projections were acquired with a 30° angular step size. In this setup, the detector ring was allowed to rotate with the phantom about the center of the reference frame, whereas the X-ray beam translated linearly only.

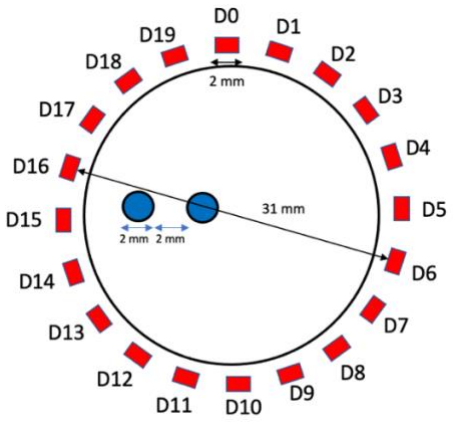

Figure 3.2: Schematic of the cadmium zinc telluride (CZT) ring detector.

The object was scanned by a modeled Sigray source from Sigray, Inc. The Sigray source was modeled using the linear interpolation user spectrum tool from GATE. The energy of the emitted photon is determined according to a probability distribution created by piecewise-linear interpolation between the energies provided. The modeled Sigray source spectrum is seen in Figure 3.3. The details of the source can be found at (https://sigray.com, accessed on 15 May 2021). In summary, the target anode and the company's optics allow for an X-ray flux of up to 10^9 photons per second. The target anode is composed of a silver microstructure encapsulated in a diamond substrate, which allows for a higher heat load limit and thus greater bombardment of electrons. The company optics consist of a monocapillary lens, which allows for a clean, low-energy cut off.

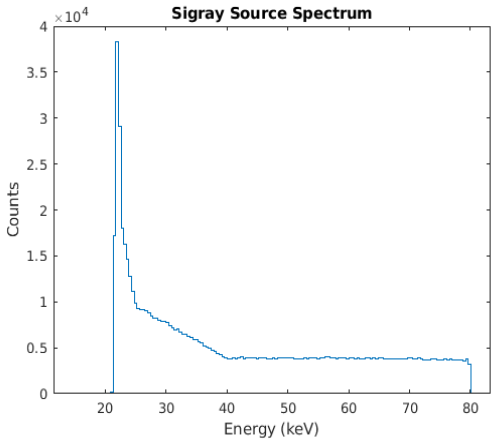

Figure 3.3: X-ray spectrum of a typical X-ray source from Sigray, Inc.

Before generating the X-ray fluorescent sinogram for reconstruction, the removal of scattered X-ray photons was applied on each measurement at each linear scan step by fitting X-ray photon energies in an 8 keV energy window. The 8 keV energy window was centered on the brightest fluorescent peak of the target element, which was 17.48 keV. A 4th-order polynomial was used to fit the scattered X-ray spectrum (the scattered X-ray source

energy), which was subtracted from the measured energy spectrum to obtain the measured X-ray fluorescent photon energy spectrum. An example of the removal is seen in Figure 3.4a. The net counts curve was shifted downward to avoid overlap with the total count curve for better view. Due to the unique spectrum of the Sigray source, little to no scattering was observed in the 8 keV energy window. Figure 3.4b is a zoomed-in version of Figure 3.4a, which focuses on the energy range of the MoNP fluorescent energy. Only the counts bounded by the red dashed vertical lines were collected for the sinogram. The width between the red dashed vertical lines corresponds to the energy resolution of the detector elements, which was 200 eV. The sinogram is seen in Figure 3.4c.

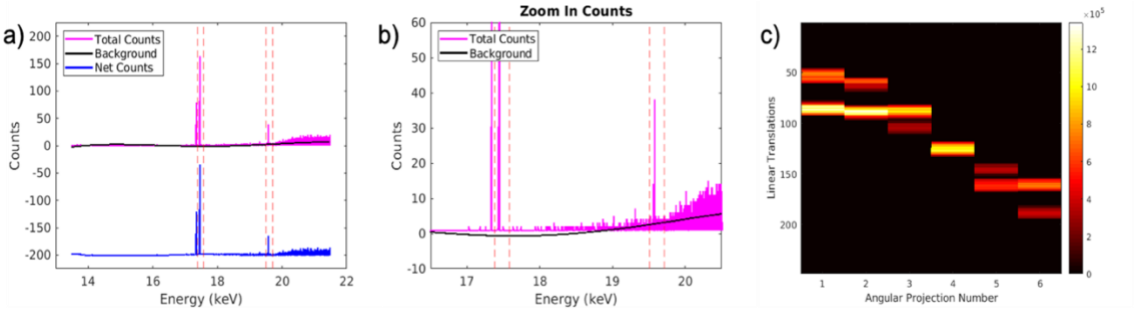

Figure 3.4: (a) A typical example of the removal of the scattered X-ray photons. (b) Zoomed-in image to show the removal of the scattered X-ray photons in the K-shell energy range of the MoNP nanoparticles. (c) Corrected sinogram summed over all 20 detectors. The detector energy resolution is depicted by the width of the red dashed lines (200 eV).

3.2.2. System Matrix and Reconstruction Algorithms

To reconstruct the image, an iterative reconstruction approach was taken in which a system of equations Ax = b must be solved, where A is the system matrix, x is the XFCT image, and b is the measurement. To generate the system matrix, the physical process and the imaging geometric parameters were considered. In XFCT imaging, the X-ray beam scans the object along a straight line, and the X-ray beam intensity distribution along the beam line follows the Beer–Lambert law. Upon X-ray beam excitation, target nanoparticles emit isotropic fluorescent X-ray lines. The intensity distribution of fluorescent X-ray lines that span the detector surface similarly follow the Beer–Lambert law. The system matrix is composed of these excitation and sensitivity matrices (F and P, respectively) as follows:

$$F_{j,m} = \exp\left(\sum -\mu_e(\mathbf{r}) \times L(\mathbf{r})\right) \tag{3.1}$$

$$P_{i,m} = \sum_{1}^{d_n} \exp\left(\sum -\mu_f(\mathbf{r}) \times L(\mathbf{r})\right) \tag{3.2}$$

$$\mathbf{A}_{n_d \times I \times J,m} = \begin{bmatrix} \begin{bmatrix} P_{1,m} \\ \vdots \\ P_{n_d,m} \end{bmatrix} \otimes F_{1,m} \\ \vdots \\ \begin{bmatrix} P_{1,m} \\ \vdots \\ P_{n_d,m} \end{bmatrix} \otimes F_{I \times J,m} \end{bmatrix} \tag{3.3}$$

$$0 \leq \mathbf{A}_{n_d \times I \times J,m} \leq 1$$

$\mu_e(\mathbf{r})$ is the linear attenuation coefficients of the imaging object and targets at the excitation energy. $\mu_{\mathbf{f}}(\mathbf{r})$ is the linear attenuation coefficients of the imaging object and targets at the fluorescent energy. $L(\mathbf{r})$ is the distance from the start of the X-ray beam or fluorescent emission to the position $\mathbf{r}$. d_n is the discretization number of the detector surface for which the fluorescent X-ray lines will be accounted for. $\otimes$ represents the element product between $P_{i,m}$ and $F_{j,m}$, where $i \in [1, n_d]$ is the detector number, $j \in [1, I \times J]$ is the excitation scan number, and m is the number of pixels used to discretize the object space. $I \times J$ is the product between angular projections number (I) and linear translation steps (J) of each angular projection, respectively. The forward model then becomes:

$$\mathbf{A}_{n_d \times I \times J,m}\, \mathbf{X}_{m,1} = \mathbf{B}_{n_d \times I \times J,1} \tag{3.4}$$

where $\mathbf{X_{m,1}}$ is the unknown image vector to reconstruct and $\mathbf{B_{n_d \times I \times J,1}}$ is the set of measurements.

The XFCT reconstruction can then be solved by minimizing the following optimization problem with the nonnegativity constraint:

$$\widehat{\mathbf{X}} = \arg\min_{\mathbf{x} \geq 0} \mathbf{Q}(\mathbf{x}) := \frac{1}{2} \|\mathbf{B} - \mathbf{A}\mathbf{X}\|_2^2 + \lambda \|\mathbf{X}\|_1^1 \tag{3.5}$$

where λ is the regularization parameter and $\|\mathbf{X}\|_1^1$ is the L^1 norm of the image vector $\mathbf{X}$. The fNUMOS algorithm is applied to minimize the L^1 regularized difference between the measurements modeled in GATE and the system matrix estimates. The details of the fNUMOS algorithm are explained in detail in [96-98, 106]. The L^1 regularization term is employed since it is well known for sparsity enhancement [95, 98]. The system matrix and reconstruction algorithms for were executed with MATLAB on a 20 multithreaded CPU workstation with 128 GB RAM.

The FBP algorithm employed the Hann filter and used the sinogram data as the input. The ML-EM based XFCT image reconstruction was performed with the system matrix as described in Equation 3.3, in which the anatomical guidance was included (the F vectors). The general form of the ML-EM algorithm was used, in which no regularization scheme

was applied. Both FBP and ML-EM algorithms were performed using the Michigan image reconstruction toolbox (MIRT) in MATLAB [112]. In this work, 15 iterations were performed by the ML-EM algorithm. A greater number of iterations in the ML-EM algorithm gave no significant benefit in the image quality metrics presented in Section 3.2.6.

3.2.3. High Spatial Resolution Imaging

To explore the high spatial resolution imaging capabilities of the imaging setup, small target sizes were used in the phantom. In the first case, the targets were set to have a diameter of 0.50 mm with target edge-to-edge distance equal to 0.50 mm. In the second case, the targets were set to have a diameter of 0.25 mm with target edge-to-edge distance equal to 0.25 mm. For high spatial resolution target reconstruction, the image space was discretized into 600 × 600 pixels, with a pixel size of 0.05 mm. To measure the image quality of the reconstruction with the small targets, square regions of interest (ROIs) with sizes of 2 × 2 and 4 × 4 pixel regions were used for 0.25 mm and 0.50 mm diameter targets, respectively.

3.2.4. Reconstruction Algorithm Performance with Different Angular Projection Number

To explore the robustness of the algorithm to the number of angular projections of measurements, the angular projection number varied from 3 to 10. The detector number also varied from 20 detectors to 2 detectors. The 2-detector configuration was determined based on the configuration that gave the best image quality. The target size was set to be 0.50 mm in diameter.

3.2.5. Reconstruction Algorithm Comparison

To explore the quality of the fNUMOS image reconstruction, the fNUMOS image reconstruction was compared to the ML-EM and FBP image reconstruction, which were based on the 20-detector configuration and six angular projections. For the FBP algorithm, the Hann filter was implemented in the FBP algorithm.

3.2.6. Image Quality Evaluation Criteria

Four criteria were used to evaluate the quality of the reconstructed images: target contrast ratio, Dice similarity coefficient, mean squared error (MSE), and contrast noise ratio (CNR).

A target contrast ratio was calculated to determine the proportionality of the contrast signals between the targets by taking the ratio of the contrast of the 10 mg/mL concentration target (T2) to the 5 mg/mL concentration target (T1). For this simulation, the closer the target contrast ratio is to two, the better. To measure the contrast signal from each target, the mean of a 5 × 5 pixel region of interest was taken from the reconstructed target center.

The Dice similarity coefficient (DICE) was used to measure the accuracy of the reconstructed target localization by comparing the reconstructed and true target positioning [72, 106].

$$\mathrm{DICE} = \frac{2 \times |\mathrm{ROI_r} \cap \mathrm{ROI_t}|}{|\mathrm{ROI_r}| + |\mathrm{ROI_t}|} \times 100\% \tag{3.9}$$

where $\mathrm{ROI_r}$ is the reconstructed target region of interest (ROI), defined as the pixels with intensities greater than 10% of the maximum pixel intensity. For smaller targets, the $\mathrm{ROI_r}$ is defined as the pixels with intensities greater than 20% of the maximum pixel intensity. $\mathrm{ROI_t}$ is the true target region of interest. Generally, the closer DICE is to 100%, the better.

The MSE was used to measure the difference between the normalized reconstruction and normalized ground truth [106].

$$\mathrm{MSE} = \frac{1}{\mathrm{N}} \sum_{\mathrm{i}=1}^{\mathrm{N}} (\mathrm{x_i} - \mathrm{x_{0i}})^2 \tag{3.10}$$

where x and x_0 are the normalized reconstructed and true target signal, respectively. N is the number of image pixels. The smaller the MSE, the better.

The CNR measures the level of distinction between the reconstructed targets and the background [106].

$$\mathbf{CNR} = \frac{\bar{\mathbf{x}}_{\mathbf{ROI}} - \bar{\mathbf{x}}_{\mathbf{ROB}}}{\sqrt{\boldsymbol{\omega}_{\mathbf{ROI}}\boldsymbol{\sigma}^{\mathbf{2}}_{\mathbf{ROI}} + (\mathbf{1} - \boldsymbol{\omega}_{\mathbf{ROI}})\boldsymbol{\sigma}^{\mathbf{2}}_{\mathbf{ROB}}}} \tag{3.11}$$

where $\bar{x}_{ROI}$ and $\bar{x}_{ROB}$ are the mean signal from the target ROI and the mean signal from the background ROI. The target ROI size was a 5 × 5 pixel region at the center of the true target. The background ROI was the region of pixels outside of the target ROI. $\omega_{ROI} = |ROI|/(|ROI| + |ROB|)$ and $|\cdot|$ is the number of elements. σ^2_{ROI} and σ^2_{ROB} are the variance of the region of interest of the targets and the variance of the region of the interest of the background, respectively. The larger the CNR, the better. In the results section, CNR_5 and CNR_{10} correspond to the CNR of the 5 mg/mL and 10 mg/mL target, respectively. According to the Rose criterion, CNR values greater than 4 are considered distinguishable from the background [40].

3.3 Results

To balance precision, computer memory, and computer storage, the data was processed and displayed to 1/1000 precision.

3.3.1. Effects of Detector Number and Detector Placement

To explore how the number of detectors and their placement along the ring configuration influence the quality of the reconstructed images, the number of detectors used for reconstruction was varied. The results of reconstructed images for four different detector numbers are seen in Figure 3.5. Zoomed-in target regions are provided, where the

green circles represent the true target size and locations. From the dashed blue lines in the zoomed-in images, line profiles are plotted with the intensity values normalized with respect to the max value along the dashed blue line. All four cases were able to separate and localize the target signals within the true target region without noise artifacts outside of the true target region. All four cases were able to reconstruct good target signals, except the case of the two-detector configuration.

The image quality metrics for the reconstruction with 2, 3, 4, and 20 detectors at different positions are listed in Table 3.1. All detector positions except for the two-detector configuration using the D0 and D4 detectors achieved a DICE coefficient of 88.737%. The two-detector configuration also showed the worst MSE. All targets were evaluated as distinguishable from the background based on the Rose criterion except for the 5 mg/mL target from the two-detector configuration. When the two-detector configuration was changed to the D9 and D14 detectors, the DICE improved from 71.805% to 88.737%. The target contrast ratio also improved from 6.910 to 2.415 when using the D9 and D14 detector configuration. For the three-detector configuration, the detectors D3, D12, and D17 provided a more accurate target contrast ratio than the D0, D9, and D14 detectors. For the four-detector configuration, the D3, D8, D13, and D18 detectors provided a more accurate target contrast ratio than the D0, D5, D10, and D15 detectors. The improvements in the image quality metrics between varying detector positions highlights the importance of detector position in XFCT imaging. The results indicate that two detectors are enough to reconstruct the targets with a DICE of up to 88.737%; however, the accuracy of the reconstruction is strongly dependent on the detector position and the number of angular projections, as seen in Table 3.1. It is observed that placing detectors at approximately 180° and 90° from the incident beam trajectory is best for the two-detector case

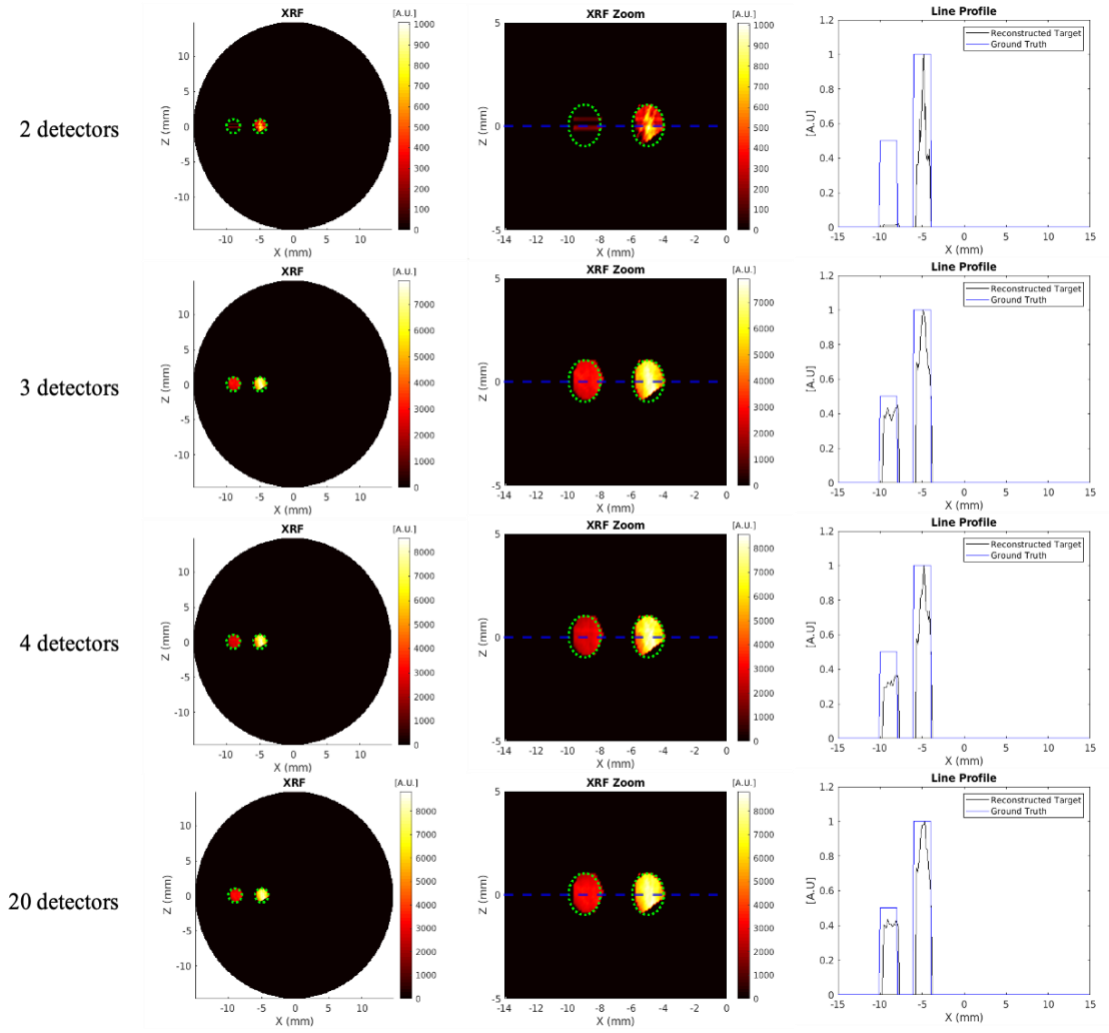

Figure 3.5: fNUMOS image reconstruction using different detector numbers. The full image (left), zoomed-in target regions (middle), and line profiles (right) are shown. The green dotted line in the zoomed-in target region indicates the exact target size and position; the blue dotted line indicates the line profile location.

Table 3.1: Image quality metrics for the GATE simulations with varying ring detector element number and position. * = the image quality metrics of the images in Figure 3.5.

Detector Number	**Target Contrast Ratio (Ground Truth = 2)**	**DICE (%) (Ground Truth = 100%)**	**MSE**	**CNR_5, CNR_{10}**
2 (D0, D4) *	6.910	71.805	2.229×10^{-3}	1.649, 11.396
2 (D9, D14)	2.415	88.737	1.105×10^{-3}	38.267, 92.413
3 (D0, D9, D14) *	2.430	88.737	1.113×10^{-3}	37.418, 90.907
3 (D3, D12, D17)	2.025	88.737	1.078×10^{-3}	18.196, 36.840
4 (D0, D5, D10, D15) *	2.887	88.737	1.116×10^{-3}	24.616, 71.068

4 (D3, D8, D13, D18)	1.774	88.737	1.030×10^{-3}	24.567, 43.577
20 (D0 to D19) *	2.389	88.737	1.061×10^{-3}	43.516, 103.936

3.3.2. Reconstruction Algorithm Comparison

Figure 3.6 shows the reconstructed images and target line profiles of the fNUMOS, ML-EM, and FBP algorithms. In general, the fNUMOS algorithm was superior in terms of achieving a uniform target signal reconstruction with no background noise and target signal that were proportional to their respective concentrations of 5 mg/mL and 10 mg/mL. Neither the ML-EM nor FBP algorithms were able to reconstruct the target signals with intensities proportional to the target concentrations.

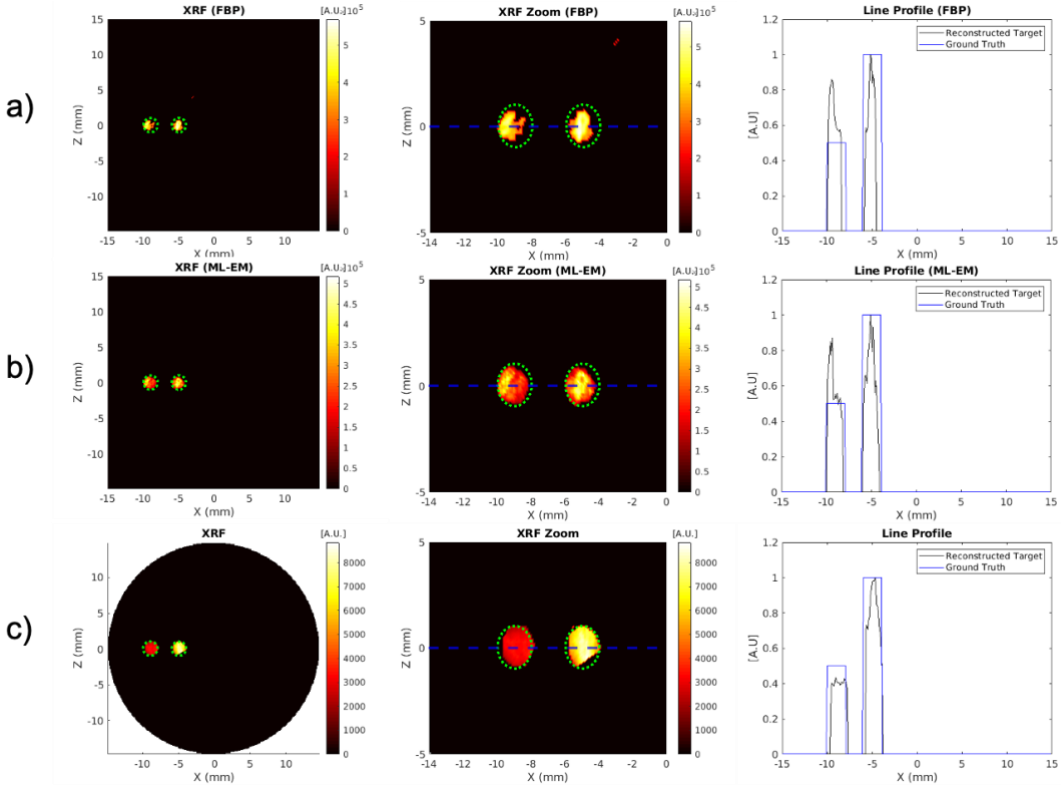

Figure 3.6: (a) Image reconstruction results using FBP. (b) Image reconstruction results using ML-EM. (c) Image reconstruction results using fNUMOS. All reconstruction algorithms utilized all 20 detectors from the ring detector configuration.

Table 3.2 shows the image quality metrics of reconstructed images from the fNUMOS, ML-EM, and FBP algorithms. From the Rose criterion, only the 5 mg/mL from the FBP was determined to be indistinguishable from the background. The ML-EM algorithm gave the best DICE. The DICE coefficient from the FBP reconstruction was inferior to ML-EM and fNUMOS. The FBP algorithm also showed the worst MSE from the algorithms. The combination of the accuracy of the target contrast ratio, DICE coefficient, MSE, and CNR

values shows that the fNUMOS outperformed the other algorithms. The target contrast ratio, MSE, and CNR values were best with the fNUMOS algorithm.

It is also worth noting the time taken for the reconstruction algorithms to reach their solutions. The fNUMOS algorithm took <0.05 s to successfully reconstruct the 300 × 300 pixel XFCT image using the data collected by all 20 detectors in the ring configuration. The ML-EM algorithm took >10 min and the FBP algorithm took <0.5 s to reconstruct the same image, with overall image quality below that of the fNUMOS reconstruction.

Table 3.2: Image quality metrics for the GATE simulations with FBP, ML-EM, and fNUMOS reconstruction.

Reconstruction Method	**Reconstruction Time (s)**	**Target Contrast Ratio (Ground Truth = 2)**	**DICE (%) (Ground Truth = 100%)**	**MSE**	**CNR_5, CNR_{10}**
FBP	0.479048	2.410	64.918	2.422×10^{-3}	2.447, 5.897
ML-EM	661.2517	1.5713	89.170	1.645×10^{-3}	12.879, 20.237
fNUMOS	0.015264	2.389	88.737	1.061×10^{-3}	43.516, 103.936

3.3.3 High Spatial Resolution Imaging

Figure 3.7 shows the reconstructed images, and the target line profiles for the small targets. Due to the size of the targets, slight background noise is noticeable in the reconstructed images; however, clear target separation is still achieved, as seen in the images and the line profiles.

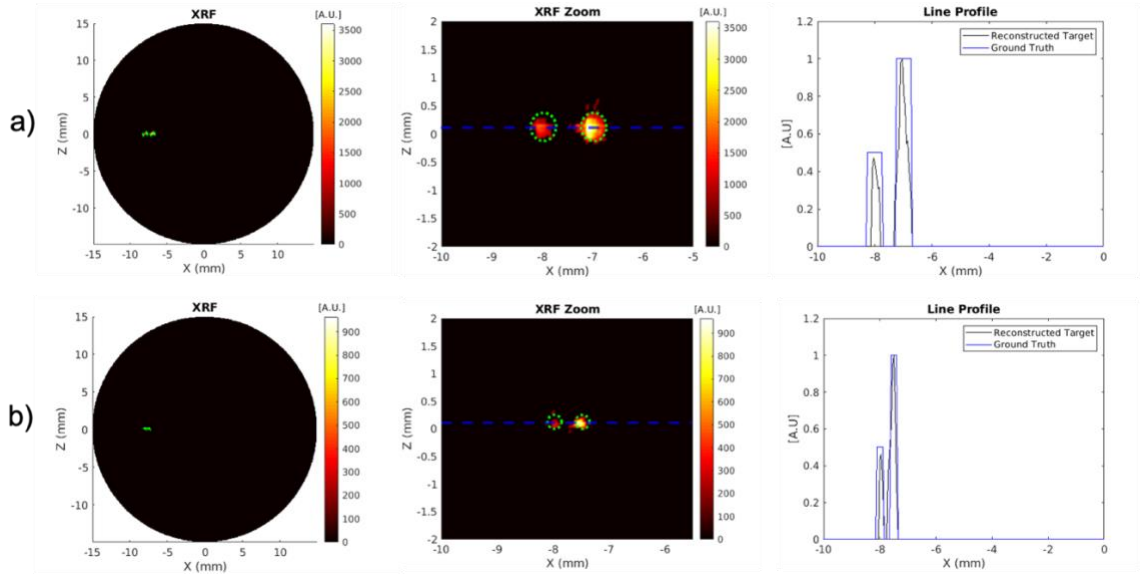

Figure 3.7: fNUMOS reconstruction of small targets. (a) Image reconstruction of the 0.50 mm diameter targets. (b) Image reconstruction of the 0.25 mm diameter targets. The reconstructions used all 20 detectors from the detector ring configuration.

Table 3.3 shows the image quality metrics for high spatial resolution imaging of the small targets. The detector number also varied from 20 detectors to two detectors. The two-detector configuration used detectors of D9 and D14, which was the detector configuration with the best image quality metrics from Table 3.1.

Table 3.3: High spatial resolution imaging metrics with varying target size and detector number.

Target Size (mm)	**Detector Number**	**Target Contrast Ratio (Ground Truth = 2)**	**DICE (%) (Ground Truth = 100%)**	**MSE**	**CNR_5, CNR_{10}**
0.25	20 (D0 to D19)	2.981	38.89	5.710×10^{-5}	4.650, 13.861
	2 (D9, D14)	4.071	37.68	5.796×10^{-5}	2.003, 8.153
0.50	20 (D0 to D19)	2.030	66.67	1.197×10^{-4}	7.445, 15.110
	2 (D9, D14)	1.662	67.13	1.283×10^{-4}	5.474, 9.098

For the 0.25 mm target reconstruction, the target contrast ratios are 2.981 and 4.071 for the 20-detector and two-detector configuration, respectively. The DICE coefficients are 38.89% and 37.68% for the 20-detector and two-detector configuration, respectively. The MSE of the 20-detector configuration and the two-detector configuration are similar. For the 20-detector configuration, both targets are distinguishable from the background according to the Rose criterion. For the two-detector configuration, the 5 mg/mL target is indistinguishable from the background.

For the 0.50 mm target reconstruction, the target contrast ratios are 2.030 and 1.662 for the 20-detector and two-detector configuration, respectively. The DICE coefficient of the 0.50 mm target is slightly better with the two-detector configuration than the 20-detector configuration. MSE and CNR values are the best for the 0.50 mm targets with the 20-detector configuration. When considering the combination of the image quality metrics, the most accurate reconstruction for high spatial resolution is obtained when using the 20-detector configuration and 0.50 mm diameter targets. The least accurate reconstruction for high spatial resolution is obtained with the 0.25 mm targets when using the D9 and D14 detector configuration.

3.3.4 Reconstruction Algorithm Performance with Different Angular Projection Number

Table 3.4 shows the image quality metrics with varying angular projection numbers and detector numbers. The two-detector configuration used detectors of D9 and D14, which is the detector configuration with the best image quality metrics from Table 3.1. The most accurate reconstruction was achieved with 10 angular projections with detectors D9 and D14 when considering the target contrast ratio, DICE, MSE, and CNR values. The MSE and CNR values are best with 10 angular projections and the two-detector configuration. The least accurate reconstruction was achieved with three angular projections and detectors D9 and D14, which showed the worst MSE and target contrast ratio, lowest DICE, and lowest CNR values. The 5 mg/mL target reconstruction with three angular projections and the two-detector configuration was determined to be indistinguishable from the background. The best DICE was achieved with six angular projections with the 20-detector configuration. From Table 3.4, we see that the reconstructed XFCT image quality is good with 20 detectors and is not very good with two detectors when the angular projection

number is three, which is reasonable. The reconstructed XFCT images are good when the angular projection number is six or 10 for both two detectors and 20 detectors. Note that while the Rose criterion is preserved, the improvement of DICE and target contrast ratio is not significant for the 20-detector case compared to the two-detector case if the angular projection number is six or 10. This means that a large number of detectors is not needed if six angular projections are performed.

Table 3.4: Image quality metrics with varying angular projection number and detector number.

Number of Projections	Detector Number	Target Contrast Ratio (Ground Truth = 2)	DICE (%) (Ground Truth = 100%)	MSE	CNR_5, CNR_{10}
3	20 (D0 to D19)	2.201	55.07	1.874×10^{-4}	15.208, 33.476
	2 (D9, D14)	3.220	49.18	1.993×10^{-4}	2.066, 6.654
6	20 (D0 to D19)	1.825	65.67	1.528×10^{-4}	4.923, 8.983
	2 (D9, D14)	1.750	53.97	1.763×10^{-4}	4.859, 8.506
10	20 (D0 to D19)	2.186	57.14	1.472×10^{-4}	32.853, 71.801
	2 (D9, D14)	2.161	59.62	1.377×10^{-4}	61.394, 132.651

3.4 Preliminary XFCT Experiment with a superfine pencil beam

3.4.1 Preliminary XFCT system with a superfine pencil beam

An XOS source (X-Beam Powerflux [Mo anode], XOS) is used to generate X-ray photons with 100 μm beam size at the focal distance from the XOS polycapillary lens opening. The XOS source was operated at 50 kVp and 1 mA. The phantoms were mounted onto a motorized rotary stage (RT-3, Newmark Systems Inc.) that is fixed on top of a motorized vertical stage (VS-50, Newmark Systems Inc.) and a motorized linear stage (NLE-100, Newmark Systems Inc.) for rotating and translating the phantom while the XOS source remains stationary. A lab-made C/C++ code is used to control the motorized stages. The imaging system except the computer is contained in a light tight and X-ray shielding lead cabinet. A single CdTe detector (X-123CdTe, Amptek) was used to capture the spectral measurements. The detector is positioned 90° from the incident X-ray beam to minimize the Compton scattering noise in the measurement. The CdTe detector was allowed to translate with the phantom. The CdTe detector has an energy resolution of 530 eV at 14.4 keV. Lab-made C/C++ code is used to automate the acquisition of the spectral measurements.

The system matrix for each XFCT imaging setup was generated using the same procedure as in Section 3.2.2. The image reconstruction was performed using the fNUMOS algorithm in MATLAB.

3.4.2 Experimental Setup of the single target agar phantom

The schematic and experimental setup of the first XFCT imaging is shown in Figure 3.8a and Figure 3.8b. A 12 mm diameter cylindrical agar phantom composed of 1% intralipid mixture was positioned at the focal distance (44.9 mm). A 1%wt Au nanoparticle target was positioned offset from the phantom center. Figure 3.8c shows an image of the phantom used in this setup. The target size diameter was 4 mm at the X-ray scan depth. Six

angular projections (0, 30, 60, 90, 120, 150) and 80 linear scan steps per projection were used to scan the phantom. The linear step size was 0.15 mm. The CdTe detector was positioned 2 cm from the phantom surface. Each linear step was acquired for 20 sec. Each angular projection took 27 min to complete. Due to the prolonged scan time, the scan was paused for 20 min every two angular projections to cool the X-ray source and rehydrate the agar phantom with water droplets. Therefore, the total scan time with pause breaks was 200 min. The L-shell energy counts of Au (9.71 keV and 11.44 keV) were collected for each measurement from the CdTe detector. The same fitting procedure as in Figure 3.4 was used to remove Compton noise from the XFCT sinogram.

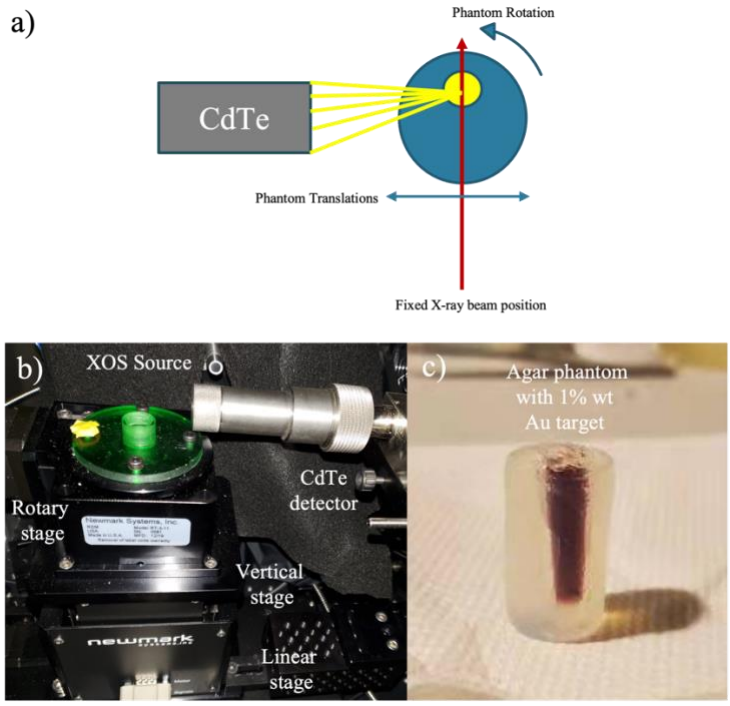

Figure 3.8: Setup of the XFCT system with a superfine X-ray beam to image the agar phantom. a) Schematic of the agar phantom XFCT experiment. b) Experimental XFCT setup showing the CdTe detector, XOS source, phantom holder, rotary stage, vertical stage, and linear stage. c) The imaging phantom with embedded 1%wt Au target.

3.4.3 Experimental Setup of the three-target air phantom

The schematic and experimental setup of the second XFCT imaging is shown in Figure 3.9a and Figure 3.9b. A 21 mm diameter cylindrical air phantom was positioned at the focal distance (44.9 mm). The air phantom was 3D printed with an inner diameter of 20 mm. Three glass tube targets with different Au concentrations (0.1%wt, 0.5%wt, 1.0%wt) were positioned offset from the phantom center. Figure 3.9c shows an image of the phantom used in this setup. The outer diameter of the targets was 6 mm and the inner target size diameter was 4 mm. Six angular projections (0, 30, 60, 90, 120, 150) and 100 linear scan steps per projection were used to scan the phantom. The linear step size was 0.20 mm. The CdTe detector was positioned 2 mm from the phantom surface. Each linear step was acquired for 90 sec. Each angular projection took 2.5 hrs to complete. Due to the prolonged

scan time, a cooling system was installed inside the cabinet to prevent the X-ray tube and CdTe detector from overheating. The total scan time was 15 hrs. Due to the attenuating effects of the printed cylinder and the glass tubes, only the 11.44 keV L-shell energies were collected from the detector measurements. The same fitting procedure as in Figure 3.4 was used to remove Compton noise from the XFCT sinogram.

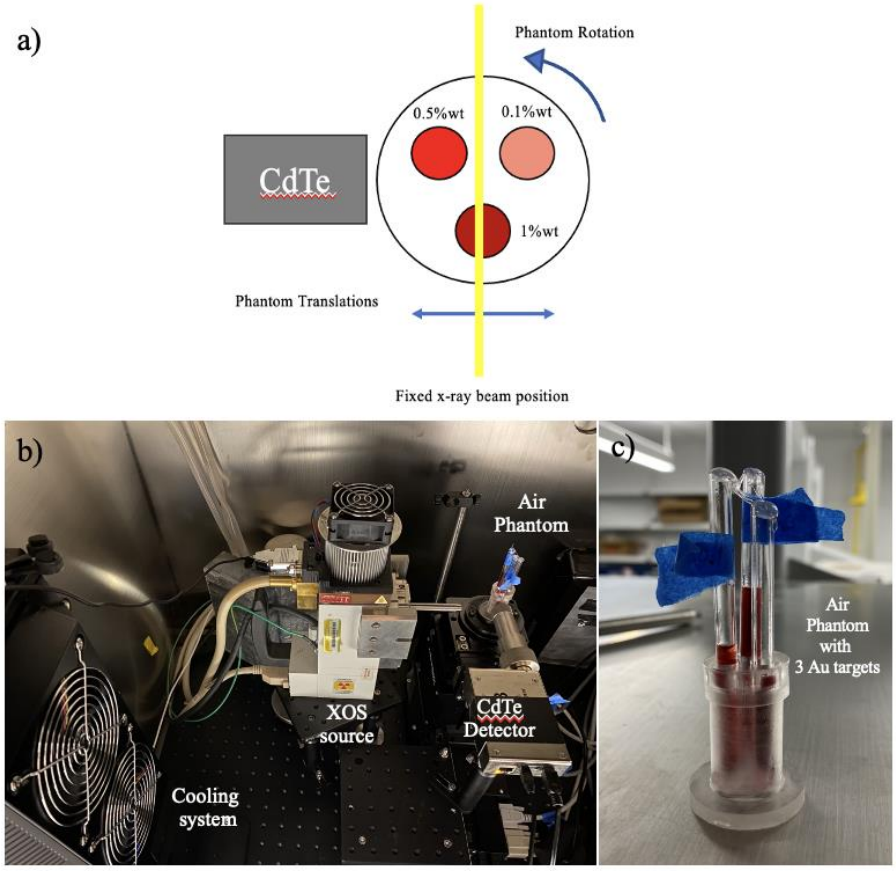

Figure 3.9: Setup of the XFCT system with a superfine X-ray beam to image the air phantom. a) Schematic of the air phantom XFCT experiment. b) Experimental XFCT setup showing the CdTe detector, XOS source, phantom, and cooling system. c) The imaging phantom with three targets of different Au concentrations.

3.4.4 Results of the agar phantom XFCT experiment

Figure 3.10a shows a sample of a step acquisition of the agar phantom in which the Compton scattered X-rays are removed through background interpolation. The net counts bound between the solid red curves were collected for the sinogram. The width of the solid red line corresponds to the energy resolution of the detector (530 eV at 14.4 keV). Figure 3.10b shows the sinogram of the agar phantom XFCT scan.

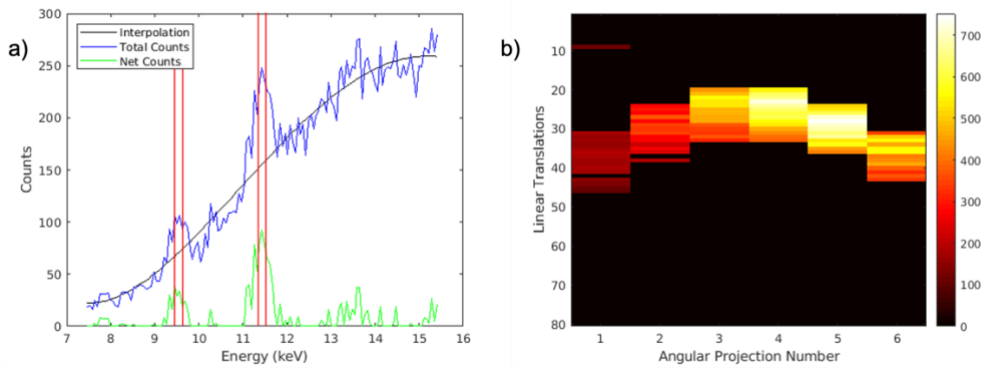

Figure 3.10: a) Sample of the removal of the Compton scatter X-rays from the acquired total counts from the agar phantom. b) Corrected sinogram of the CdTe detector. The detector energy resolution is depicted by the width of the red solid lines (530 eV at 14.4 keV).

Figure 3.11 shows the results of the agar phantom XFCT image reconstruction with the fNUMOS algorithm. The green dashed circle shows the ground truth positioning of the Au target in the agar phantom. The DICE coefficient of the image reconstruction was calculated to be 51.84% using Equation 3.11.

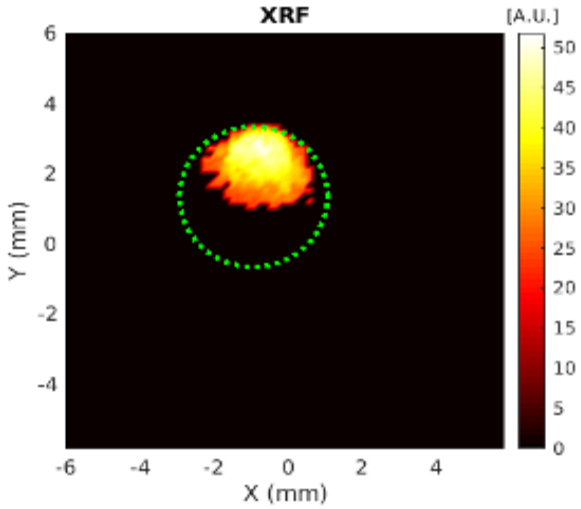

Figure 3.11: fNUMOS reconstruction of the Au nanoparticle distribution in the agar phantom. The green dashed circle shows the ground truth positioning of the Au target in the agar phantom.

3.4.5 Results of the air phantom XFCT experiment

Figure 3.12a shows a sample of a step acquisition of the air phantom in which the Compton scattered X-rays are removed through background interpolation. The net counts bound between the solid red curves were collected for the sinogram. The width of the solid red line corresponds to the energy resolution of the detector (530 eV at 14.4 keV). Figure 3.10b shows the sinogram of the air phantom XFCT scan.

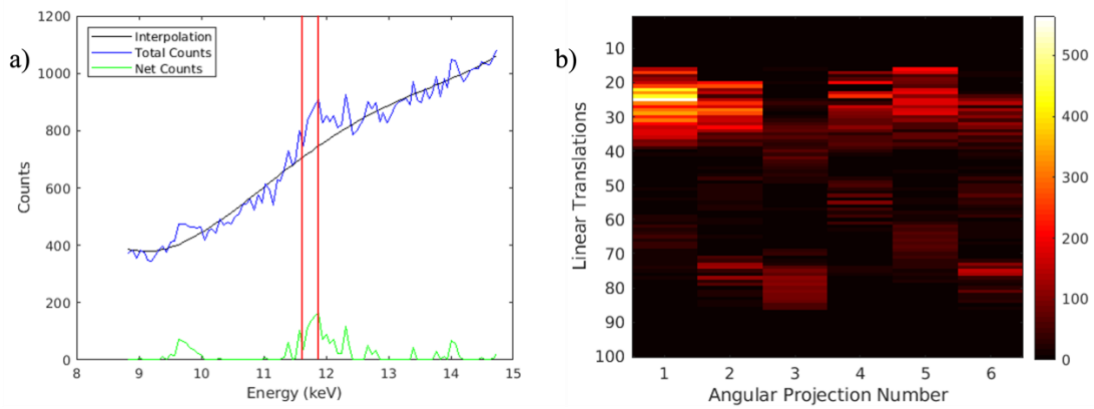

Figure 3.12: a) Sample of the removal of the Compton scatter X-rays from the acquired total counts from the air phantom. b) Corrected sinogram of the CdTe detector. The detector energy resolution is depicted by the width of the red solid lines (530 eV at 14.4 keV).

Figure 3.13 shows the results of the air phantom XFCT image reconstruction with the fNUMOS algorithm. The green dashed circle shows the ground truth positioning of the Au targets in the air phantom. Figure 3.13a shows the unsuccessful reconstruction of the Au targets in the air phantom due to the high noise level in the acquired signal. In this case, only a fraction of a single target was reconstructed with significant noise artifacts. Figure 3.13b shows a binary image of the reconstructed signal in which all pixel values greater than 1 are given the value 1 and regions with no signal are given a value 0. The XFCT binary image shows that all Au targets can be localized despite the high level of noise from Compton scattering.

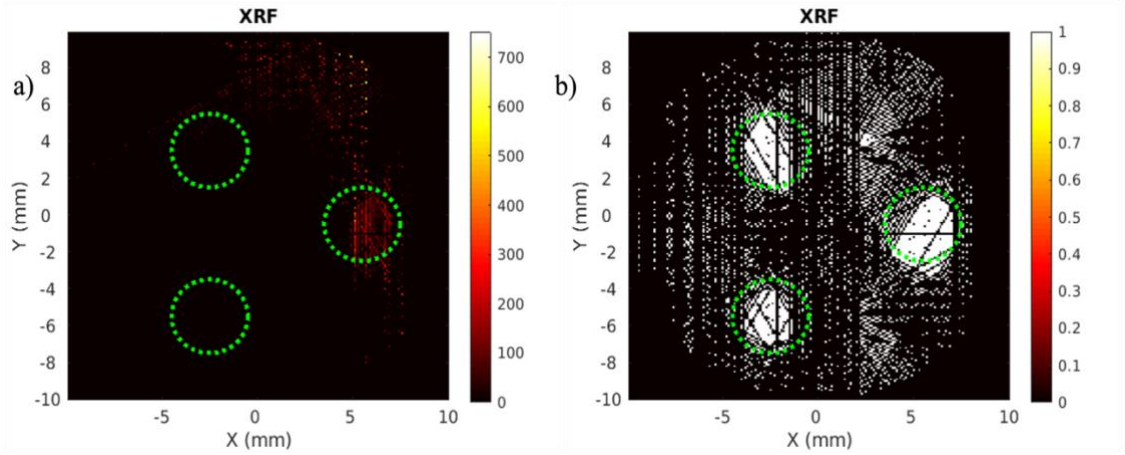

Figure 3.13: XFCT fNUMOS reconstruction results of the Au targets in the air phantom. a) Unsuccessful image reconstruction of the Au targets in the air phantom b) Binary image of the Au nanoparticle distribution in the air phantom. All pixel values greater than 1 are shown. The green dashed circle shows the ground truth positioning of the Au targets in the air phantom.

3.5 Discussion

In this chapter, a benchtop XFCT imaging system comprised of ring detector elements and a benchtop quasi-monochromatic source was modeled in GATE. The fNUMOS algorithm was applied to reconstruct the image successfully and efficiently. The fNUMOS algorithm was successful in localizing small targets as well. Due to the unique energy characteristics of the benchtop source, a relatively low X-ray photon number was enough to obtain a good XFCT signal even when a low number of detectors from the ring configuration were used. If a conventional polychromatic source were to be used instead, the number of X-rays would need to be increased to obtain sufficient fluorescent counts for a good image reconstruction since the bremsstrahlung energies would mainly contribute to dose.

The proposed imaging scheme and reconstruction algorithm was studied with different detector numbers and detector positions, and different angular projection numbers. Compton scattering effects prevent a good and clear XFCT signal from being detected. Detector placement is crucial to minimizing the detection of greater scattering counts. Typically, detectors are placed >90° to the incident beam trajectory to minimize scatter. In this work, it was shown that two detectors are enough to accurately reconstruct the targets; however, the accuracy of the reconstruction is strongly dependent on the placement of the detectors and the number of angular projections, as seen in Tables 3.1 and 3.4. Placing detectors at approximately 180° and 90° from the incident beam trajectory is best for the two-detector case. This recommendation is supported by other literature [54, 69, 104]. When considering the imaging protocol and dose concerns with pencil-beam XFCT imaging, six angular projections are sufficient to provide an accurate reconstruction of small targets. However, when utilizing the full ring configuration with 20 detectors, three angular projections are enough for an accurate reconstruction based on the image quality metrics.

Several artifacts can be observed in Figure 3.5. In the two-detector configuration, the artifacts resulted from bad detector placement, in which the reconstructed targets had a nonuniform signal intensity. From detector configurations 3, 4, and 20, the artifacts are the slight signal nonuniformity in the right target and the missed target signals in the bottom right of the right target. These artifacts were likely caused by the combination of the limited projection number and the scatter noises. It is well known that measurements at each projection takes a very long time to measure. It is a compromise between the measurement time (projection number) and the image quality [69].

From the image quality metrics in Table 3.3, the target contrast ratio retained proportionality of the reconstructed signals, whereas the CNR and DICE image quality metrics suffered. These results are due to the increased sparsity of the problem. With the 2 mm targets, the incident beam linearly projected at most 16 times on each target. For the 0.50 mm and 0.25 mm targets, the incident beam linearly projected at most four and two times on each target, respectively. The reduction of the beam incident on the targets resulted in significantly less fluorescent X-rays for an accurate reconstruction. Nonetheless, the fNUMOS algorithm was able to localize the signal from the small targets within the true target region.

The fNUMOS reconstruction algorithm performance was compared with the popular ML-EM and FBP algorithms. The image quality metrics show that the fNUMOS reconstruction algorithm is superior when considering the combination of the target contrast ratio, DICE coefficient measurements, CNR values, MSE, and reconstruction

time. The XFCT measurements only have six angular projections, which is why artifacts in the reconstructed XFCT images by FBP are observed. Unlike the FBP and ML-EM, the fNUMOS algorithm performs well with sparse targets with little computation time, as seen in this work and in XLCT studies [76, 95], because there is L^1 regularization in the fNUMOS algorithm.

In the preliminary experimental XFCT studies, a 100 μm X-ray beam was used to scan a couple of phantoms. First, a 12 mm phantom with a 4 mm 1%wt Au target was scanned. The total scan time after six angular projections (80 step/projection) was 200 min. A 51.84% DICE coefficient was obtained after fNUMOS image reconstruction. Next, a 20 mm phantom with three Au targets of differing concentrations was scanned. The total scan time after six angular projections (100 step/projection) was >16 hrs. The image reconstruction was unsuccessful as the noise signal outweighed the target signals. However, the image reconstruction was able to localize the targets as observed in Figure 3.13. Only one CdTe detector was used to collect the spectral measurements. The motivation for this work arose from Vernekohl et al in which they were able to scan a 3cm diameter object within 66 min. They were able to detect a Au concentration of 0.03%wt with a 2.6 mm X-ray pencil beam and two spectrometers [53]. Two significant comparisons can be attributed to their study success. (1) A greater X-ray beam width was used which enable a greater cross section for X-ray absorption in the Au target. (2) Two spectrometers were used therefore less acquisition time and increased sensitivity is achieved.

3.6 Conclusion

In summary, a benchtop pencil-beam XFCT imaging system with a ring detector and a unique quasi-monochromatic benchtop source was proposed. GATE simulations were performed to validate the forward modeling and the fNUNMOS-based XFCT reconstruction algorithm. Our simulation results indicate that a quasi-monochromatic source from Sigray and a 20-detector ring could be used to improve the performance of the proposed XFCT imaging system. In the future, we plan to collaborate with the Sigray company to design and build a benchtop XFCT system with good spatial resolution and practical scanning times for small animal XFCT imaging. In the experimental work, current resource limitations like a low intensity X-ray source and the use of a single detector hindered the experiment success, however, the future XFCT experiment will employ multiple spectrometers to improve the sensitivity of the image reconstruction and allow for reduction in acquisition.

Acknowledgements: I would like to thank Yile Fang and Dr. Michael Lun. Yile Fang helped build the XFCT system matrix for this work, and Dr. Michael Lun performed the preliminary XFCT experiment. I designed and executed the XFCT simulations in GATE. I also performed the data analysis and image reconstructions in this work.

CHAPTER 4

RADIATION DOSE ESTIMATION IN PENCIL BEAM XLCT IMAGING

4.1 Introduction

X-ray luminescence computed tomography (XLCT) has emerged as a promising molecular imaging tool because XLCT combines the high measurement sensitivity of optical imaging and high spatial resolution of X-ray imaging. XLCT uses X-ray beams to excite nanophosphors embedded in deep tissues of the imaging object. The nanophosphors emit optical photons to be measured for optical imaging. The width and position of the pencil beam can be used as structural guidance to reconstruct the XLCT image therefore creating a molecular image with high spatial resolution [25, 76, 95]. Pencil beam XLCT imaging provides superior spatial resolution than other XLCT geometries like sheet beam and cone beam geometries because the fine pencil beam can provide anatomical guidance in the XLCT image reconstruction to resolve fine targets. The structural guidance information is lost when using the sheet beam and cone beam geometries for XLCT imaging which limit the sensitivity and spatial resolution [31, 35, 113-115]. However, a pencil beam scan suffers from long scan times. Thus, concerns with dose discourage laboratory use of pencil beam X-ray sources. To minimize the dose, benchtop X-ray sources are filtered to remove the lower energy X-ray photons, but the added filtration increases the scan times. Instruments used to measure the dose in pencil beam X-ray imaging is difficult. With superfine pencil beams, the instruments often suffer from partial volume response limitations, and/or dose rate dependence which hinder the accuracy of the dose measurements. It is better to numerically simulate the pencil beam XLCT imaging protocol to accurately calculate the absorbed dose.

In this work, the dose deposited into a small object (5 mm in diameter) using a pencil X-ray beam geometry was simulated in GATE (Geant4 Application for Tomographic Emission) [107-109]. The small object was composed of water, bone, and blood to simulate the bone marrow structures of a mouse leg. Three different X-ray sources were simulated, and the dose and dose rate delivered from one angular projection scan were shown and compared. The dose measurements were repeated with different X-ray output rates to generate the linear relationship of the absorbed dose in each structure to the X-ray source output photon number. Among the three different X-ray sources, a benchtop quasi-monochromatic X-ray source from Sigray Inc was modeled. Next, a small (~30 mm in diameter) mouse trunk model composed of muscle, bone, and a breast malignant tumor was imported into GATE to estimate the total dose delivered in a six angular projection scan. The three different X-ray sources were simulated, and the dose and dose rate delivered to the different mouse structures are shown and compared.

The chapter is organized as follows. In section 4.2, the methods of the GATE simulations, setup, and source spectra are presented. In section 4.3, the results showing the relationships between X-rays output and dose with different spectra are presented. This chapter concludes with discussions of the results and future works.

4.2 Methods

4.2.1 GATE programming

The GATE simulations in this work were parallelized and executed with a custom bash script on a 20 CPU workstation. The Penelope physics package (empenelope) from GEANT4 was used to model the physical processes. The Dose Actor feature from GATE was used to store the dose delivered to the volume inside a 3D matrix [109].

4.2.2 Bone marrow phantom setup

A 5 mm diameter cylindrical water phantom with a 2 mm diameter cylindrical bone structure located at the phantom center was simulated in GATE. A 1 mm diameter cylindrical blood structure was centered in the bone structure to simulate the bone marrow. The imaging object was placed at the center of the reference axis. The source beam width at the central coronal slice (x-axis) was 100 μm. A linear scan step size of 100 μm was used to acquire a single angular projection. The schematic of the bone marrow phantom GATE simulation setup along with a snapshot of the GATE simulation is shown in Figure 4.2. The black box in the schematic is a representation of the dose actor tool from GATE which is seen as the white framed box around the simulated object.

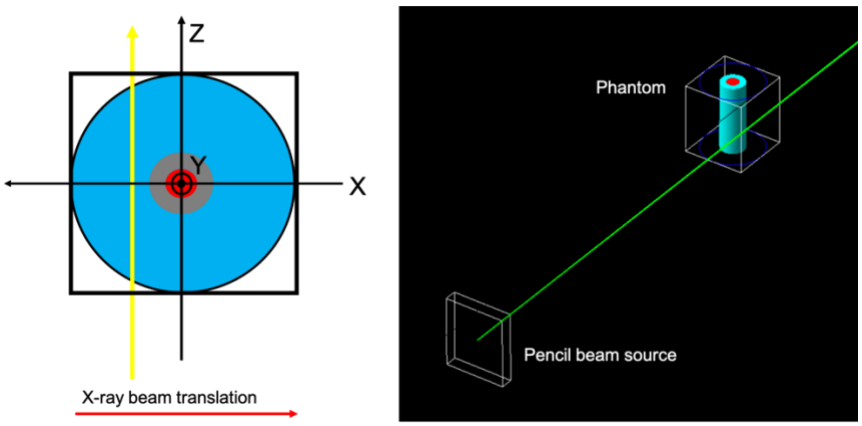

Figure 4.1: Schematic (left) and simulation snapshot (right) of the pencil beam dose GATE simulations for the bone marrow study.

The dose was stored in a 5 mm^3 cube with voxel size of 0.1 mm^3. 5×10^5, 7.5×10^5, 10^6, 1.25×10^6 and 1.5×10^6 X-ray photons were used for each linear scan step to establish a linear relationship between X-ray photon number and dose. From the linear relationship, the dose delivered by the X-ray sources at any output rate can be estimated by linear interpolation.

4.2.3 Mouse model setup

A 32.6 mm diameter mouse trunk model was simulated in GATE. To generate the mouse model, a mouse CT image from a previous microCT scan was processed in MATLAB to show only the muscle and the spine of the mouse. The mouse trunk CT image is shown in Figure 4.3a. A 6.2 mm diameter tumor composed of 8%wt calcium oxalate was simulated and positioned close to the spine of the mouse model as shown in Figure 4.3b. Calcium oxalate has been found to exist at higher concentrations in malignant breast tissues [116, 117]. Breast cancers are commonly used in mouse tumor models [118, 119]. A schematic of the GATE simulation with the mouse model is shown in Figure 4.3b. The mouse model was discretized into 186×176×1 voxels. The voxel size was set to 0.2 mm^3. The mouse model was placed at the center of the reference axis. The source beam width at the central coronal slice (x-axis) was 100 μm. A linear scan step size of 100 μm with 380 linear steps per angular projection and six angular projections with an angular step size of 30° was used to scan the mouse (0°, 30°, 60°, 90°, 120°, 150°).

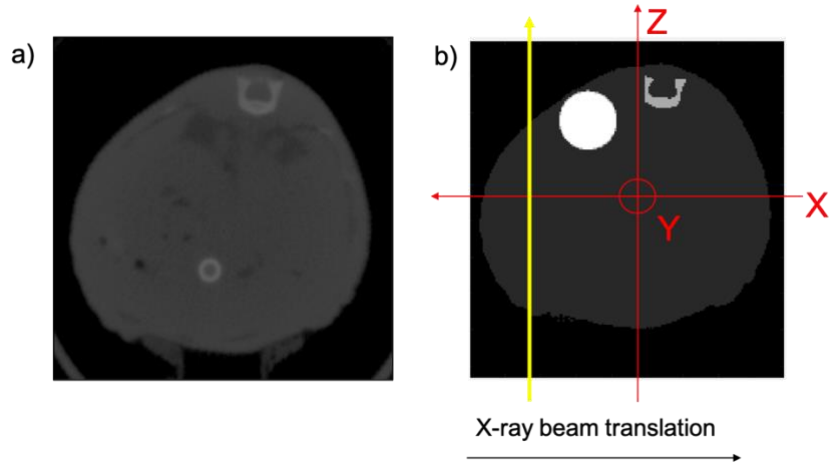

Figure 4.2: a) A transverse slice of a mouse CT image; b) Schematic of the pencil beam GATE simulation with the mouse model. The difference in the image values in the mouse model is due to the different labeling values used for the GATE simulation.

The dose deposited in the mouse model was stored in a 186×176×1 cube with voxel size of 0.2 mm^3. 5×10^5, 6.25×10^5, 7.5×10^5, 8.75×10^5, and 10^6 X-ray photons were used for each linear scan step to generate the linear relationship between the X-ray photon number and dose. From the linear relationship, the dose delivered by the X-ray sources to each mouse structure at any output rate can be estimated by linear interpolation.

4.2.4 X-ray source spectra modeling in GATE

For the X-ray source from Sigray Inc., we have estimated and plotted its energy spectrum in Figure 4.4. To simulate the XOS X-ray source (X-Beam Powerflux [Mo anode], XOS) in our lab, a 50 kVp spectrum of the X-ray source with polycapillary lens was acquired and normalized. The polycapillary lens only focused X-ray photons with energies less than 30 keV. The lab X-ray tube focuses X-rays to an approximate focal spot

size of 100 µm at its focal distance. The histogram user spectrum tool from GATE was used to import the XOS source histogram. The energy of the emitted photon within each bin of the histogram was distributed uniformly. The spectrum is plotted in Figure 4.5a below. Due to the utilization of a polycapillary lens, the spectrum was truncated after 30 keV. To minimize the dose contribution from low energy X-ray photons, a 2 mm Al filter was positioned in front of the source. The spectrum for the filtered XOS lab source was calculated and plotted in Figure 4.5b.

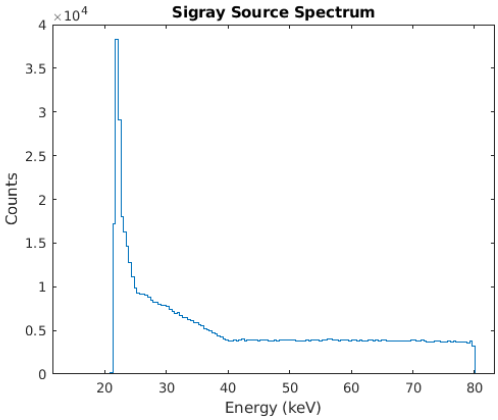

Figure 4.3: The X-ray energy spectrum of the X-ray source from Sigray, Inc.

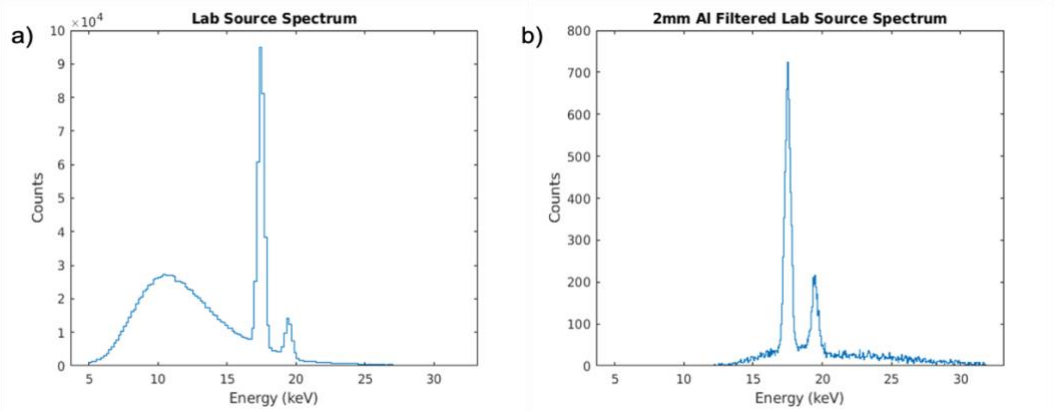

Figure 4.4: The X-ray energy spectrum of the XOS source without (a) and with (b) a 2 mm thick aluminum filter after the polycapillary lens.

4.2.5 Dose estimations

The dose stored in each voxel in GATE was calculated as the energy deposited per mass of the voxel. For the water phantom, the dose for bone marrow, bone, and object background were calculated as the mean dose from each region. This was done by using masks to identify only those pixels belonging to the bone marrow, bone, or object background and then the values in each region were averaged. For the mouse trunk model, the total dose for the bone, muscle, and tumor were calculated as the mean dose for each structure. This was done by using masks to identify only those pixels belonging to the bone, muscle, or tumor. Then the values in each structure were averaged to obtain the mean dose

(total dose). All dose calculations were done in MATLAB after the GATE simulations had been completed.

4.3 Results

4.3.1 Results of the bone marrow dose map in one projection XLCT imaging

Figure 4.6 shows the central line profile and dose maps for the cases of the filtered XOS source, unfiltered XOS source, and Sigray source. All the sources had an X-ray photon number of 10^6 per linear scan step. All three cases had 50 linear steps with the same pencil beam size and step size of 100 micrometers. From Figure 4.6, it is shown that the bone structure absorbed more dose than the surrounding background and bone marrow structures due to the bone's greater effective atomic number (Z). In Figure 4.6a, the addition of the Al filter results in the removal of the high entrance dose as seen in Figure 4.6b. Without the Al filter, the lower energy photons result in increased air ionizations and superficial dose which result in the high entrance dose as seen in the central slice line profile and dose map of Figure 4.6b. However, by adding a filter, the mean energy of the X-ray source is increased which results in beam hardening and the X-rays become more penetrating to deliver greater dose in deeper structures. This can be seen by the increased dose in the right bone peak and the exit dose of the central slice line profiles in Figure 4.6a compared to those in Figure 4.6b. The shadowing effects are also less severe as shown in Figure 4.6a due to the beam hardening effects. Figure 4.6c shows more uniformity in the dose distribution due to a greater average energy by the Sigray source and less dose in the bone morrow region compared with the XOS source cases.

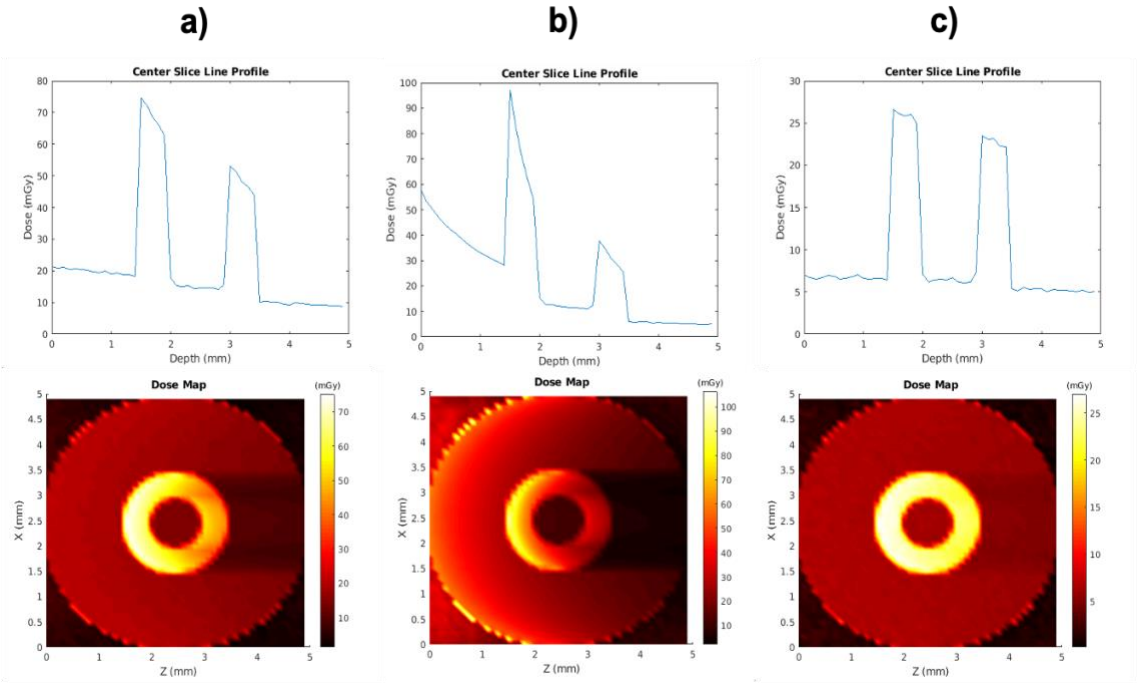

Figure 4.5: Center slice line profile and dose maps of (a) Filtered XOS source, (b) Unfiltered XOS source, (c) Sigray source for 10^6 x-ray photons per linear scan step for all 50 steps.

4.3.2 Bone marrow dose estimation based on X-ray photon number for one projection XLCT imaging

Figure 4.7 shows the regression line plots with trendline equations relating the X-ray number per linear scan step (photons/step) to the absorbed average dose (Avg Dose) in milliGray (mGy) units for cases of the filtered XOS source, the unfiltered XOS source, and the Sigray source and for the different components of the phantom. All regression plots showed a high positive linearity with all R^2 values being greater than 0.99. For all regression plots, the bone structure shows greater values of average absorbed dose than the bone marrow and background structures. All the trendlines equations for the bone structure show a greater slope therefore bone will absorb dose at a greater rate than the other structures. For Figure 4.7a, the regression lines of bone marrow and background are identical. Figure 4.7a shows a slight increase in the dose rate of the bone structure due to the beam hardening effects from the Al filter. In Figure 4.7b, the background regression curve is greater than the bone marrow regression curve due to the bremsstrahlung energies depositing significant dose to the background. Figure 4.7c shows the lowest absorbed dose rate for the bone structure. Figure 4.7c also shows a decrease of at least a half order of magnitude in the absorbed dose rate in bone marrow and background structures.

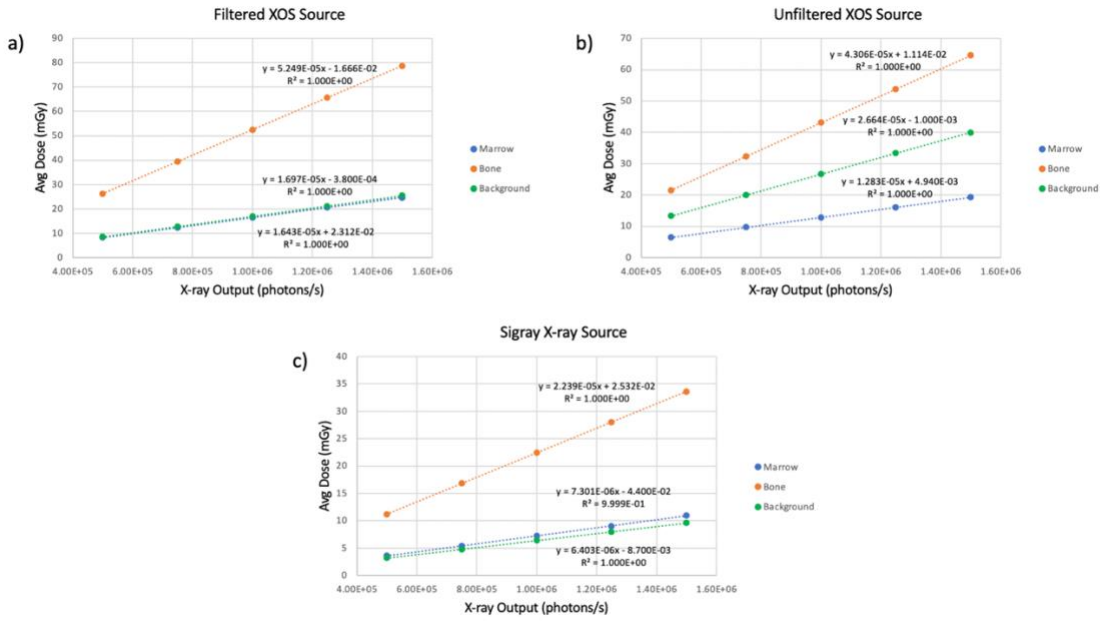

Figure 4.6: Regression line plots of (a) filtered XOS source, (b) unfiltered XOS source, and (c) Sigray source for the different components of the phantom. In (a), the marrow and background plots are overlaid.

4.3.3 Bone marrow dose estimation of a typical XLCT scan

As we reported in our XLCT imaging studies [80, 99, 120], only six angular projections are needed for the narrow beam based XLCT imaging. The X-ray tube output photon number in each linear scan step depends on many factors including the detector sensitivity, the X-ray excitable phosphor particle brightness, the linear scan speed, and the target size

and depth, etc. Generally, it can be assumed that the X-ray photon number is about 10^6 per linear scan. For each angular projection, the radiation dose in bone marrow was calculated to be 7.301 mGy as indicated in Figure 4.7c for the Sigray source case. For a typical XLCT scan with 6 angular projections, we estimate the bone marrow dose to be about 43.806 mGy.

4.3.4 Results of dose map for the mouse model in one projection XLCT imaging

Figure 4.8 shows the central line dose profiles and dose maps from a single angular projection for the different X-ray sources. All the sources had an X-ray photon number of 10^6 per linear scan step. All three cases had 380 linear steps with the same pencil beam size and step size of 100 micrometers. From Figure 4.8a and 4.8c, it is shown that the bone structure absorbed more dose than the other mouse structures which is consistent with the results from the small mouse leg in Figure 4.6. In Figure 4.8b, the bone received little dose due to the limited number of X-rays with enough energy to penetrate to deeper tissues. Most of the dose is seen deposited along the surface of the mouse trunk with little to no dose deposited in deeper tissues due to the bremsstrahlung energies of the unfiltered XOS source. Figure 4.8b also shows greater dose absorbed in air than Figure 4.8a and 8c thus contributing to the dose along the surface of the mouse trunk. In Figure 4.8a, greater shadowing effects are observed compared to Figure 4.6a due to the greater size of the imaging object, therefore less dose is deposited in deeper tissues. With the addition of the Al filter, the mean energy of the X-ray source is increased, and greater transmission is observed thus the superficial tissues of the mouse trunk are spared from dose. Figure 4.8c shows little shadowing effects and more uniformity in the dose distribution due to a greater mean energy of the Sigray source.

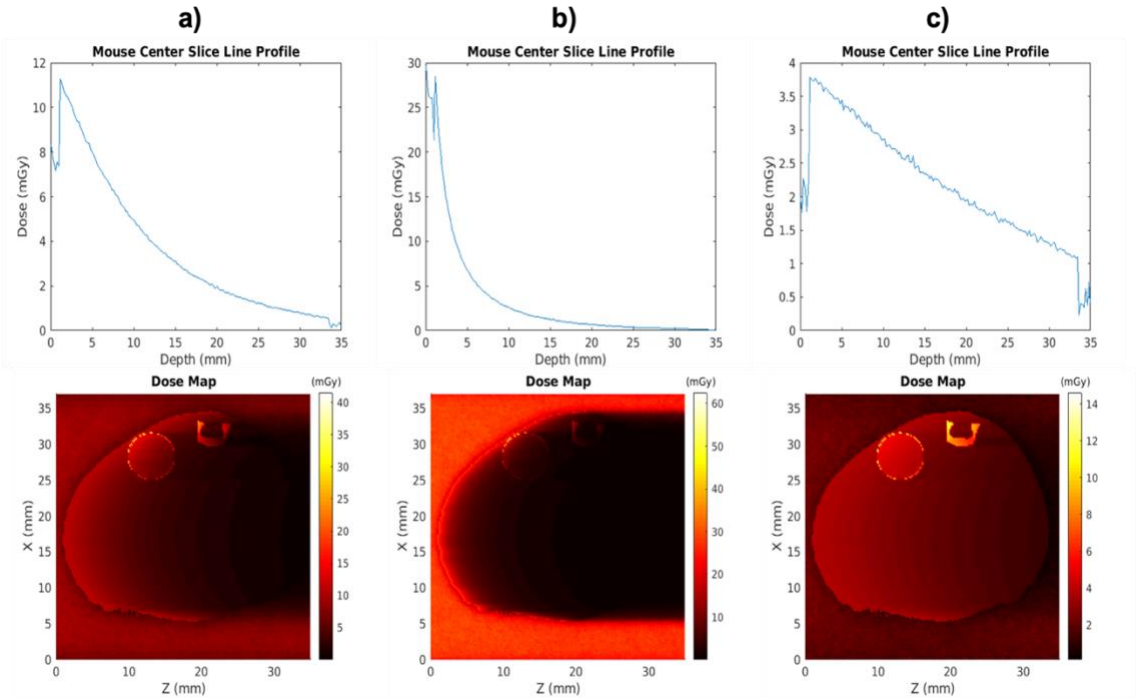

Figure 4.7: Mouse model line profiles and dose maps of (a) Filtered XOS source, (b) Unfiltered XOS source, (c) Sigray source for 10^6 x-ray photons per linear scan step for one angular projection.

4.3.5 Results of the mouse model dose map for a typical XLCT scan

Figure 4.9 shows the total dose maps and central line profiles from six angular projections for the three different X-ray sources. All the sources had an X-ray photon number of 10^6 per linear scan step. All three cases had 380 linear steps with the same pencil beam size and step size of 100 micrometers per angular projection. Figure 4.9a shows that the greatest accumulation of the dose is found at the superficial tissues and the dose falls at a moderate rate in deep tissues as seen in the line profile. In Figure 4.9b, the greatest accumulation of the dose lies strictly on the surface of the mouse model with minimal dose extending to deeper tissues. The line profile of Figure 4.9b shows the dose decreases at an exponential rate in deeper tissues. Due to the drastic dose falloff from the mouse model surface, the tumor and bone structures are not very noticeable in the dose map thus showing little absorbed dose compared to the dose in air. Figure 4.9b also shows the greatest accumulated dose in air when compared with Figure 4.9a and 4.9c which increases the surface dose of the mouse trunk. Figure 4.9c shows a more uniform distribution of the dose compared to Figure 4.9a and 4.9b so that the tumor and bone structures are clearly displayed in the dose map. The line profile from Figure 4.9c shows a dose decrease that resembles a more linear rate. The dose to air in Figure 4.9c is minimal compared to Figure 4.9a and 4.9b. Our results indicate that the surface of the mouse model is spared from additional dose for the case with the Sigray source.

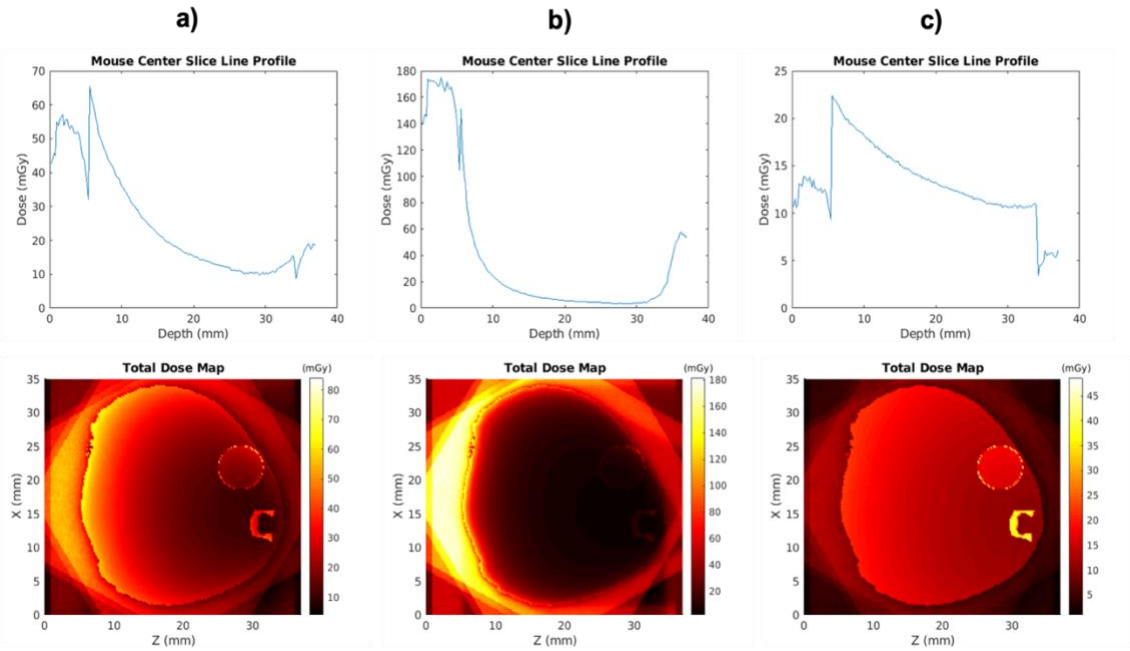

Figure 4.8: Mouse model center slice line profile and total dose maps of (a) Filtered XOS source, (b) Unfiltered XOS source, (c) Sigray source for 10^6 x-ray photons per linear scan step after six angular projections with 30° angle step size.

4.3.6 Mouse model dose estimation based on X-ray photon number for six projection XLCT imaging

Figure 4.10 shows the regression line plots relating the X-ray number per linear scan step (photons/step) to the absorbed average dose (Avg Dose) in milliGray (mGy) units for cases of the filtered XOS source, the unfiltered XOS source, and the Sigray source and for the different components of the mouse model after six angular projections. All regression plots showed a high positive linearity with all R^2 values being greater than 0.97. For the filtered XOS and Sigray source regression plots, the bone structure shows greater values of average absorbed dose than the muscle tissues and tumor. Due to the limited penetrability of the unfiltered XOS source, the muscle tissues show the greatest values for average absorbed dose when compared to the bone and tumor structures as seen in Figure 4.10b. From Figure 4.10, the dose rate for the muscle tissues was the lowest with the Sigray source. The dose rate for the tumor and bone were lowest with the unfiltered XOS source, however, this was due to the low penetrability of the source X-ray photons as seen in Figure 4.9.

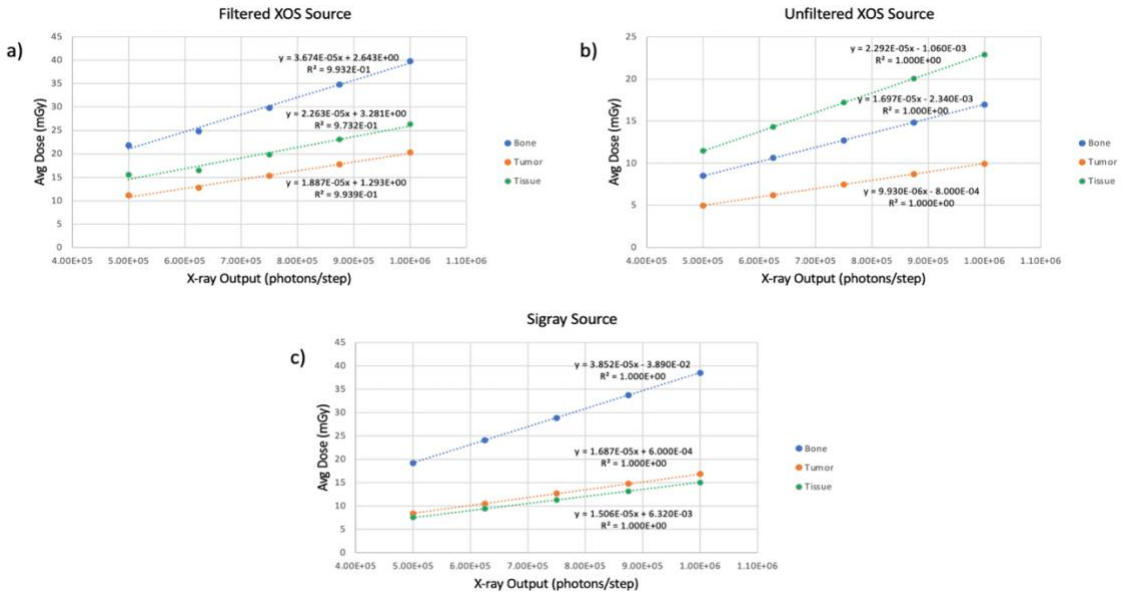

Figure 4.9: Regression line plots of (a) filtered XOS source, (b) unfiltered XOS source, and (c) Sigray source for the different components of the mouse model after six angular projections.

Table 4.1 shows the average dose deposited in the spine bone, muscle tissues, and tumor structures of the mouse model by each source spectra after six angular projections with 10^6 X-ray photons/step. Table 4.1 also shows the dose deposited for the whole mouse model. The muscle tissues absorbed the least amount of dose with the Sigray source. The spine bone and the tumor structures absorbed the least amount of dose with the Unfiltered XOS. The whole body of the mouse model absorbed the least dose with the Sigray source.

Table 4.1: Average (total) dose deposited in the mouse structures by each source spectra after six angular projections with 10^6 x-ray photons/step.

Model Structure	Dose by Filtered XOS	Dose by Unfiltered XOS	Dose by Sigray
Spine bone	39.77 mGy	16.97 mGy	38.49 mGy
Muscle Tissues	20.35 mGy	22.92 mGy	15.07 mGy
Tumor	26.38 mGy	9.93 mGy	16.87 mGy
Whole body	26.28 mGy	22.29 mGy	15.42 mGy

4.4 Discussion

In this chapter, the dose deposited into a 5 mm diameter mouse leg model by one projection pencil beam X-ray imaging was simulated in GATE. Then the dose deposited into a 32 mm diameter mouse model by six projection pencil beam X-ray imaging was simulated. The dose deposited in both models by three different X-ray source spectra was shown and compared. The removal of bremsstrahlung energies results in decreased

superficial dose thus making the filtered XOS source or the Sigray source a better choice for imaging. However, in a practical setting, a source filter will add to the imaging protocol.

Higher mean X-ray energies were observed to give greater dose in deeper depths due to the beam hardening effects. This effect was observed when comparing the unfiltered XOS source to the filtered XOS source results. With the filtered XOS source, the bone structures and bone marrow had greater dose rate as seen in the regression plot in Figure 4.7. X-rays become less susceptible to the photoelectric effect at greater energies therefore the X-rays may be fully absorbed at greater depths which explains the greater background dose and bone dose with the filtered XOS source in the mouse leg model. In the mouse trunk model, this can be observed in the one projection scan.

Due to the size of the imaging objects, the Compton scattering dose effects are minimal compared to the photoelectric effect. However, the photoelectric effect is inversely related to the energy of the X-ray. Therefore, at much greater energies, X-ray transmission is more likely to occur. In the bone marrow model, this explains why the filtered XOS source shows greater dose and dose rates for all structures than the Sigray source. In the mouse model, the greatest absorbed dose for most structures was delivered with the filtered XOS source as seen in Table 4.1. From Figure 4.4 and Fig 4.5, the average energy of the filtered XOS source is lower than the Sigray source, therefore the filtered XOS source is more susceptible to the photoelectric effect which increases the dose of the object tissues. The Sigray source would be a great alternative to other lab sources (like XOS) in XLCT imaging.

For a typical XLCT imaging scan with the Sigray source, more transmitted X-rays will be absorbed to excite the phosphor contrast agents while the surrounding tissues are spared from dose. From Figure 4.9c, the entirety of the mouse trunk absorbed dose to relative levels unlike Figure 4.9a and Fig 4.9b which showed great disparities between the surface and deep tissues. This means that good imaging can be acquired with the Sigray source without concerns of the starting imaging object position and with little concerns of absorbed dose. If a relatively longer scan is required to collect a better phosphor signal, the dose rates for muscle tissues were shown to be minimal when using the Sigray source as seen in Fig 4.10. With the XOS sources, the dose rates are dependent on the starting positions of the imaging object since the source X-ray energies are not as penetrating as the Sigray source. If the mouse model was to have rotated the opposite direction, the dose rates for the bone and tumor with the XOS sources would be much greater than the Sigray source.

XLCT uses X-rays to excite X-ray excitable nanoparticles embedded deep in tissues. The emitted optical photons are collected to reconstruct the image at a good resolution by using the pencil X-ray beam positions as anatomical guidance in the XLCT reconstruction. Unlike XLCT, optical luminescence or fluorescence imaging use nonionizing, low energy optical photons to excite contrast agents and suffer from strong optical scattering in deep tissues that limits the image spatial resolution and the imaging depth. X-ray luminescence imaging offers only 2D imaging of the object while XLCT can offer volumetric imaging of the object if the object is scanned slice by slice.

The dose maps give a distribution of the deposited energy which is good information to know when using nanoparticles in XLCT imaging since the nanoparticles require energy

for excitation to emit the optical photons. With the imaging scheme of six angular projections with 100 μm step size and 10^6 X-rays/step, the total dose was 15.42 mGy if using the Sigray source. Our lab has experimentally measured the accumulated dose of a small phantom object (~25 mm diameter) after six angular projections from an XOS source (~68.6 mGy) [99]. The dose measurements in this work are within the levels of a typical small animal micro-CT scan in which the dose from a scan with 600 projections is >200 mGy [121]. One can estimate the deposited dose in XLCT imaging after considering the effects of projection numbers, imaging time, and X-ray tube currents based on our simulated dose distributions. Furthermore, the dose calculation can be applied for cancer theranostics (like X-ray luminescence induced photodynamic therapy).

It is important to review the concept of dose which has units in Gray (Gy). Dose is defined as the energy absorbed in Joules (J) per unit mass in kilograms (kg). For reference, the dose of a typical abdominal CT imaging for a human patient is ~1.5 mGy, however, this value may vary depending on several factors like the patient size, number of projections, exposure time, and X-ray tube settings [4]. The notable discrepancy between the absorbed dose in human patients and small animal X-ray imaging is due mainly from the following reasons: (1) the mass/size of the imaging object is much larger in human imaging, (2) the X-ray tube energy and current for human imaging is much greater meaning that X-rays are more penetrating, and Compton Scattering is more prevalent which deposits partial dose. However, it is vital to understand the mechanism for imaging between attenuation-based CT imaging and XLCT imaging.

In attenuation-based X-ray imaging the source of contrast is generated through the photoelectric effect in which the X-ray absorption occurs in tissues. An X-ray source with a spectrum where the photoelectric effect is dominant in tissues is more suitable for this form of imaging. In XLCT imaging the source of contrast is radioluminescence in which the X-ray absorption occurs in the embedded contrast agents. Therefore, X-ray sources with greater energies which allow for better transmission and tissue penetrability to excite deep contrast agents and spare tissues from radiation dose are more suitable.

4.5 Conclusion

In summary, dose measurements were first performed on a 5 mm diameter object size, and then performed on a 32 mm diameter mouse model with three different pencil beam X-ray spectra. This work provides insight to the concerns associated with XLCT imaging with a pencil beam geometry. With an adequate X-ray benchtop source with high brilliance and quasi-monochromatic properties like the Sigray source, the dose concerns can be reduced. With the Sigray source, the bone marrow in the mouse leg model was estimated to have a radiation dose of 44 mGy for a typical XLCT imaging with six angular projections and 100 micrometer scan step size and 10^6 X-ray photons per linear scan. With the Sigray source, the spine bone, muscle tissues, and tumor structures of the mouse model received a radiation dose of 38.49 mGy, 15.07 mGy, and 16.87 mGy, respectively. The findings of this work will also be beneficial to other molecular X-ray imaging modalities like X-ray fluorescence computed tomography if it relies on a pencil X-ray beam imaging geometry.

CHAPTER 5

CORRELATION BETWEEN X-RAY TUBE CURRENT EXPOSURE TIME AND X-RAY PHOTON NUMBER

5.1 Introduction

X-ray imaging has remained as the workhorse of medical imaging due to its fast acquisition speeds and high spatial resolution [122]. The intensity of the X-rays is dependent on the X-ray tube current and exposure time. Hybrid X-ray imaging modalities like X-ray luminescence computed tomography (XLCT) and X-ray fluorescence computed tomography (XFCT) rely on the intensity of the X-ray tube to provide an accurate and time efficient image of the nanoprobes in the imaged objects [75, 76, 123]. XLCT and XFCT can use X-ray excitable exogenous contrast agents to monitor drug delivery and track the progression of diseases like cancer [19, 51, 66, 115, 120, 124]. However, the dose absorbed by the imaged sample from X-ray photons is a concern and therefore it limits the image quality and applications [122, 125]. There are ways to measure the X-ray dose experimentally, but current methods are limited and/or standardized to a specific imaging object size and imaging protocol [126-128]. These methods also often include instruments that suffer from oversaturation, pile up effects, energy dependence, temperature dependence, and/or dose rate dependence which reduce the accuracy of the measurements [129-131]. Therefore, it is better to numerically simulate the X-ray imaging to accurately calculate the absorbed dose.

Among the Monte Carlo software available for medical imaging applications, the Monte Carlo software, GATE (Geant4 Application for Tomographic Emission) has gained attentions in medical imaging applications [107-109, 132-134]. However, to model the X-ray imaging system in GATE the X-ray number is needed. The X-ray number in the Monte Carlo GATE software is the number of X-ray photons which will be initialized for the imaging simulation. This X-ray photon number is defined by the user. However, in an experimental imaging protocol, it is the tube current exposure time to be recorded (mAs). One cannot use the tube current exposure time as the input in GATE to simulate the X-ray imaging or dose. Therefore, to model an experimental imaging protocol with an X-ray tub setting in mAs, a method to correlate the X-ray photon number in GATE to the experimental X-ray tub setting in mAs should be explored. So far, to the best of our knowledge, there is no good way to model the X-ray tube's output of X-ray photon number in GATE for a given X-ray tube current.

In this chapter, the X-ray output number from a cone beam micro computed tomography (micro-CT) X-ray tube is estimated using Monte Carlo GATE. An ion chamber is used to record the accumulated exposure in Roentgens (R) of the X-ray tube

for various exposure times. The exposure measurements were then converted to dose in air. The X-ray tube spectrum and measurement setup were modeled in GATE to generate a linear relationship between the radiation dose in the modeled ion chamber and the X-ray photon number. The measurement data and the trendline equations from the GATE simulations were then used to determine the X-ray output number from the dose in the experimental setup for each exposure time. Several aluminum filter thicknesses were incorporated in the experimental imaging protocol to explore the effects of filtration on X-ray output.

The chapter is organized as follows. In section 5.2, the methods of the GATE simulations, experimental setup for source spectra measurements and dose exposure are presented. In section 5.3, the results showing the relationships between X-ray output and dose with different spectra are presented. The chapter concludes with discussions of the results and future works.

5.2 Methods

5.2.1 Experimental setup for X-ray source spectra measurement

The spectrum of an Oxford Instruments X-ray tube (Oxford XTF5011) was acquired using an Amptek CdTe 123 spectrometer. The X-ray tube has a cone angle of 23 degrees and was operated at 50 kVp and 1 μA. To avoid oversaturation and pile up effects, a 2 mm thick, 2 mm diameter pinhole collimator was inserted in the front of the spectrometer sensor. The spectrum was acquired for 60 seconds. The spectra of the X-ray tube with Aluminum (Al) filters of thickness 0.0, 0.5 mm, and 1.0 mm were collected.

5.2.2 Experimental setup for X-ray Exposure Measurement

The X-ray exposure was measured using an Accu-Dose system (Radcal, Monrovia, CA) with a general purpose in-beam ion chamber (10X6-6, Radcal). The Accu-Dose system meter allows for at most 4 digits when making a measurement. The ion chamber head has a diameter of 25 mm and a length of 38 mm. The active component of the ion chamber head has a volume of 6 mm^3. The ion chamber was positioned 17.78 cm away from the X-ray tube window, which is the isocenter of the micro-CT setup. The X-ray tube was operated at 50 kVp and 0.5 mA. The X-ray tube system and the ion chamber were positioned inside a lead cabinet. The Accu-Dose system was placed outside the lead cabinet. The ion chamber cable was fed through a lead cabinet hole to be connected to the Accu-Dose system. The setup of the exposure acquisition and the Accu-Dose system is seen in Figure 5.1. The exposure was acquired in Roentgen units (R) for different exposure times: 1, 2, 4, 8, 10, and 20 seconds which correspond to tube current exposure times: 0.5, 1, 2, 4, 5, 10 mAs.

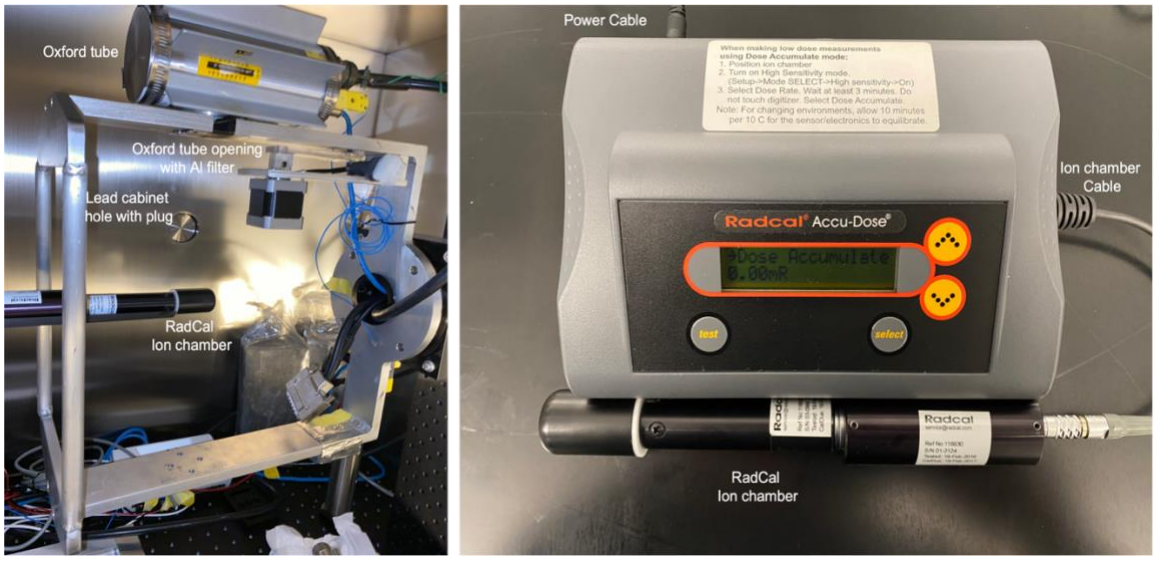

Figure 5.1: Experimental acquisition setup (left) and the Accu-Dose system (right). The Accu-Dose system was positioned outside of the lead cabinet for user control.

Each exposure reading was repeated six times for each exposure time to reduce the variance from the Accu-Dose system measurements. The average exposure was taken from the measurements for each exposure time. The Accu-Dose system measurements account for corrections factors due to temperature and pressure values which may be different from standard temperature and pressure in air. The Dose-to-air in the sensitive volume was found directly from the mean exposure by using the roentgen-to-cGy conversion factor, 0.876 cGy/R [125, 127, 131].

Aside from measuring the accumulated exposure, the Accu-Dose system also allows for the measurement of the exposure rate (R/min). The exposure rate was measured to validate the accuracy of the linear model equations for each Al filter thickness. The exposure rates (slopes) of the linear model equations are compared with the measured exposure rates after conversion from R/mAs to R/min.

5.2.3 GATE simulation setup

A schematic and snapshot of the GATE simulation is seen in Figure 5.2. The ion chamber was modeled as a cylinder with wall material composed of polycarbonate. The sensitive volume of the ion chamber was also modeled as a cylinder of air with 6 cm^3 volume positioned at the center of the ion chamber head. The X-ray tube spectra were imported into GATE using the user spectrum function which by a fixed default normalizes the imported spectra. The GATE simulations employed the GEANT4 emstandard_opt4 physics builder to model the physical processes [134]. In the GATE simulation, the radiation dose was stored in a 3D matrix using the "DoseActor" tool [109]. The mass weighting algorithm was employed for the dose calculations, in which the dose was calculated as the energy deposited per unit mass of the voxel within the dose matrix. The dose matrix was discretized into 25 x 25 x 40 voxels of 1 mm^3 size. 10^6, 2 x 10^6, 10^7, and 2 x 10^7 X-rays were initialized in GATE to create a linear trendline model between the X-

ray number and the radiation dose for each Al filter thickness. The absorbed dose in the modeled ion chamber sensitive volume was masked to only identify the voxels found within the sensitive volume. The dose voxels were then summed to acquire the total absorbed dose in the sensitive volume. The tube X-ray photon number for each measured dose was determined from a trendline model equation. All dose calculations from the modeled ion chamber sensitive volume were performed in MATLAB.

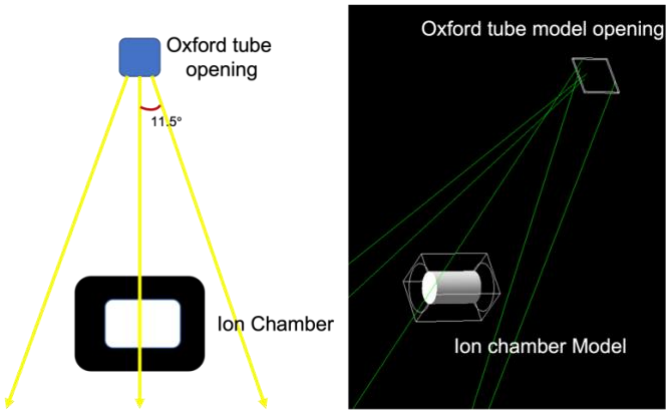

Figure 5.2: Schematic (left) and snapshot (right) of the GATE simulation for the dose acquisition. The green lines in the snapshot are the X-ray beams. The sensitive volume of the ion chamber is modeled as the white cylinder.

5.2.4 X-ray tube output model generation

Linear regression models are used to establish a relationship between the estimated X-ray photon number and the experimental X-ray tube setting. The first regression model establishes a relationship between the experimentally measured X-ray radiation dose and the X-ray tube setting. This model is obtained from fitting experimental measurements acquired with the Accu-Dose system. The second regression model is obtained by fitting the simulated the X-ray radiation dose and the known X-ray photon number in GATE using the captured X-ray tube spectra. By correlating both models, a regression model which estimates the X-ray photon number from the experimental X-ray tube setting is obtained and can be used as an input for GATE simulation for the specific X-ray tube setting.

5.3 Results

5.3.1 X-ray tube spectra

The acquired spectra for each Al filter case are plotted in Figure 5.3. The L-shell energies of the tungsten anode target are clearly visible in Figure 5.3a when no Al filter is used. With 0.5 mm Al thickness, the L-shell energies are effectively attenuated, and their intensity reduced as seen in Fig 5.3b. With 1 mm Al thickness, the L-shell energies are essentially nonexistent as seen in Figure 5.3c. The energies below the bremsstrahlung curve are from Compton scattering effects caused by the Al filter or spectrometer collimator.

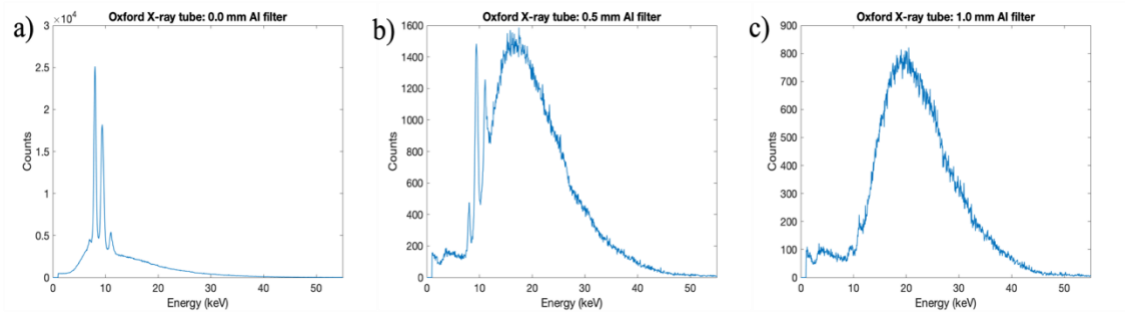

Figure 5.3: Spectrum of the Oxford X-ray tube with different Al thickness: a) 0.0 mm, b) 0.5 mm, c) 1.0 mm.

5.3.2 Measured X-ray radiation dose

Figure 5.4 shows the linear regression plots formed from the mean of the exposure measurements (in Roentgens, R) with the ion chamber for each exposure time (milliampere-seconds, mAs) of the Oxford X-ray tube. All regression plots showed a high positive linearity with all R^2 values being greater than 0.99.

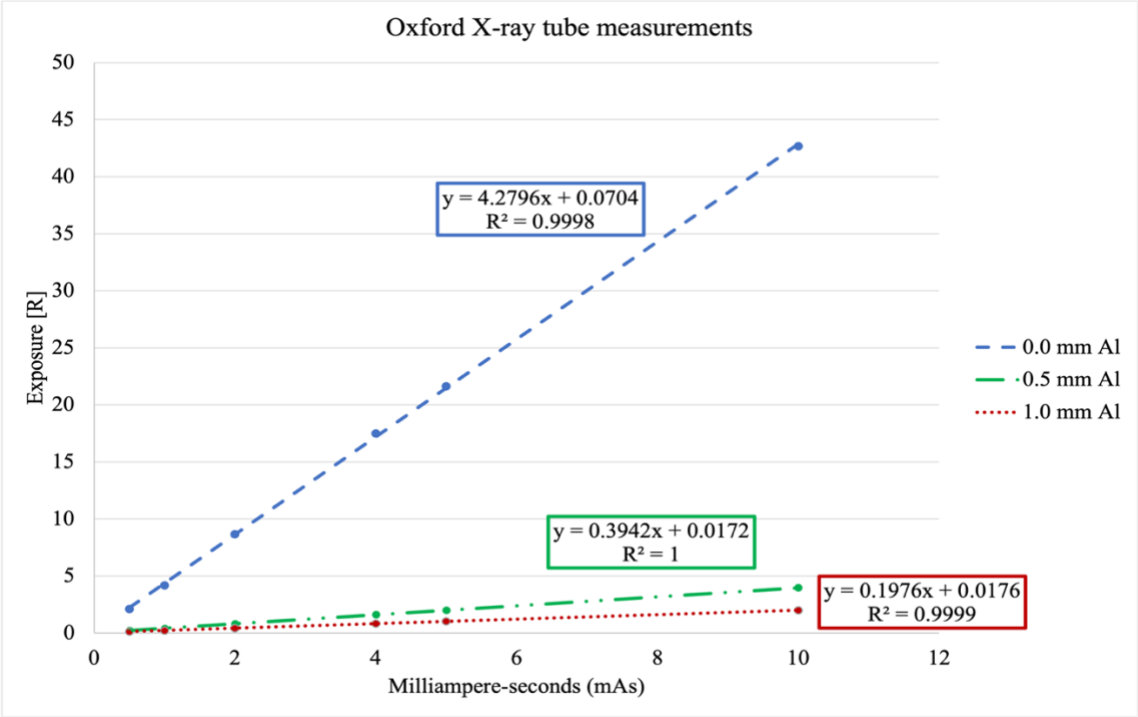

Figure 5.4: Linear regression plots between the mean X-ray radiation dose (R) and the tube current exposure time (mAs). This plot was generated from the tube exposure measurements.

The highest exposure rate was seen without the Al filter due to the absorption of the L-shell energies from the tungsten anode. The plots of the 0.5 mm Al, and 1.0 mm Al are more similar since the L-shell energies have significantly been removed. The lowest exposure rate is seen with 1.0 mm Al filter thickness.

Table 5.1 compares and validates the accuracy of the linear trendlines equations displayed in Figure 5.4. The exposure rates (slopes) of the linear model equations are compared with the measured exposure rates after conversion from R/mAs to R/min. Table 5.1 shows the percent error (PE) between the measured exposure rate and the modeled exposure rate for each Al filter thickness. The modeled exposure rates are obtained from the trendline equations in Figure 5.4. All modeled exposure rates are accurate within 5% of the measured exposure rate. The highest percent error was seen with 1.0 mm Al filter while the lowest percent error was seen with 0.5 Al filter thickness.

Table 5.1: Comparison of the modeled exposure rate to the measured exposure rate at 0.5 mA tube current for each Al filter thickness.

Al filter thickness (mm)	Measured Exposure Rate (R/min)	Modeled Exposure Rate (R/min)	Percent Error (%)
0.0	133.6	128.4	4.050
0.5	11.85	11.83	0.1691
1.0	5.641	5.928	4.841

5.3.3 The radiation dose calculated by GATE

Figure 5.5 shows the linear regression plots relating the X-ray number and the total absorbed dose in cGy for each Al filter thickness. The largest rate is observed with 0.5 mm Al filter thickness, and the lowest rate is observed with 1.0 mm Al filter thickness. A larger number of X-ray photons is required with the 1.0 mm Al filter to achieve a similar dose as the other Al filter thickness. All regression plots showed a high positive linearity with all R^2 values being greater than 0.99. The trendlines equations are used to convert the experimental dose readings into the X-ray output number in GATE for a given current exposure time (mAs).

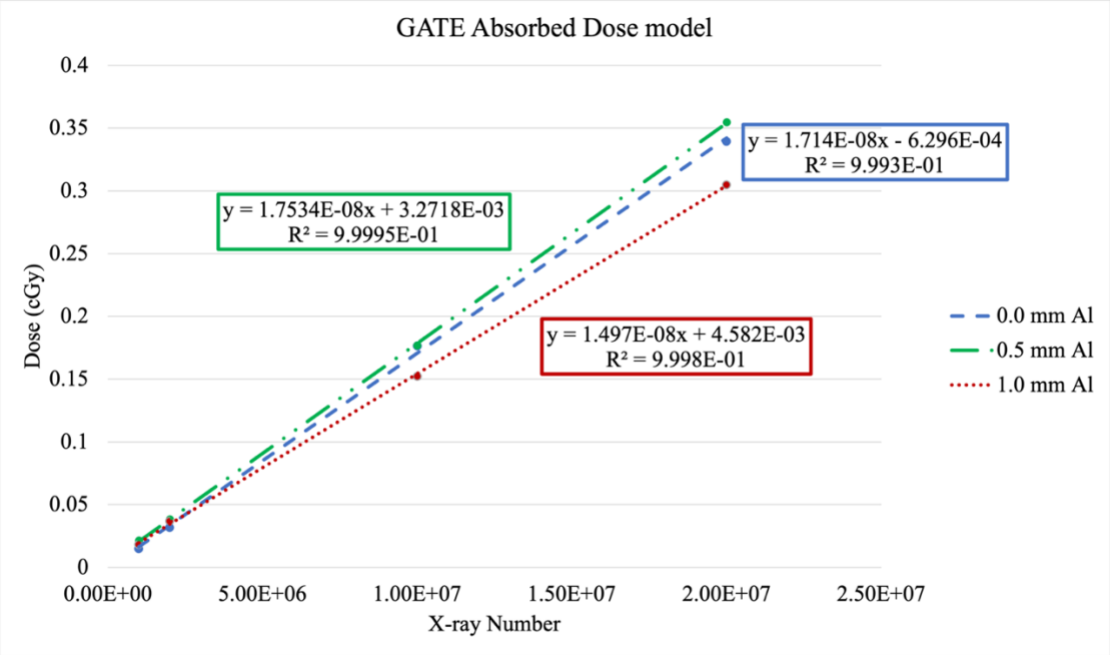

Figure 5.5: Linear regression plots between the X-ray photon number and total absorbed dose (cGy) modeled in GATE.

5.3.4 Correlation between the photon number in GATE and the X-ray tube current

Figure 5.6 shows the plots relating the X-ray number and the exposure time in milliampere-seconds (mAs) for the Oxford X-ray tube. The largest output rate is observed without the Al filter and the lowest output rate is observed with 1.0 mm Al filter thickness. All regression plots showed a high positive linearity with all R^2 values being greater than 0.999.

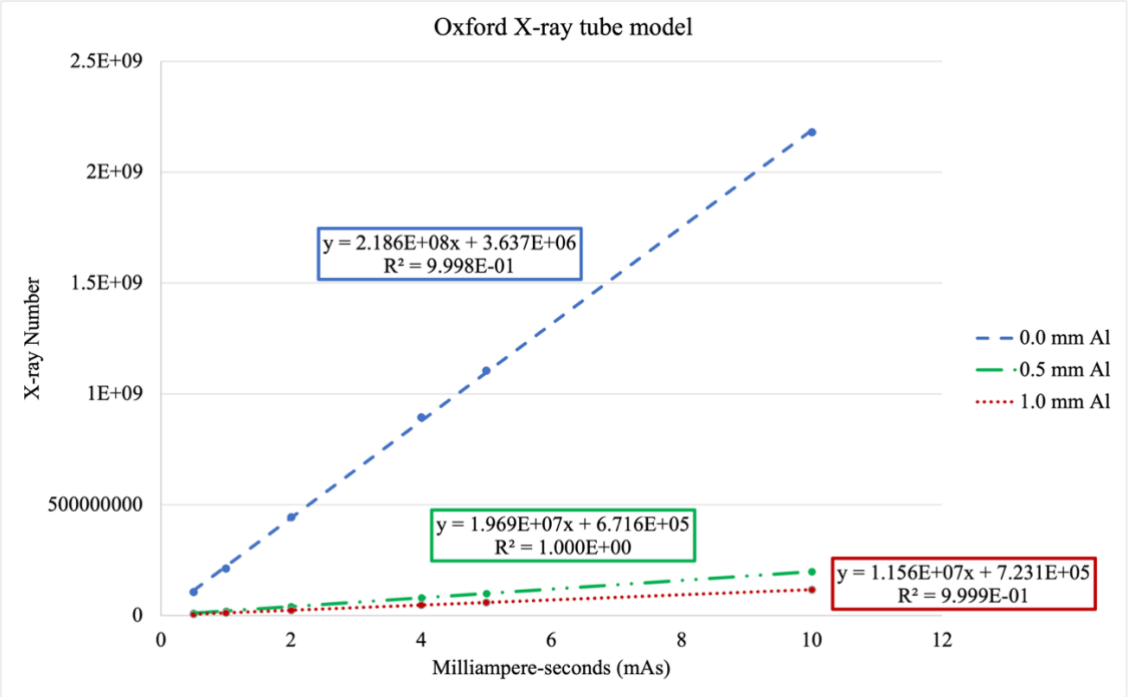

Figure 5.6: Linear regression plots between the X-ray photon number and the exposure time (mAs).

For a typical micro-CT scan, the X-ray tube is operated at 50 kVp and 0.5 mA for a 500 ms exposure time per projection (0.25 mAs). It is standard for a tungsten anode X-ray tube to have a 1.0 mm Al filter to remove the anode L-shell emissions. From Figure 5.6, the X-ray output number per projection can be estimated through linear extrapolation. The X-ray number per projection is estimated to be 3.613×10^6 with 1.0 mm Al filter.

5.4 Discussion

The accuracy of the X-ray output estimate in this work depends heavily on the specifications of the imaging system and dose measurement system. Parameters like the beam cone angle, distance between the source and ion chamber, the size of the sensitive volume inside the ion chamber head, and ion chamber wall material are important to include in the GATE simulation. Another limiting factor is the normalization of the spectrum that GATE performs as a default operation which is hardcoded in the software. The normalized spectrum becomes a probability distribution of energies from which GATE selects randomly when an X-ray is initialized. A high number of X-rays needs to be initialized to generate X-rays with an energy distribution like the original spectrum.

The increased exposure rate with decreased Al filter thickness is due to the reduced average beam energy with lower filter thickness. From Figure 5.3, it can be observed that the average X-ray energy increases with greater Al filter thickness since the filter removes the L-shell energies of the tungsten anode seen in Figure 5.3a. The physical process responsible for a large contribution of the dose is the photoelectric effect which is inversely

proportional to the X-ray energy. Therefore, the highest dose rate is observed without the Al filter.

The curves of Figure 5.4 are more different compared to the curves of Figure 5.5 which are more similar. Note that Figure 5.4 shows the relationship between the experimentally measured exposure and the X-ray tube mAs setting while Figure 5.5 shows the relationship between the absorbed dose and the X-ray photon number simulated in GATE. In Figure 5.4, the curve without an Al filter is much greater than the other curves since more X-rays are being emitted for the tube current exposure time (mAs) setting. The X-ray spectrum associated with this curve is Figure 5.3a. This spectrum shows the L-shell energy emission of the tungsten anode of the X-ray tube. L-shell energies are very bright (intense) due to their high interaction cross section. The L-shell energies are attenuated and removed as the Al thickness is increased. Therefore, the intensities of the other spectra (Figure 5.3b and Figure 5.3c) are not as great as in Figure 5.3a. The similarity in the curves of Figure 5.5 is due to the X-ray number being the same for all Al thickness spectra and so the intensity of each spectrum is the same unlike Figure 5.4 which results in little variation of the dose.

In Figure 5.5, the highest dose rate is observed with the 0.5 mm Al filter. This may be due to the greater effective energy with 0.5 mm Al which allows for the X-rays to become more penetrative. This leads to more dose onto the sensitive volume of the modeled ion chamber after the X-rays have traversed the ion chamber wall. However, little difference in the dose rates is observed when the 0 mm Al filter or 0.5 Al filter is used compared with the 1 mm Al filter. Without an Al filter, some of the L-shell energies of the target anode can pass the chamber wall and deposit their energy onto the sensitive volume of the ion chamber since the L-shell energies are most intense without the Al filter.

Figure 5.6 is the final model result which gives an estimation of the X-ray tube photon number for an X-ray tube current exposure time setting. Figure 5.6 is our final goal of this study, from which one can find the X-ray photon number as input in GATE for any experimental X-ray tube settings (mAs). By having a better estimation of the X-ray tube output, the radiation dose for an imaging protocol can be accurately estimated without using standardized methods.

The ion chamber was positioned at the iso-center since that is the position of the imaged object and the ion chamber is fully covered by the X-ray tube cone beam. In this work, the X-ray photon number in the X-ray beam after filtering is correlated with the X-ray tube current. To correlate the photon number before filtering including the factor of X-ray self-attenuation, more detailed information of the X-ray tube product is required. However, intellectual property right is an obstacle to circumvent.

The trendline coefficient of determinations between X-ray number and absorbed dose is consistent with previous work and literature in which a strong linear relationship with a high coefficient of determination, $R^2 >= 0.97$ between the X-ray number and the radiation dose exists [77, 125]. The trendline equations and X-ray photon numbers in this work are within standard small animal X-ray imaging parameters [77, 121].

This work can be applicable to any X-ray tube that uses the cone or fan beam geometry if the sensitive volume of the ion chamber can be completely covered by the X-ray beam or if good partial volume response can be achieved with the ion chamber. For smaller X-

ray beams, like pencil beams, film dosimetry or diode edge detectors need to be integrated into the presented method.

5.5 Conclusion

In this work, the X-ray tube output of a small animal micro-CT imaging system was estimated using Monte Carlo GATE. Exposure measurements were performed on the imaging system using an ion chamber. By comparing the simulated dose in GATE with the measured dose in the experimental setup, the X-ray photon number is found to be linearly correlated with the X-ray tube current exposure time in mAs. The linear correlation is changed with different X-ray filters. From the linear correlation, it is straightforward to setup the X-ray photon number in the GATE simulations according to the desired exposure time. The proposed method offers a simple solution to measure the X-ray photon number from an X-ray tube for any imaging design/X-ray tube setting. From the X-ray output estimate, Monte Carlo software like GATE can be used to measure the radiation dose delivered to the imaging object which is more accurate than standardized methods. In the future work, X-ray photon number estimation methods will be explored in pencil beam-based X-ray imaging system.

Acknowledgements: I would like to thank Yile Fang. Yile helped with the measurement of the X-ray tube spectra. I was responsible for the exposure measurements, GATE simulations, linear models, and data analysis.

CHAPTER 6

CONCLUDING REMARKS AND FUTURE DIRECTIONS FOR PRECLINICAL FUNCTIONAL X-RAY IMAGING

6.1 Concluding Remarks

Functional X-ray imaging has demonstrated to circumvent obstacles associated with optical imaging modalities and functional imaging modalities. XLCT combines the high spatial resolution of CT imaging with the high measurement sensitivity of optical imaging. XLCT mitigates the ill-posedness of deep tissue optical imaging by incorporating the pencil beam imaging geometry which is used as structural guidance for image reconstruction. XFCT combines the high spatial resolution of CT imaging with the material analysis capabilities of XF. XFCT evades the half-life limitations associated with radiotracers used in nuclear medicine imaging techniques and can provide greater spatial resolution when the pencil beam geometry is used. In this dissertation, potential preclinical functional X-ray imaging advancements in XFCT and XLCT were investigated.

The feasibility of the time domain method in XLCT imaging was first explored. The problem framework, the forward model, and the reconstruction algorithm of a time domain XLCT for lifetime imaging with high spatial resolution was proposed and investigated with MATLAB simulations. Unlike the reconstructed light yield images, the reconstructed lifetime images were found to be robust to noise levels up to 5% and to unknown optical properties up to 4 times the absorption and scattering coefficients. A preliminary experimental study to measure the X-ray pulses and resulting GOS:Eu^{3+} optical pulses was also presented. The GOS:Eu^{3+} optical pulses were found to be much longer lived than the X-ray pulses especially when the X-ray pulse frequency was increased.

The feasibility of a high resolution XFCT imaging system was investigated. A benchtop XFCT imaging system with a superfine pencil-beam X-ray source and a ring of X-ray spectrometers was simulated using GATE Monte Carlo software. The fNUMOS algorithm used in XLCT image reconstruction was used to reconstruct the XFCT image of molybdenum (Mo) NP targets. Good target localization was achieved with a DICE coefficient of 88.737%. The reconstructed signal of the targets was found to be proportional to the target concentrations if detector number, detector placement, and angular projection number were optimized. The fNUMOS algorithm performance was compared with the maximum likelihood expectation maximization (ML-EM) and filtered back projection (FBP) algorithms. The results indicated that the fNUMOS is superior to the ML-EM and FBP algorithms. The fNUMOS algorithm was also able to reconstruct XFCT targets as small as 0.25 mm in diameter. The results showed that measurements with three angular

projections and a 20-detector ring were enough to reconstruct the XFCT images. A preliminary experimental XFCT study was also performed using an XOS X-ray tube with 100 um beam diameter and a single CdTe detector. A 12 mm diameter cylindrical agar phantom with a 4 mm diameter 1%wt Au target was scanned. Next a 20 mm diameter cylindrical air phantom with three targets of different Au concentrations was scanned. The fNUMOS algorithm was used for the image reconstruction. For the agar phantom, a DICE coefficient of 51.84% was achieved. For the air phantom, the fNUMOS algorithm was unsuccessful in accurately reconstructing the targets due to the high level of noise, however, the target concentrations were localized.

Typically, the radiation dose of pencil beam XLCT imaging is difficult to measure due to instrumentation limitations. Therefore, it is best to calculate the dose with Monte Carlo methods. The dose deposited in pencil beam XLCT imaging was investigated to estimate the dose from one angular projection scan with three different X-ray sources. The dose deposited in a typical small animal XLCT imaging was also investigated. GATE was used to estimate the dose from one angular projection scan of a mouse leg model with three different X-ray sources. Dose estimations from a six angular projection scan by three different X-ray source energies were performed in GATE on a mouse trunk model composed of muscle, spine bone, and a tumor. With the Sigray source, the bone marrow of mouse leg was estimated to have a radiation dose of 44 mGy for a typical XLCT imaging with six angular projections, a scan step size of 100 micrometers, and 10^6 X-ray photons per linear scan. With the Sigray X-ray source and the typical XLCT scanning parameters, the estimated dose for spine bone, muscle tissues, and tumor structures of the mouse trunk were 38.49 mGy, 15.07 mGy, and 16.87 mGy, respectively which are found to be within the dose range of a typical small animal microCT scan. The results indicated that an X-ray benchtop source (like the X-ray source from Sigray Inc.) with high brilliance and quasi-monochromatic properties can reduce dose concerns associated with the pencil beam geometry. The findings of this work can be applicable to other imaging modalities like XFCT if the imaging protocol consists of the pencil beam geometry.

Finally, an X-ray tube output estimation method was explored. The accumulated radiation dose of a microCT X-ray tube at different current exposure times was recorded with a general-purpose ion chamber. GATE was used to model the experimental microCT imaging system and record the total absorbed dose (cGy) in the sensitive volume of the ion chamber with different X-ray photon numbers. Linear regression models were used to establish a correlation between the estimated X-ray photon number and the X-ray tube settings. At first, one model establishes the relationship between the experimentally measured dose and the X-ray tube setting. Then, another model establishes a relationship between the simulated dose and the X-ray number in GATE. At last, by correlating these two models, a regression model to estimate the X-ray output number from an experimental X-ray tube setting (milliampere-seconds (mAs)) is obtained. For a typical micro-CT scan, the X-ray tube is operated at 50 kVp and 0.5 mA for a 500 ms exposure time per projection (0.25 mAs). For these X-ray imaging parameters, the X-ray number per projection was estimated to be 3.613×10^6 with 1.0 mm Al filter. The findings of this work provide a workflow to correlate the experimental X-ray tube current exposure time (mAs) to the X-ray photon number in the GATE simulation of the X-ray tube to determine the radiation

dose more accurately for an imaging protocol without the need of standardized equipment or standardized techniques.

6.2 Future Directions

While this dissertation has been computationally intensive work, it has laid out a foundation to carry out future experimental work. A future work is the development of X-ray excitable nanophosphors which are sensitive to microenvironmental parameters like oxygen concentrations and pH to be use for time domain XLCT experiments. While no X-ray excitable nanophosphors exist which are sensitive to microenvironmental parameters like oxygen, it is possible to attach a nanophosphor to an optical agent (dye) which is responsive to these parameters of interest. Sensitivity of the dye to the microenvironmental parameter of interest will cause a reduction of the emission intensity of the dye over time. For the energy transfer to occur, the emission spectra of the donor (nanophosphor) must overlap with the absorption spectra of the acceptor (dye). We are in collaboration with Dr. Anker's group at Clemson University to develop such particle.

Another future work is the development of an XFCT system with a bright Sigray source. We are in collaboration with the Sigray company to incorporate a bright X-ray source onto our benchtop XFCT system. The bright X-ray source will increase XF photon production which will increase the sensitivity of our benchtop XFCT system. More spectrometers will be included in the imaging system to accelerate the acquisition.

We also plan to incorporate machine learning algorithms to further improve the sensitivity and imaging efficiency of XFCT imaging. Preliminary work has been conducted in XLCT in which a proposed deep learning algorithm was used to reduce the number of measurements [135]. We propose to use the same deep learning algorithm in the XFCT system. Other machine learning algorithms exist which can help improve our XFCT system performance [136-138].

We have investigated the time of flight computed tomography (TOF-CT) imaging method as a scatter rejection method for contrast enhancement in small objects [139]. The time of flight (TOF) cone beam computed tomography (CBCT) was recently shown to reduce the X-ray scattering effects by 95% and improve the image CNR by 110% for large volume objects like in abdominal CT imaging [140]. The advancements in X-ray sources like in compact Free Electron Lasers (FEL) and advancements in detector technology show potential for the TOF method to be feasible in CBCT when imaging large objects. GATE Monte Carlo software was used to simulate the CT imaging of an 8 cm diameter cylindrical water phantom with two bone targets using a modeled 20 keV quasi-energetic FEL source and various TOF resolutions ranging from 1 to 1000 ps. An inhomogeneous breast phantom of similar size with a tumor target was also imaged using the same system setup. The simulation study indicated that a TOF resolution below 10 ps was required to see notable enhancements in the image quality and scatter reduction for small objects around 8 cm in diameter as seen in Figure 6.1 and Figure 6.2. Figure 6.1 shows the TOF CT results of a 8 cm cylindrical phantom with bone targets. Figure 6.1a show the line profiles with various TOF resolutions of the reconstructed cylinder along the yellow line from Figure 6.1b. Figure 6.1b shows reconstructed axial slices of the cylinder phantom with 10 ps TOF

scatter rejection and without TOF rejection. Figure 6.2 shows the TOF CT results of an 8 cm numerical breast phantom. Figure 6.2a shows line profiles of the reconstructed TOF CT images for the breast phantom with various TOF resolutions along the yellow line from Figure 6.2b. Figure 6.2b shows reconstructed breast images with 5 ps TOF scatter rejection and without TOF scatter rejection. The strong scattering from targets such as bone can result in substantial improvements by the TOFCT. In the future, we plan to collaborate with institutions like Stanford University to experimentally explore the TOF-CT scatter rejection method using a bright X-ray source like a synchrotron source and a TOF detector.

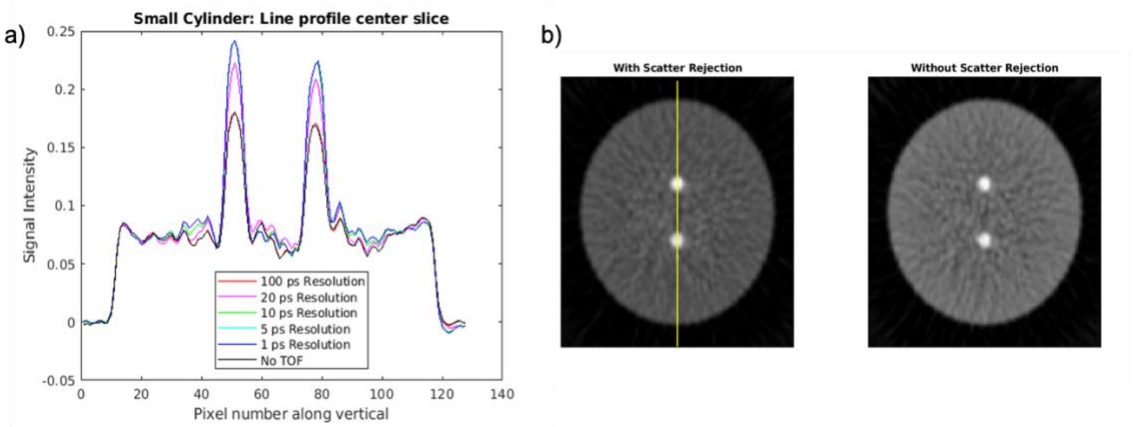

Figure 6.1: TOF CT results of the small cylindrical phantom. a) Line profiles with various TOF resolutions; b) Cylinder slices of the reconstructed TOF CT images with 10 ps TOF scatter rejection and without TOF scatter rejection.

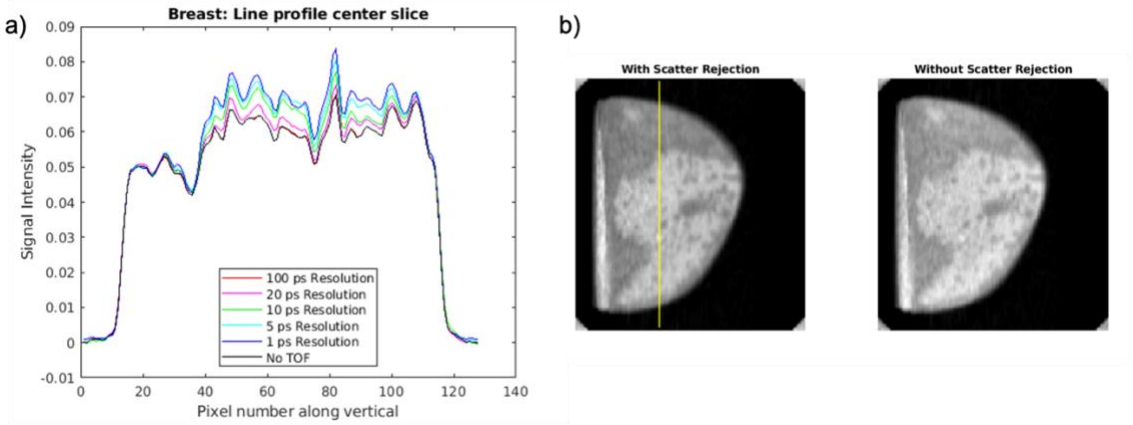

Figure 6.2: TOF CT results of the numerical breast phantom. a) Line profiles of the reconstructed TOF CT images for the breast phantom with various TOF resolutions. b) Reconstructed breast images with 5 ps TOF scatter rejection and without TOF scatter rejection.

We have also explored speckle-based phase contrast X-ray imaging as another method to enhance the contrast of CT imaging. Speckle-based phase contrast X-ray imaging employs the use of a thin diffuser object (i.e sandpaper) to generate a random speckle pattern on the detector [141-144]. The imaging object is then inserted along the trajectory of the X-rays. Multiple translations of the diffuser along the transverse direction of the

beam generate speckle pattern changes of the imaging object. Analysis of the speckle pattern changes creates an enhancement in the imaging object contrast. Recently, a computer vision algorithm known as optical flow has been incorporated in the image reconstruction of speckle-based phase contrast imaging in which a single exposure of the imaging object is enough to reconstruct the image and enhance the image contrast [145, 146]. We first validated the optical flow method on a nylon wire using GATE in which a significant improvement in the contrast was observed from a conventional attenuation-based image as seen in Figure 6.3. Figure 6.3a shows the attenuation-based nylon wire image while Figure 6.1b shows the phase shift image of the nylon wire. Currently, we are simulating a numerical breast phantom with an embedded 1 cm cyst in GATE. We will apply the optical flow method to observe contrast improvement of the embedded cyst. In the future, we will collaborate with companies like Sigray, Olympus, and Thor Labs to build an experimental speckle-based phase contrast X-ray imaging system.

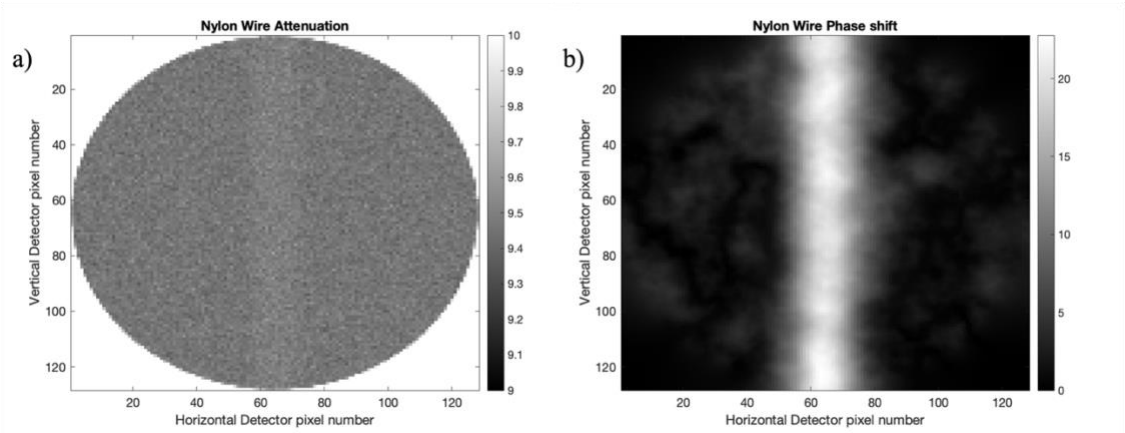

Figure 6.3: Comparison of the image contrast of nylon wire. a) Nylon wire attenuation image. b) Nylon wire phase shift image

REFERENCES

[1] R.F. Mould, *"The early history of x-ray diagnosis with emphasis on the contributions of physics in 1895-1915",* Phys. Med. Biol. **40** (1995) 1741-1787

[2] François Pontana, Julien Pagniez, Thomas Flohr, Jean-Baptiste Faivre, Alain Duhamel, Jacques Remy, and Martine Remy-Jardin. Chest computed tomography using iterative reconstruction vs filtered back projection (part 1): evaluation of image noise reduction in 32 patients. *European radiology*, 21 (3): 627–635, 2011

[3] Andrew Webb and George C Kagadis. Introduction to biomedical imaging. *Medical Physics*, 30 (8): 2267–2267, 2003.

[4] Simon R Cherry, Y Shao, RW Silverman, K Meadors, S Siegel, A Chatziioannou, JW Young, W Jones, JC Moyers, D Newport, *et al*. MicroPET: a high-resolution PET scanner for imaging small animals. *IEEE Transactions on Nuclear Science*, 44 (3): 1161– 1166, 1997.

[5] Jinyi Qi and Richard M Leahy. Iterative reconstruction techniques in emission computed tomography. *Physics in Medicine & Biology*, 51 (15): R541, 2006.

[6] Yang YF, Wu YB, Qi JY, James SS, Du HN, Dokhale PA, Shah KS, Farrell R, Cherry SR. A prototype PET scanner with DOI-encoding detectors. J Nucl Med. 2008;49(7):1132-40. PMCID: PMC2662710.

[7] Peremans K, Cornelissen B, Van den Bossche B, Audenaert K, Van de Wiele C. A review of small animal imaging planar and pinhole SPECT Gamma camera imaging. *Vet Radiol Ultrasoun*. 2005;46(2):162-70.

[8] Hendee, W. R., Ritenour, E. R. & Hoffmann, K. R. Medical Imaging Physics, Fourth Edition. *Medical Physics* 30, 730–730 (2003)

[9] Caravan P. Strategies for increasing the sensitivity of gadolinium-based MRI contrast agents. Chem Soc Rev. 2006;35(6):512-23.

[10] Wang G, Cong WX, Durairaj K, Qian X, Shen H, Sinn P, Hoffman E, McLennan G, Henry M. In vivo mouse studies with bioluminescence tomography. Opt Express. 2006;14(17):7801-9

[11] Gao M, Lewis G, Turner GM, Soubret A, Ntziachristos V. Effects of background fluorescence in fluorescence molecular tomography. Appl Opt. 2005;44(26):5468-74

[12] V. Ntziachristos, J. Ripoll, and R. Weissleder, *"Would infrared fluorescence signals propagate through large human organs for clinical studies?",* Opt. Lett. **27**, 333-335 (2002)

[13] Zong, W. *et al.* Fast high-resolution miniature two-photon microscopy for brain imaging in freely behaving mice. *Nature Methods* **14,** 713–719 (2017)

[14] Yoon, S. *et al.* Deep optical imaging within complex scattering media. *Nature Reviews Physics* **2,** 141–158 (2020)

[15] Li CQ, Mitchell G, Dutta J, Ahn S, Leahy R, Cherry S. A three-dimensional multispectral fluorescence optical tomography imaging system for small animals based on a conical mirror design. Opt Express. 2009;17(9):7571-85. PMCID: PMC2852255

[16] Li CQ, Wang G, Qi J, Cherry S. Three-dimensional fluorescence optical tomography in small-animal imaging using simultaneous positron-emission-tomography priors. Opt Lett. 2009;34(19):2933-5. PMCID: PMC2856619.

[17] Thomas Beyer, David W Townsend, Tony Brun, Paul E Kinahan, *et al*. A combined PET/CT scanner for clinical oncology. *The Journal of nuclear medicine*, 41 (8): 1369, 2000.

[18] Andreas Boss, Sotirios Bisdas, Armin Kolb, Matthias Hofmann, Ulrike Ernemann, Claus D Claussen, Christina Pfannenberg, Bernd J Pichler, Matthias Reimold, and Lars Stegger. Hybrid PET/MRI of intracranial masses: initial experiences and comparison to PET/CT. *Journal of Nuclear Medicine*, 51 (8): 1198–1205, 2010

[19] Vernekohl D. X-Ray Excited Fluorescent Materials for Medical Application. *Top Med Chem*. Vol 9.; 2014:1-68. doi:10.1007/7355

[20] G. Pratx, C.M. Carpenter, C. Sun, R. Rao, and L. Xing, *"Tomographic molecular imaging of x-ray excitable nanoparticles",* Opt. Lett. 35, 3345-3347 (2010)

[21] H. Chen, D.E. Longfield, V.S. Varahagiri, K.T. Nguyen, A.L. Patrick, H. Qian, D.G. VanDerveer, and J.N. Anker, *"Optical imaging in tissue using X-ray excited luminescenct sensors",* Roy. Chem. Soc. Analyst, **136**, 3438-45 (2011).

[22] H. Chen, A.L. Patrick, Z. Yang, D.G. Vanderveer, and J.N. Anker, *"High- resolution Chemical Imaging Through Tissue with an X-ray Scintillator Sensor",* ACS Analy. Chem. **83**, 5045-49 (2011)

[23] Pratx, *"A tale of two photons: radioluminescence and its application in molecular imaging",* Proc. of SPIE, Vol. 10049, 1004916 (2017)

[24] Zhang, W., Zhu, D., Zhang, K. & Li, C. Microscopic x-ray luminescence computed tomography. in Multimodal Biomedical Imaging X 9316, 93160M (SPIE, 2015)

[25] G. Pratx, C.M. Carpenter, C. Sun, and L. Xing, *"X-ray luminescence computed tomography via selective excitation: a feasibility study",* IEEE Trans. Med. Imag 29, 1992-99 (2010)

[26] W. Cong, H. Shen, and G. Wang, ''Spectrally resolving and scattering- compensated X-ray luminescence/fluorescence computed tomography,'' J. Biomed. Opt., vol. 16, no. 6, pp. 066014-1–066014-7, 2011

[27] C. M. Carpenter, C. Sun, G. Pratx, H. Liu, Z. Cheng, and L. Xing, ''Radioluminescent nanophosphors enable multiplexed small-animal imaging,'' Opt. Exp., vol. 20, no. 11, pp. 11598–11604, May 2012

[28] C. Li, K. Di, J. Bec, and S. R. Cherry, ''X-ray luminescence optical tomography imaging: Experimental studies,'' Opt. Lett., vol. 38, no. 13, pp. 2339–2341, Jul. 2013

[29] D. Chen, S. Zhu, H. Yi, X. Zhang, Du. Chen, and J. Liang, *"Cone beam x-ray luminescence computed tomography: a feasibility study",* Med. Phys. **40** (3) (2013)

[30] G. Zhang, F. Liu, J. Liu, J. Luo, Y. Xie, J. Bai, and L. Xing, *"Cone beam x-ray luminescence computed tomography based on Bayesian method",* IEEE Trans. on Med. Imag. **36** (1) 225-235 (2017)

[31] X. Liu, Q. Liao, and H. Wang, *"In vivo x-ray luminescence tomographic imaging with single-view data",* Opt. Lett. **38** (22) (2013)

[32] S. Tzoumas, D. Vernekohl, and L. Xing, *"Coded-aperture compressed sensing x-ray luminescence tomography",* IEEE Trans. on Biomed. Eng. **65** (8) (2017)

[33] X. Liu, H. Wang, M. Xu, S. Nie, and H. Lu, *"A wavelet-based single view reconstruction approach for cone beam x-ray luminescence tomography imaging",* Biomed. Opt. Expr. **5** (11) (2014)

[34] W. Cong and G. Wang, *"X-ray fan-beam luminescence tomography",* Austin J. of Biomed. Eng. **1** (5) (2014).

[35] D. Chen, S. Zhu, X. Cao, F. Zhao, and J. Liang, *"X-ray luminescence computed tomography imaging based on X-ray distribution model and adaptively split Bregman method",* Biomed. Opt. Expr. **6** (7) (2015)

[36] B. Quigley, C.D. Smith, S. Cheng, J.S. Souris, C.A. Pelizarri, C. Chen, L. Lo, C.S. Reft, R.D. Wiersma, and P.J. La Riviere, *"Sensitivity evaluation and selective plane*

imaging geometry for x-ray induced luminescence imaging", Med. Phys. **44** (10) 5367-5377 (2017)

[37] P. Boisseau and L. Grodzins, ‘‘Fluorescence tomography using synchrotron radiation at the NSLS,’’ Hyperfine Interact., vol. 33, nos. 1–4, pp. 283–292, Mar. 1987.

[38] T. Takeda et al., ‘‘X-ray fluorescent CT imaging of cerebral uptake of stable-iodine perfusion agent iodoamphetamine analog IMP in mice,’’ J. Synchrotron Radiat., vol. 16, no. 1, pp. 57–62, Jan. 2009.

[39] S.-K. Cheong, B. L. Jones, A. K. Siddiqi, F. Liu, N. Manohar, and S. H. Cho, ‘‘X-ray fluorescence computed tomography (XFCT) imaging of gold nanoparticle-loaded objects using 110 kVp X-rays,’’ Phys. Med. Biol., vol. 55, no. 3, pp. 647–662, Feb. 2010.

[40] M. Bazalova, Y. Kuang, G. Pratx, and L. Xing, ‘‘Investigation of X-ray fluorescence computed tomography (XFCT) and K-edge imaging,’’ IEEE Trans. Med. Imag., vol. 31, no. 8, pp. 1620–1627, Aug. 2012

[41] Y. Kuang, G. Pratx, M. Bazalova, B. Meng, J. Qian, and L. Xing, ‘‘First demonstration of multiplexed X-ray fluorescence computed tomography (XFCT) imaging,’’ IEEE Trans. Med. Imag., vol. 32, no. 2, pp. 262–267, Feb. 2013.

[42] B. L. Jones, N. Manohar, F. Reynoso, A. Karellas, and S. H. Cho, ‘‘Experimental demonstration of benchtop X-ray fluorescence computed tomography (XFCT) of gold nanoparticle-loaded objects using lead- and tin-filtered polychromatic cone-beams,’’ Phys. Med. Biol., vol. 57, no. 23, p. N457, Dec. 2012.

[43] Fu G, Meng L-J, Eng P, Newville M, Vargas P, La Riviere P. Experimental demonstration of novel imaging geometries for x-ray fluorescence computed tomography. *Medical Physics.* 2013;40:061903, 11

[44] H. M. Hertz, J. C. Larsson, U. Lundström, D. H. Larsson, and C. Vogt, ‘‘Laboratory X-ray fluorescence tomography for high-resolution nanopar- ticle bio-imaging,’’ Opt. Lett., vol. 39, no. 9, pp. 2790–2793, May 2014.

[45] L. Vincze et al., ‘‘Three-dimensional trace element analysis by confocal X-ray microfluorescence imaging,’’ Anal. Chem., vol. 76, no. 22, pp. 6786–6791, Nov. 2004.

[46] N. Gao, I. Y. Ponomarev, Q. F. Xiao, W. M. Gibson, and D. A. Carpenter, ‘‘Monolithic polycapillary focusing optics and their applications in microbeam X-ray fluorescence,’’ Appl. Phys. Lett., vol. 69, no. 11, pp. 1529–1531, Sep. 1996.

[47] A. R. Woll et al., ‘‘Development of confocal X-ray fluorescence (XRF) microscopy at the Cornell high energy synchrotron source,’’ Appl. Phys. A, vol. 83, no. 2, pp. 235–238, May 2006.

[48] F. E. Carroll, M. H. Mendenhall, R. H. Traeger, C. Brau, and J. W. Waters, ‘‘Pulsed tunable monochromatic X-ray beams from a compact source: New opportunities,’’ Amer. J. Roentgenol., vol. 181, no. 5, pp. 1197–1202, Nov. 2003

[49] K. Nakajima, ‘‘Compact X-ray sources: Towards a table-top free-electron laser,’’ Nature Phys., vol. 4, no. 2, pp. 92–93, Feb. 2008.

[50] M. Ahmad, M. Bazalova, L. Xiang, and L. Xing, ‘‘Order of magnitude sensitivity increase in X-ray fluorescence computed tomography (XFCT) imaging with an optimized spectro-spatial detector configuration: Theory and simulation,’’ IEEE Trans. Med. Imag., vol. 33, no. 5, pp. 1119–1128, May 2014.

[51] Bazalova-Carter M. The potential of L-shell X-ray fluorescence CT (XFCT) for molecular imaging. *Br J Radiol*. 2015;88(1055). doi:10.1259/bjr.20140308

[52] Manohar N, Reynoso FJ, Cho SH. Experimental demonstration of direct L-shell x-ray fluorescence imaging of gold nanoparticles using a benchtop x-ray source. Med Phys 2013; 40: 080702. doi: 10.1118/1.4816297

[53] Vernekohl D, Ahmad M, Dai X, Zhao W, Cheng K, Xing L (2019) Reduced acquisition time for L-shell x-ray fluorescence computed tomography using polycapillary x-ray optics. Med Phys

[54] Vernekohl D. X-Ray Excited Fluorescent Materials for Medical Application. In: *Top Med Chem*. Vol 9; 2014:1-68. doi:10.1007/7355

[55] Naczynski DJ, Sun C, Turkcan S, Jenkins C, Koh AL, Ikeda D, Pratx G, Xing L (2015) X-ray induced shortwave infrared biomedical imaging using rare-earth nanoprobes. Nano Lett 15:96–102

[56] Xing MM, Cao WH, Pang T, Ling XQ, Chen N. Preparation and characterization of monodisperse spherical particles of X-ray nano-phosphors based on Gd2O2S:Tb. Chinese Sci Bull. 2009;54(17):2982-6

[57] Thirumalai J, Chandramohan R, Valanarasu S, Vijayan TA, Somasundaram RM, Mahalingam T, Srikumar SR. Shape-selective synthesis and opto-electronic properties of Eu3+-doped gadolinium oxysulfide nanostructures. J Mater Sci. 2009;44(14):3889-99.

[58] Tian Y, Cao WH, Luo XX, Fu Y. Preparation and luminescence property of Gd2O2S : Tb X-ray nano- phosphors using the complex precipitation method. J Alloy Compd. 2007;433(1-2):313-7.

[59] Wang HY, Wang RJ, Sun XM, Yan RX, Li YD. Synthesis of red-luminescent Eu3+-doped lanthanides compounds hollow spheres. Mater Res Bull. 2005;40(6):911-9.

[60] Pires AM, Davolos MR, Stucchi EB. Eu3+ as a spectroscopic probe in phosphors based on spherical fine particle gadolinium compounds. Int J Inorg Mater. 2001;3(7):785-90.

[61] Sudheendra L, Das GK, Li CQ, Stark D, Cena J, Cherry S, Kennedy IM. NaGdF4:Eu3+ Nanoparticles for Enhanced X-ray Excited Optical Imaging. Chem Mater. 2014;26(5):1881-8. PMCID: PMC3985768

[62] Hainfeld JF, Powell RD. New frontiers in gold labeling. J Histochem Cytochem. 2000;48(4):471-80

[63] Sun C, Pratx G, Carpenter CM, Liu HG, Cheng Z, Gambhir SS, Xing L. Synthesis and Radioluminescence of PEGylated Eu3+-doped Nanophosphors as Bioimaging Probes. Adv Mater. 2011;23(24):H195-H9. PMCID: PMC4145869

[64] Karathanasis E, Chan L, Karumbaiah L, McNeeley K, D'Orsi CJ, Annapragada AV, Sechopoulos I, Bellamkonda RV. Tumor Vascular Permeability to a Nanoprobe Correlates to Tumor-Specific Expression Levels of Angiogenic Markers. Plos One. 2009;4(6). PMCID: PMC2688084.

[65] Kuang Y, Pratx G, Bazalova M, Qian J, Meng B, Xing L (2013) Development of XFCT imaging strategy for monitoring the spatial distribution of platinum-based chemodrugs: instru- mentation and phantom validation. Med Phys 40:030701

[66] Bazalova M, Ahmad M, Pratx G, Xing L. L-shell x-ray fluorescence computed tomography (XFCT) imaging of Cisplatin. *Phys Med Biol*. 2014;59(1):219-232. doi:10.1088/0031-9155/59/1/219

[67] Geraki K, Farquharson MJ, Bradley DA (2002) Concentrations of Fe, Cu and Zn in breast tissue: a synchrotron XRF study. Phys Med Biol 47:2327

[68] Costello LC, Franklin RB (1998) Novel role of zinc in the regulation of prostate citrate metabolism and its implications in prostate cancer. Prostate 35:285–296

[69] Larsson, J.C.; Vogt, C.; Vågberg, W.; Toprak, M.S.; Dzieran, J.; Arsenian-Henriksson, M.; Hertz, H.M. High-spatial-resolution X-ray fluorescence tomography with spectrally matched nanoparticles. Phys. Med. Biol. 2018, 63

[70] Shilo, M.; Reuveni, T.; Motiei, M.; Popovtzer, R. Nanoparticles as computed tomography contrast agents: Current status and future perspectives. Nanomedicine 2012, 7

[71] Hainfeld, J.F.; Slatkin, D.N.; Smilowitz, H.M. The use of gold nanoparticles to enhance radiotherapy in mice. Phys. Med. Biol. 2004, 49

[72] Jiang, S.; He, P.; Deng, L.; Chen, M.; Wei, B. Monte Carlo Simulation for Polychromatic X-ray Fluorescence Computed Tomography with Sheet-Beam Geometry. Int. J. Biomed. Imaging 2017

[73] B. L. Jones and S. H. Cho, "The feasibility of polychromatic cone-beam X-ray fluorescence computed tomography (XFCT) imaging of gold nanoparticle-loaded objects: a Monte Carlo Study," *Physics in Medicine and Biology*, vol. 56, no. 12, pp. 3719–3730, 2011.

[74] Quigley BP. X-ray induced luminescence imaging: Sensitivity measurements, selective plane geometry, and dual-modality X-ray fluorescence imaging. [Order No. 10808401]. The University of Chicago; 2018

[75] Romero, I. O., Fang, Y., Lun, M. & Li, C. X-ray fluorescence computed tomography (Xfct) imaging with a superfine pencil beam x-ray source. *Photonics* **8,** (2021)

[76] Zhang, W., Romero, I. O. & Li, C. Time domain X-ray luminescence computed tomography: numerical simulations. *Biomedical Optics Express* **10,** 372 (2019)

[77] Romero, I. O. & Li, C. Radiation dose estimation for pencil beam X-ray luminescence computed tomography imaging. *Journal of X-Ray Science and Technology* **29,** 773–784 (2021).

[78] Romero, I.O & Li, C. Correlation between X-ray tube current exposure time and X-ray photon number in GATE. *Journal of X-Ray Science and Technology*

[79] M. Lun, W. Zhang, and C. Li, "Sensitivity study of x-ray luminescence computed tomography," Appl. Opt. 56(11), 3010–3019 (2017).

[80] W. Zhang, D. Zhu, M. Lun, and C. Li, "Collimated superfine x-ray beam-based x-ray luminescence computed tomography," J. X-ray Sci. and Tech. 25(6), 945–957 (2017).

[81] W. Zhang, D. Zhu, M. Lun, and C. Li, "Multiple pinhole collimator-based X-ray luminescence computed tomography," Biomed. Opt. Express 7(7), 2506–2523 (2016).

[82] W. Zhang, L. Wu, J. Li, X. Yi, X. Wang, Y. Lu, W. Chen, Z. Zhou, L. Zhang, H. Zhao, and F. Gao, "Combined hemoglobin and fluorescence diffuse optical tomography for breast

tumor diagnosis: a pilot study on time- domain methodology," Biomed. Opt. Express 4(2), 331–348 (2013).

[83] Y. Zhang, A. A. Khan, G. D. Vigil, and S. S. Howard, "Super-sensitivity multiphoton frequency-domain fluorescence lifetime imaging microscopy," Opt. Express 24(18), 20862–20867 (2016).

[84] L. M. Hirvonen, F. Festy, and K. Suhling, "Wide-field time-correlated single-photon counting (TCSPC) lifetime microscopy with microsecond time resolution," Opt. Lett. 39(19), 5602–5605 (2014).

[85] A. Gibson, J. Hebden, and S. R. Arridge, "Recent advances in diffuse optical tomography," Phys. Med. Biol. 50(4), R1–R43 (2005).

[86] E. Gratton, S. Breusegem, J. D. B. Sutin, Q. Ruan, and N. P. Barry, "Fluorescence lifetime imaging for the two- photon microscope: time-domain and frequency-domain methods," J. Biomed. Opt. 8(3), 381–390 (2003).

[87] S. Liu, Y. Zhang, H. Liang, Z. Chen, Z. Liu, and Q. Zhao, "Time-resolved luminescence imaging of intracellular oxygen levels based on long-lived phosphorescent iridium(III) complex," Opt. Express 24(14), 15757–15764 (2016).

[88] W. Zheng, D. Tu, P. Huang, S. Zhou, Z. Chen, and X. Chen, "Time-resolved luminescent biosensing based on inorganic lanthanide-doped nanoprobes," Chem. Commun. (Camb.) 51(20), 4129–4143 (2015).

[89] K. Hanaoka, K. Kikuchi, S. Kobayashi, and T. Nagano, "Time-resolved long-lived luminescence imaging method employing luminescent lanthanide probes with a new microscopy system," J. Am. Chem. Soc. 129(44), 13502–13509 (2007).

[90] K. Suhling, P. French, and D. Phillips, "Time-resolved fluorescence microscopy," Photochem. Photobiol. Sci. 4(1), 13–22 (2005).

[91] M. Lazarczyk and M. Favre, "Role of Zn2+ Ions in Host-Virus Interactions," J. Virol. 82(23), 11486–11494 (2008).

[92] C.Supnet and I.Bezprozvanny,"The dysregulation of intracellular calcium in Alzheimer disease," Cell Calcium 47(2), 183–189 (2010).

[93] H. Lin, P. Herman, and J. Lakowicz, "Fluorescence lifetime-resolved pH imaging of living cells," Cytometry 52A(2), 77–89 (2003)

[94] F. Gao, H. Zhao, Y. Tanikawa, and Y. Yamada, "A linear, featured-data scheme for image reconstruction in time-domain fluorescence molecular tomography," Opt. Express 14(16), 7109–7124 (2006).

[95] C. Li, A. Martinez-Davalos, and S. R. Cherry, "Numerical simulation of X-ray luminescence optical tomography for small-animal imaging," J. Biomed. Opt. 19(4), 046002 (2014).

[96] C. Li, G. Wang, J. Qi, and S. R. Cherry, "Three-dimensional fluorescence optical tomography in small-animal imaging using simultaneous positron-emission-tomography priors," Opt. Lett. 34(19), 2933–2935 (2009).

[97] D. Zhu and C. Li, "Nonuniform update for sparse target recovery in fluorescence molecular tomography accelerated by ordered subsets," Biomed. Opt. Express 5(12), 4249–4259 (2014).

[98] D. Zhu and C. Li, "Nonconvex regularizations in fluorescence molecular tomography for sparsity enhancement," Phys. Med. Biol. 59(12), 2901–2912 (2014).

[99] W. Zhang, M. Lun, A. Nguyen, and C. Li, "X-ray luminescence computed tomography using a focused x-ray beam," J. Biomed. Opt. 22(11), 116004 (2017).

[100] P. Favier, L. Amoudry, K. Cassou, K. Dupraz, A. Martens, H. Monard, and F. Zomer, "The compact x-ray source ThomX," Proc. SPIE 10387, 1038708 (2017).

[101] Deng, L.; Ahmed, M.F.; Jayarathna, S.; Feng, P.; Wei, B.; Cho, S.H. A detector's eye view (DEV)-based OSEM algorithm for benchtop X-ray fluorescence computed tomography (XFCT) image reconstruction. *Phys. Med. Biol.* **2019**, *64*.

[102] Zhang, S.; Li, L.; Chen, J.; Chen, Z.; Zhang, W.; Lu, H. Quantitative imaging of gd nanoparticles in mice using benchtop cone-beam X-ray fluorescence computed tomography system. *Int. J. Mol. Sci.* **2019**, *20*, 2315.

[103] Dunning, C.A.S.; Bazalova-Carter, M. Optimization of a table-top X-ray fluorescence computed tomography (XFCT) system. Phys. Med. Biol. 2018, 63, 235013s

[104] Dunning, C.A.S.; Bazalova, M. Design of a combined X-ray fluorescence Computed Tomography (CT) and photon-counting CT table-top imaging system. *J. Instrum.* **2020**, *15*, P06031

[105] Defrise, M.; Kinahan, P.E.; Michel, C.J. Image Reconstruction Algorithms in PET. In *Positron Emission Tomography*; Bailey, D.L., Townsend, D.W., Valk, P.E., Maisey, M.N., Eds.; Springer: London, UK, 2005

[106] Zhu, D.; Li, C. Accelerated image reconstruction in fluorescence molecular tomography using a nonuniform updating scheme with momentum and ordered subsets methods. *J. Biomed. Opt.* **2016**, *21*, 016004

[107] Sarrut, D. *et al.* Advanced Monte Carlo simulations of emission tomography imaging systems with GATE. *Physics in Medicine and Biology* 66, (2021)
[108] S. Jan, G. Santin, D. Strul, et al., GATE: a simulation toolkit for PET and SPECT, *Phys Med Biol* 49(19) (2004), 4543–4561.

[109] D. Sarrut, M. Bardie`s, N. Boussion, et al., A review of the use and potential of the GATE Monte Carlo simulation code for radiation therapy and dosimetry applications: GATE for dosimetry, *Med Phys* 41(6) (2014), 064301.

[110] Achterhold, K.; Bech, M.; Schleede, S.; Potdevin, G.; Ruth, R.; Loewen, R.; Pfeiffer, F. Monochromatic computed tomography with a compact laser-driven X-ray source. *Sci. Rep.* **2013**, *3*, 3–6.

[111] Brun, R.; Rademakers, F. ROOT-An Object Oriented Data Analysis Framework, Proceedings AIHENP'96 Workshop, Lausanne, September 1996. *Nucl. Inst. Methods Phys. Res. A* **1997**, *389*, 81–86. Available online: http://root.cern.ch/ (accessed on 18 June 2021)

[112] Fessler, J.A. Michigan Image Reconstruction Toolbox. Available online: https://web.eecs.umich.edu/~fessler/code/index.html (accessed on 18 June 2021)

[113] M. Ahmad, G. Pratx, M. Bazalova and L. Xing, X-ray luminescence and X-ray fluorescence computed tomography: New molecular imaging modalities, *IEEE Access* **2** (2014), 1051–1061

[114] D. Chen, S. Zhu, X. Chen, et al., Quantitative cone beam X-ray luminescence tomography/X-ray computed tomography imaging, *Appl Phys Lett* **105** (2014), 191104.

[115] T. Liu, J. Rong, P. Gao, W. Zhang and W. Liu, Cone-beam X-ray luminescence computed tomography based on X-ray absorption dosage, *J Biomed Opt* **23**(2) (2018), 1–11

[116] A.M. Castellaro, A. Tonda, H.H. Cejas, et al., Oxalate induces breast cancer, *BMC Cancer* **15** (2015), 761

[117] L.M. Warren, A. Mackenzie, D.R. Dance and K.C. Young, Comparison of the X-ray attenuation properties of breast calcifications, aluminium, hydroxyapatite and calcium oxalate, *Phys Med Biol* **58**(7) (2013), N103–113

[118] K. Sakamoto, J.W. Schmidt and K.U. Wagner, Mouse models of breast cancer, *Methods Mol Biol* **1267** (2015), 47–71.

[119] M.K. Park, C.H. Lee and H. Lee, Mouse models of breast cancer in preclinical research, *Lab Anim Res* **34**(4) (2018), 160–165.

[120] Y.M. Zhang, M. Lun, C.Q. Li and Z.X. Zhou, Method for improving the spatial resolution of narrow X-ray beam-based X-ray luminescence computed tomography imaging, *Journal of Biomedical Optics* **24**(8) (2019), 1–11.

[121] J.M. Boone, O. Velazquez and S.R. Cherry, Small-Animal X-ray Dose from Micro-CT, *Molecular Imaging* **3**(3) (2004), 149–158.

[122] Huda, W. & Brad Abrahams, R. X-ray-based medical imaging and resolution. *American Journal of Roentgenology* 204, W393–W397 (2015)

[123] Lun, M. C. *et al.* Focused X-ray luminescence imaging system for small animals based on a rotary gantry. *Journal of Biomedical Optics* 26,(2021)

[124] Lun, M. C. *et al.* Contrast agents for X-ray luminescence computed tomography. *Applied Optics* 60, 6769 (2021)

[125] Bushberg, J. T. *The Essential physics of medical imaging*. Wolters Kluwer Health/Lippincott Williams & Wilkins, 2012; 3:229-230, 344

[126] McCollough, C. H. *et al.* CT dose index and patient dose: They are not the same thing. *Radiology* 259, 311–316 (2011)

[127] McNitt-Gray, M. F. AAPM/RSNA Physics Tutorial for Residents: Topics in CT. *RadioGraphics* 22, 1541–1553 (2002)

[128] Bazalova, M. & Verhaegen, F. Monte Carlo simulation of a computed tomography x-ray tube. *Physics in Medicine and Biology* 52, 5945–5955 (2007)

[129] Usman, S. & Patil, A. Radiation detector deadtime and pile up: A review of the status of science. *Nuclear Engineering and Technology* 50,1006–1016 (2018).

[130] Seco, J., Clasie, B. & Partridge, M. Review on the characteristics of radiation detectors for dosimetry and imaging. *Physics in Medicine and Biology* 59, R303–R347 (2014).

[131] Attix, F. H. Introduction to Radiological Physics and Radiation Dosimetry. Introduction to Radiological Physics and Radiation Dosimetry (Wiley, 1986). doi:10.1002/9783527617135

[132] Kawrakow, I. & Rogers, D. W. O. The EGSnrc Code System : Monte Carlo Simulation of Electron and Photon Transport. *System* 2001–2003 (2003)

[133] Briesmeister, J. F. *et al. MCNP-A General Monte Carlo Code for Neutron and Photon Transport, Version 3A. Los Alamos National Lab., NM (USA)* (1986)

[134] Agostinelli, S. *et al.* GEANT4 - A simulation toolkit. *Nuclear Instruments and Methods in Physics Research, Section A: Accelerators, Spectrometers, Detectors and Associated Equipment* 506, 250–303 (2003)

[135] M.C. Lun, W. Cong, M. Arifuzzaman, M. Ranasinghe, S. Bhattacharya, J. Anker, G. Wang, and C. Li, *"X-ray luminescence imaging for small-animals",* Proc. of SPIE 11224, Optics and Ionizing Radiation; 112240F (2020)

[136] Kim, K. *et al.* Penalized PET Reconstruction Using Deep Learning Prior and Local Linear Fitting. *IEEE Transactions on Medical Imaging,* **37,** 1478–1487 (2018)

[137] Jung, S., Lee, J., Cho, H., Kim, T. & Ye, S. J. Compton Background Elimination for in Vivo X-Ray Fluorescence Imaging of Gold Nanoparticles Using Convolutional Neural Network. *IEEE Transactions on Nuclear Science* **67,** 2311–2320 (2020)

[138] Feng, P. Luo Y, Zhao R, Huang P, Li Y, He P, Tang B, Zhao X. Reduction of Compton Background Noise for X-ray Fluorescence Computed Tomography with Deep Learning. *Photonics* **9**, 108 (2022)

[139] Romero, I. O. & Li, C. A feasibility study of time of flight cone beam computed tomography imaging. *Journal of X-Ray Science and Technology* **29,** 867–880 (2021)

[140] Rossignol, J. *et al.* Time-of-flight computed tomography - proof of principle. *Physics in Medicine and Biology* **65,** (2020)

[141] Quénot, L., Brun, E., Létang, J. M. & Langer, M. Evaluation of simulators for x-ray speckle-based phase contrast imaging. *Physics in Medicine and Biology* **66,** (2021)

[142] Zhou, T. *et al.* Speckle-based x-ray phase-contrast imaging with a laboratory source and the scanning technique. *Optics Letters* **40,** 2822 (2015)

[143] Wang, H. *et al.* X-ray phase contrast tomography by tracking near field speckle. *Scientific Reports* **5,** (2015)

[144] Zdora, M. C. State of the Art of X-ray Speckle-Based Phase-Contrast and Dark-Field Imaging. *Journal of Imaging* **4,** (2018)

[145] Paganin, D. M., Labriet, H., Brun, E. & Berujon, S. Single-image geometric-flow x-ray speckle tracking. *Physical Review A* **98,** (2018)

[146] Rouge-Labriet, H. *et al.* Comparison of X-ray speckle-based imaging deflection retrieval algorithms for the optimization of radiation dose. *Physics in Medicine and Biology* **66,** (2021)